Nonlinear Modeling Parameters for Reinforced Concrete Coupling Beams

Christopher Motter

Baha'a Al-Khateeb

Dakota Saathoff

May 2022

Washington State University

Department of Civil and Environmental Engineering

ABSTRACT

A database of diagonally reinforced concrete coupling beam tests was formulated and used to assess strength, stiffness, and deformation capacity. The shear strength equation provided in ACI 318-19 considers only the transverse strength of the diagonal bars and was found to be overly conservative. A new equation that includes shear strength of concrete and transverse reinforcement was found to provide a better fit to test data. Existing recommendations were found to underestimate deformation capacity. A plastic hinge model that includes bond slip was formulated to estimate deformation capacity based on strain at crushing of confined concrete and strain at onset of diagonal reinforcement buckling. Favorable agreement was found between the model and test data. An empirical equation based on ratio of diagonal bar diameter to section depth and ratio of spacing of transverse reinforcement to diagonal bar diameter was fit to data. The empirical equation led to reduced scatter relative to the plastic hinge model. A parametric study was conducted using the plastic hinge model and the empirical equation, and reasonable agreement was found between the two models over this practical range of parameters. New recommendations for determining the deformation capacity of diagonally reinforced concrete coupling beams are provided.

Damage patterns observed after the 2010-2011 Canterbury earthquake sequence in New Zealand showed instances in which coupled walls did not behave as intended in design, as plastic hinges formed at the base of the wall piers but not at the beam ends. A potential cause was coupling beam axial restraint from walls and floors increasing the strength of the coupling beams. The deformation capacity model was not intended to predict axial elongation and capture the resulting

influence of axial restraint on coupling beam deformation capacity. To better understand the effect of axial restraint on coupling beam strength and deformation capacity, seven one-half-scale reinforced concrete coupling beams, designed using ACI 318-19, were constructed and tested under constant axial compressive stiffness. Test variables were reinforcement configuration (conventional or diagonal), span-to-depth ratio, primary reinforcement ratio and bar diameter, and level of axial restraint. Six beams consisted of three identical pairs, with the two beams in each pair tested at a different level of constant stiffness axial restraint. The conventionally reinforced beams were observed to yield in shear. The onset of significant strength degradation in the diagonally reinforced beams was associated with buckling of diagonal reinforcement rather than crushing of confined concrete. As a result, deformation capacity was more sensitive to variation in the ratio of transverse reinforcement spacing to diagonal bar diameter, s/d_b , than variation in axial compression. The diagonally reinforced beams with #4 and #6 reinforcement had deformation capacity of at least 6% and 10%, respectively. The deformation capacity was at least 15% larger than that predicted using the empirical model, suggesting that axial restraint did not result in a reduction of deformation capacity.

It is recommended to design coupled walls for expected coupling beam demands. Results from this study provide experimentally derived values for the level of overstrength in diagonally reinforced coupling beams with axial restraint. Values of constant axial compressive stiffness used in the tests ranged from $0.69A_gf'c$ to $1.38A_gf'c$ per inch and led to development of peak compressive stresses of $0.27-0.51A_gf'c$. This resulted in an increase in beam strength as high as 120% above nominal moment strength when computed without consideration of axial restraint and as high as 53% when computed at peak measured axial force. The difference between M_n computed at peak

measured axial force and computed without axial force suggested an increase in beam shear strength due to axial restraint as high as 64%, with larger values associated with lower longitudinal reinforcement ratio.

This research was sponsored by the American Concrete Institute (ACI) Foundation.

ACKNOWLEDGEMENTS

This report is based on a thesis by Dakota Saathoff and a thesis by Baha'a Al-Khateeb, both completed in partial fulfillment of the requirements for a M.S. degree from Washington State University. Thanks are extended to S. Lewis, J. Jennings, D. Dolan, K. Maloney, S. McGuiness, A. Hill, J. Forbes, J. Hatt, M. Jarrah, A. Islam, M. Wagemann Herrera, C. Moen, J. Divelbiss, R. Dombrowski, T. Walters, and Z. Kylany for assistance with laboratory testing.

This research was sponsored by the American Concrete Institute (ACI) Foundation. The authors express their gratitude to the ACI Foundation and Executive Director Ann Masek. Any opinions, findings, and conclusions expressed in this report are those of the authors and do not necessarily reflect those of the ACI Foundation.

TABLE OF CONTENTS

ABSTRACT	ii
ACKNOWLEDGEMENTS	v
TABLE OF CONTENTS	vi
LIST OF FIGURES	viii
LIST OF TABLES	xii
1. INTRODUCTION	1
2. BACKGROUND	4
2.1 Reinforced Concrete Coupling Beams	4
2.2 Modeling Parameters	5
3. DEVELOPMENT OF MODELING PARAMETERS	9
3.1 Experimental Database	9
3.2 Deformation Capacity	14
3.2.1 Beam Model	14
3.2.1.1 Model Development	14
3.2.1.2 Model Validation	23
3.2.3 Empirical Model	31
3.2.4 Parametric Study	36
3.3 Effective Stiffness	41

	3.4 Strength	43
4.	EXPERIMENTAL PROGRAM	48
	4.1 Beam Details	48
	4.2 Construction	55
	4.3 Material Properties	59
	4.4 Test Set-Up	61
	4.5 Instrumentation	65
	4.6 Loading Protocol	70
5.	EXPERIMENTAL RESULTS AND DISCUSSION	73
	5.1 Observed Damage	73
	5.2 Axial Elongation and Axial Restraint	83
	5.3 Force-Deformation	86
	5.4 Components of Deformation	94
	5.5 Effective Stiffness	96
	5.6 Backbone Models	97
	5.7 Reinforcement Strain	. 101
	5.8 Curvature Profiles	. 101
6	SUMMARY AND CONCLUSIONS	. 104
D	EEEDENCES	110

LIST OF FIGURES

Figure 2.1. Nonlinear Modeling Parameters
Figure 3.1. Ghannoum and Matamoros (2014) Backbone Model Fit to CB33F11
Figure 3.2. Coupling Beam Deformation Capacity Relative to: a) ρ , b) s/d_b c) ρ_t , and d) L/h 13
Figure 3.3. Diagonally Reinforced Coupling Beam Deformation Model
Figure 3.4. Compression Reloading Strain
Figure 3.5. Comparison of Model Results with L_p as a Multiple of a) h , b) $h*\cos(\alpha)$ c) L , and d)
$L^*\cos(\alpha)$
Figure 3.6. Comparison of Model Results, Excluding Specimens C6 and C8, with L_p as a Multiple
of a) h , b) $h^*\cos(\alpha)$ c) L , and d) $L^*\cos(\alpha)$
Figure 3.7. Select Model Results with L_p as a Multiple of h , $h*\cos(\alpha)$, L , and $L*\cos(\alpha)$, a) Including
Specimens C6 and C8, and b) Excluding Specimens C6 and C8
Figure 3.8. Predicted Coupling Beam Deformation Capacity Relative to: a) ρ , b) s/d_b , c) ρt , and d)
<i>L/h</i>
Figure 3.9. a) Comparison of Predicted d using Empirical Model to Measured d, b) Comparison
of Ratio of Predicted to Measured d to s/db
Figure 3.10. Measured and Predicted d with Variation in: a) ρ , b) s/d_b , c) d_b/h , and d) L/h 35
Figure 3.11. Cross-Sectional Drawings for Beams in Parametric Study
Figure 3.12. Parametric Study Results for: a) d_b/h , b) s/d_b , and c) L/h
Figure 3.13. Comparison of Predicted to Measured Stiffness

Figure 3.14. Ratio of Measured Maximum Shear Force to Nominal Strength for a) V_n from ACl
318-19, b) Proposed V_n from Eq. (3.22) c) V_n from ACI 318-19 Without $10f'cbwd$ Limit, and d
Proposed V_n from Eq. (3.22) Without $10f'cbwd$ Limit
Figure 3.15. Comparison of Peak Measured Shear Demand to $10f'cbwd$ Limit
Figure 4.1. C(#5)-3.0-0.69 and C(#5)-3.0-1.38: a) Elevation View and b) Beam Cross Section. 49
Figure 4.2. D(#4)-3.0-0.69 and D(#4)-3.0-0.69: a) Elevation View and b) Beam Cross Section 50
Figure 4.3. D(#6)-3.0-0.69 and D(#6)-3.0-0.69: a) Elevation View and b) Beam Cross Section 50
Figure 4.4. D(#4)-1.5-0.69: a) Elevation View and b) Beam Cross Section
Figure 4.5. Strain Gauge Installation
Figure 4.6. Reinforcement Cages for Top and Bottom Blocks
Figure 4.7. Reinforcement Cages for C(#5)-3.0-0.69 and C(#5)-3.0-0.35
Figure 4.8. Reinforcement Cage for D(#4)-3.0-0.69 or D(#4)-3.0-1.38
Figure 4.9. Reinforcement Cage for D(#6)-3.0-0.69 or D(#6)-3.0-1.38
Figure 4.10. Reinforcement Cage for D(#6)-1.5-0.69
Figure 4.11. Reinforcement Cages in Formwork Prior to Pouring Concrete to Top of Beams 58
Figure 4.12. Stress-Strain for: a) #4 Reinforcement, b) #5 Reinforcement, c) #6 Reinforcement
and d) 5/16"-Diameter Reinforcement
Figure 4.13. 2D Drawing of Test Set Up
Figure 4.14. 3D Rendering of Test Set-Up
Figure 4.15. Photo of Test Set-Up
Figure 4.16. LVDT Layout for: a) Beams with Span-to-Depth Ratio of 3.0 and b) Beam with Span-
to-Depth Ratio of 1.567
Figure 4.17. Photo of LVDTs on Test Beam

Figure 4.18. Strain Gauge Layout for: a) C(#5)-3.0-0.69 and C(#5)-3.0-0.35, b) D(#6)-3.0-0.69
and D(#6)-3.0-1.38, c) D(#4)-3.0-0.69 and d) D(#4)-3.0-1.38, and d) D(#6)-1.5-0.69
Figure 4.19. Loading Protocol
Figure 4.20. LVDTs Use to Determine Measured Chord Rotation
Figure 5.1. Damage Photos for C(#5)-3.0-0.69 at First Cycle Displacement Peaks
Figure 5.2. Damage Photos for C(#5)-3.0-0.35 at First Cycle Displacement Peaks
Figure 5.3. Damage Photos for D(#4)-3.0-0.69 at First Cycle Displacement Peaks
Figure 5.4. Damage Photos for D(#4)-3.0-1.38 at First Cycle Displacement Peaks
Figure 5.5. Damage Photos for D(#6)-3.0-0.69 at First Cycle Displacement Peaks
Figure 5.6. Damage Photos for D(#6)-3.0-1.38 at First Cycle Displacement Peaks
Figure 5.7. Damage Photos for D(#6)-1.5-0.69 at First Cycle Displacement Peaks
Figure 5.8. Axial Elongation and Force for: a) C(#5)-3.0-0.69, b) C(#5)-3.0-0.35, c) D(#4)-3.0-
0.69, d) D(#4)-3.0-1.38, e) D(#6)-3.0-0.69, f) D(#6)-3.0-1.38, and g) D(#6)-1.5-0.69
Figure 5.9. Load-Displacement Responses of: a) C(#5)-3.0-0.69, b) C(#5)-3.0-0.35, c) D(#4)-3.0-0.40
0.69, d) D(#4)-3.0-1.38, e) D(#6)-3.0-0.69, f) D(#6)-3.0-1.38, and g) D(#6)-1.5-0.69
Figure 5.10. Load-Displacement Responses of: a) FB33 (Naish et al, 2011), b) HB3-6L-T100
(Xiao, 1999), and c) C(#5)-3.0-0.35
Figure 5.11. Observed Damage at 4.0% Chord Rotation for a) FB33 (Naish et al, 2011), b) HB3-
6L-T100 (Xiao, 1999), and c) C(#5)-3.0-0.35
Figure 5.12. Load-Displacement Responses of: a) CB33F (Naish et al, 2011) and b) D(#6)-3.0-
1.38
Figure 5.13. Components of Deformation for: a) C(#5)-3.0-0.69, b) C(#5)-3.0-0.35, c) D(#4)-3.0-0.40
0.69, d) D(#4)-3.0-1.38, e) D(#6)-3.0-0.69, f) D(#6)-3.0-1.38, and g) D(#6)-1.5-0.69

Figure 5.14. Effective Secant Stiffness	97
Figure 5.15. Backbone Models for: a) C(#5)-3.0-0.69, b) C(#5)-3.0-0.35, c) D(#4)-3.0-0.0	69, d)
D(#4)-3.0-1.38, e) D(#6)-3.0-0.69, f) D(#6)-3.0-1.38, and g) D(#6)-1.5-0.69	99
Figure 5.16. Reinforcement Strain Profiles for: a) C(#5)-3.0-0.69, b) C(#5)-3.0-0.69, c) D(#4)-3.0
0.69, d) D(#4)-3.0-1.38, e) D(#6)-3.0-0.69, f) D(#6)-3.0-1.38, and g) D(#6)-1.5-0.69	102
Figure 5.17. Curvature Profiles for: a) C(#5)-3.0-0.69, b) C(#5)-3.0-0.35, c) D(#4)-3.0-0.0	69, d)
D(#4)-3.0-1.38, e) D(#6)-3.0-0.69, f) D(#6)-3.0-1.38, and g) D(#6)-1.5-0.69	103

LIST OF TABLES

Table 2.1. FEMA 273, ASCE/SEI 41-17, and ACI 374 Recommended Values for d and e for
Coupling Beams Controlled by Flexure
Table 2.2. FEMA 273, ASCE/SEI 41-17, and ACI 374 Recommended Values for d and e for
Coupling Beams Controlled by Shear
Table 3.1. Sample Parameters from Diagonally Reinforced Concrete Coupling Beam Tests 10
Table 3.2. Deformation Capacity and Failure Mechanism Predicted by Model
Table 3.3. Variation in Parameters for Beams in Parametric Study
Table 3.4. Sources of Deformation at Deformation Capacity for Beams in Parametric Study 41
Table 4.1. Test Matrix
Table 4.2. Measured Concrete Compressive Strength from 6"x12" Cylinder Tests
Table 4.3. Measured Yield and Ultimate Tensile Strength of Reinforcement
Table 5.1. Chord Rotation at Onset of Major Damage Events
Table 5.2. Maximum Measured Crack Widths
Table 5.3. Number of Bar Fractures at Each Cycle
Table 5.4. Measured Peak Axial Load and Corresponding Deformation
Table 5.5. Measured Strength
Table 5.6. Effective Stiffness and Yield Rotation from Backbone Model Fit to Test Data 100

1. INTRODUCTION

Reinforced concrete walls are often used in buildings to provide lateral resistance to wind and seismic demands. Adjacent coplanar walls may include coupling beams, which are often located above door openings. Coupling beams are often used by designers to enhance strength and stiffness and to provide energy dissipation. Coupling beams transfer shear and moment into the wall. The shear demands from the beams create axial loads in the walls. Coupled walls are stiffer and stronger than uncoupled walls due to the moment resistance provided by the axial tension-compression force couple. During large earthquakes, plasticity is expected to concentrate at the base of the walls and at the ends of the coupling beams. Coupling beams are typically designed to yield prior to walls and are designed for ductile response to provide energy dissipation. The rotational demands on coupling beams are typically higher than walls, columns, and moment frame beams, due to the shorter length of the coupling beams. The use of diagonal reinforcement in reinforced concrete coupling beams is commonplace due to improved resistance to shear sliding at advanced deformation demands relative to conventional reinforcement.

Reinforced concrete plastic hinges have a tendency to elongate during cyclic loading caused by earthquakes. Despite the tendency of reinforced concrete coupling beams to elongate once plastic hinges have formed, the design of coupling beams in accordance with building codes typically does not include consideration of the influence of axial restraint on coupling beam behavior. Observed damage patterns in coupled walls in New Zealand following the 2010-2011 Canterbury earthquake sequence did not match the expected damage patterns for coupled walls. Instead, plasticity was observed to have concentrated at the base of the walls, without evidence of coupling

beam yielding. It was speculated by the Canterbury Earthquakes Royal Commission (CERC, 2012) that axial restraint of coupling beams may have generated axial compression that caused an increase in coupling beam strength. An increase in coupling beam strength may have prevented the coupling beams from yielding while also creating larger axial demands on the walls than were considered in design, leading to yielding of the wall piers without yielding of the coupling beams. The resulting lack of energy dissipation in the coupling beams in combination with the increased axial loading demands on the walls would be expected to result in more demand on the walls than was considered in design, thereby increasing the potential for failure of the walls.

Limited experimental studies have been conducted on individual reinforced concrete coupling beams subjected to axial restraint. In this study, seven reinforced concrete coupling beams were tested in a fixed-fixed condition with constant axial compressive stiffness within each test. Test variables included span-to-depth ratio, reinforcement configuration (longitudinal or diagonal), longitudinal and transverse reinforcement ratio, and transverse reinforcement spacing. The results were used to assess the impact of axial restraint on coupling beam behavior. The data generated from the study may be used for calibration of nonlinear numerical coupling beam models that could be used for future modeling efforts of coupled wall behavior.

Nonlinear dynamic analyses are often used to analyze the response of structures subjected to earthquake demands. Modeling parameters for strength, stiffness, and ductility of individual components that comprise a lateral force resisting system are required for nonlinear dynamic analyses. Recommended values for modeling parameters of reinforced concrete beams, columns, walls, and coupling beams are provided in Seismic Evaluation and Retrofit of Existing Buildings

(ASCE/SEI 41-17), Guide to Nonlinear Modeling Parameters for Earthquake-Resistant Structures (ACI 374.3R-16), and Guidelines for Performance-Based Seismic Design of Tall Buildings (PEER TBI, 2017). There is discrepancy in the recommended values between the documents. Additionally, the recommendations in ASCE/SEI 41-17 were initially published in FEMA 273 (1997) and have not been updated for diagonally reinforced coupling beams, despite an abundance of new test data. In this report, updated nonlinear modeling parameters for diagonally reinforced concrete coupling beams are provided. The new recommendations were formulated based on a database of past tests and simplified models to estimate deformation capacity.

2. BACKGROUND

2.1 Reinforced Concrete Coupling Beams

ACI 318-19 Section 18.10.7 specifies the use of either conventionally reinforced or diagonally reinforced concrete coupling beams. For coupling beams with span-to-depth ratio greater than or equal to 4.0, coupling beams are prescribed to be designed as Special Moment Frame beams using ACI 318-19 Section 18.6. For coupling beams with span-to-depth ratio less than 2.0, diagonal reinforcement is prescribed. For coupling beams with span-to-depth ratio between 2.0 and 4.0, either option is permitted. For diagonally reinforced concrete coupling beams, transverse reinforcement is prescribed in ACI 318-19 Section 18.10.7.4 to confine each group of diagonal bars or the entire cross-section. The transverse reinforcement detailing requirements are prescribed to meet those for columns of special moment frames in ACI 318-19 Section 18.7.5.2 (a) through (e). The option to provide transverse reinforcement around the entire cross-section was introduced in ACI 318-08, with ACI 318-05 and earlier editions of the ACI building code prescribing transverse reinforcement around the diagonal bar groups.

The mechanism of shear load resistance differs for diagonally and conventionally reinforced concrete coupling beams. For an imposed chord rotation on a diagonally reinforced concrete coupling beam, one group of diagonal bars is in tension and the other is in compression, such that both sets of bars provide shear resistance due to the vertical (transverse) components of axial bar force. Diagonally reinforced concrete coupling beams have improved resistance to sliding shear failure over that of conventionally reinforced concrete coupling beams (Paulay and Binney, 1974).

Due to the enhanced shear strength of a diagonally reinforced coupling beam, a shallower beam may be used to achieve the desired shear strength, while meeting potential depth limitations imposed by architectural constraints on story and doorway heights.

2.2 Modeling Parameters

Recommended nonlinear modeling parameters for structural components are provided in ASCE/SEI 41-17 and ACI 374.3R-16 and are based on statistical values from test data. As shown in Figure 2.1, these parameters are used to formulate the load-deformation backbone model for the structural component, which includes the deformation capacity before strength loss, d, the total deformation capacity, e, and the elastic stiffness, k, determined based on an effective flexural and shear rigidity. The recommended values for a given structural component typically differ based upon parameters that are expected to significantly influence the component behavior.

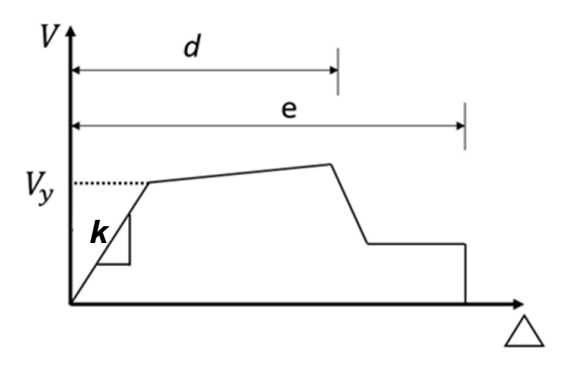


Figure 2.1. Nonlinear Modeling Parameters

The effective stiffness of coupling beams is specified in ASCE/SEI 41-17 Section 10.7.2.2 to be the same as non-prestressed beams, which is $0.3E_cI_g$ for flexural rigidity and $0.4E_cA_W$ for shear rigidity, where E_c is the modulus of elasticity of concrete, I_g is the gross moment of inertia of the

cross-section, and A_w is the cross-sectional area of the beam web. The recommended flexural rigidity of $0.3E_cI_g$ was reduced from the value of $0.5E_cI_g$ specified in FEMA 273 (1997). Recommended values for the effective stiffness of diagonally reinforced concrete coupling beams are also provided in PEER TBI (2017) Section 4.6.3 as $0.07 \left(\frac{L}{h}\right) E_cI_g$ for flexural rigidity and $0.4E_cA_g$ for shear rigidity, where $\frac{L}{h}$ is the ratio of length to height (i.e., aspect ratio) of the beam.

Modeling parameters for deformation capacity in ASCE/SEI 41-17 and ACI 374.3R-16 differ for conventionally and diagonally reinforced concrete coupling beams. Diagonally reinforced concrete coupling beams have larger values to reflect the mitigation of shear sliding at advanced deformation levels. As shown in Table 2.1 and Table 2.2, the modeling parameters provided by ASCE/SEI 41-17 and ACI 374.3R-16 for reinforced concrete coupling beams were adopted from FEMA 273 (1997) with some modifications for conventionally reinforced concrete coupling beams. Conventionally reinforced concrete coupling beams have multiple categories of parameters based on the level of conformance of the transverse reinforcement and the shear stress demand, $\frac{v}{t_w l_w \sqrt{f_c'}}$. ACI 374.3R-16 specifies parameters for beams that are ACI 318 compliant, without providing values for non-compliant beams. In ASCE/SEI 41-17, the criteria for conforming transverse reinforcement for conventionally reinforced concrete coupling beams are closed hoops placed over the entire length of the beam at a spacing less than or equal to $d_s/3$, where d_s is the distance from the extreme compression fiber to the centroid of tension reinforcement, and shear strength of closed stirrups, V_s , greater than or equal to 75% of the required shear strength of the coupling beam. ACI 374.3R-16 includes only the V_s requirement. For conforming coupling beams, identical modeling parameters are provided by ACI 374.3R-16 and ASCE/SEI 41-17 for d and e.

One category of modeling parameters is provided in ASCE/SEI 41-17 and ACI 374.3R-16 for diagonally reinforced concrete coupling beams, with the beams categorized as being controlled by flexure. The recommended values in ASCE 41-17 (2017) and ACI 374-16 (2016) are consistent with FEMA 273 (1997). At the time of publishing of FEMA 273 (1997), identified test data on diagonally reinforced concrete coupling beams included Binney (1972), Paulay and Binney (1974), Santhakumar (1974), Barney et al (1980), and Tassios et al (1996). An abundance of new test data (Galano and Vignoli, 2000; Weber-Kamin et al, 2019; Kwan et al, 2002; Fortney et al, 2008; Naish et al, 2013; Shin et al, 2014; Han et al, 2017; Lim et al, 2016; Poudel et al, 2018; and Jang et al, 2018) has become available since the publication of FEMA 273 (1997). In this study, the new data is included in the formulation of updated nonlinear modeling parameters.

Table 2.1. FEMA 273, ASCE/SEI 41-17, and ACI 374 Recommended Values for *d* and *e* for Coupling Beams Controlled by Flexure

Condition	Shear Ratio	Chord Rotati	on, (radians)	Chord Rotation	on, (radians)	Chord Rotation, (radians)			
	V	FEMA	A 273	ASCE/SI	El 41-17	ACI 374.3R-16			
	$\overline{t_w l_w \sqrt{f_c'}}$	d	е	d	e	d	е		
Conventional longitudinal reinforcement with conforming transverse	≤ 3	0.025	0.040	0.025	0.050	0.025	0.050		
reinforcement.	≥ 6	0.015	0.030	0.020	0.040	0.020	0.040		
Conventional longitudinal reinforcement	≤ 3	0.020	0.035	0.020	0.035	N/A	N/A		
with nonconforming transverse reinforcement.	≥ 6	0.010	0.025	0.010	0.025	N/A	N/A		
Diagonal reinforcement	N/A	0.030	0.050	0.030	0.050	0.030	0.050		

Table 2.2. FEMA 273, ASCE/SEI 41-17, and ACI 374 Recommended Values for d and e for Coupling Beams Controlled by Shear

Condition	Shear Ratio	Chord Rotati	on, (radians)	Chord Rotation	on, (radians)	Chord Rotation, (radians)			
	V	FEMA	A 273	ASCE/SI	El 41-17	ACI 374.3R-16			
	$\overline{t_w l_w \sqrt{f_c'}}$	d	е	d	e	d	e		
Conventional longitudinal reinforcement with conforming transverse	≤ 3	0.018	0.030	0.020	0.030	0.020	0.030		
reinforcement.	≥ 6	0.012	0.020	0.016	0.024	0.016	0.024		
Conventional longitudinal reinforcement with nonconforming transverse	≤ 3	0.012	0.025	0.012	0.025	N/A	N/A		
reinforcement.	≥ 6	0.008	0.014	0.008	0.014	N/A	N/A		

3. DEVELOPMENT OF MODELING PARAMETERS

3.1 Experimental Database

A database of diagonally reinforced concrete coupling beam tests was compiled and includes 42 tests, 34 of which were conducted after publication of FEMA 273 (1997). As shown in Table 2.1, the recommended values for d and e in ASCE 41-17 (2017) and ACI 374-16 (2016) are consistent with FEMA 273 (1997), reflecting the need for updated nonlinear modeling parameters. The database included parameters on beam geometry, reinforcement details, material properties, component strength, ACI 318 compliance, test results, and modeling parameters d, a, and k, where a is the plastic deformation capacity up to 20% strength loss. The lack of test data that extends significantly beyond 20% strength loss prevented gathering of accurate values for the modeling parameter e. Select parameters from the database are provided in Table 3.1, where d_b is the bar diameter of diagonal reinforcement, ρ is the longitudinal reinforcement ratio, ρ_{shx} and ρ_{shy} are the transverse reinforcement ratio in the x- and y-direction of the cross-section, respectively, s is the spacing of transverse reinforcement measured as the distance along the diagonal bar, f'_c is the tested compressive strength of concrete, and f_y is the tested yield strength of diagonal reinforcement. ρ was determined as the ratio of the area of longitudinal tension reinforcement to the product of the beam width and effective depth. The area of longitudinal tension reinforcement was taken as the product of the area of reinforcement in one diagonal bar bundle multiplied by the cosine of the angle of inclination of the diagonal reinforcement relative to the longitudinal orientation of the beam. For ρ_{shx} and ρ_{shy} , the x- and y-directions were oriented along the crosssection width and height, respectively. The modeling parameters were obtained from a piecewise

linear load-displacement backbone model fit to each test using the Ghannoum and Matamoros (2014) procedure, with an example shown in Figure 3.1 for specimen CB33F tested by Naish et al (2013).

Table 3.1. Sample Parameters from Diagonally Reinforced Concrete Coupling Beam Tests

Specimen Name	Author	Year of Publication	Depth	Width	Length	d_b	ρ	Confinement Type	ρ_{shx}	ρ_{shy}	S	f_c'	f_y	d	а	k	ACI 318-19 Compliance
			(in)	(in)	(in)	(in)		-77			(in)	(psi)	(psi)	(%)	(%)	$(\%E_cI_a)$	
C6	Barney et al	1980	6.67	4.00	16.67	0.38	0.007	F	0.0128	0.0073	1.33	3470	62800	6.0	5.0	8.7	N
C8	Barney et al	1980	6.67	4.00	33.33	0.38	0.008	F	0.0128	0.0073	1.33	3470	62800	6.8	5.7	19.2	N
DCB-1	Fortney et al	2008	14.00	10.00	36.00	1.00	0.031	D	0.0032	0.0037	14.00	5550	62600	4.6	3.2	10.6	N
DCB-2	Fortney et al	2008	12.00	10.00	36.00	0.88	0.031	D	0.0098	0.0146	2.00	8020	69200	10.0	8.9	12.5	Y*
P07	Galano et al	2000	15.75	5.90	23.62	0.39	0.006	F	0.0045	0.0015	4.00	7832	82215	4.6	3.8	3.4	N
P12	Galano et al	2000	15.75	5.90	23.62	0.39	0.006	D	0.0074	0.0068	4.00	6032	82215	3.5	2.6	3.3	N
SD-2.0	Han et al	2017	20.67	9.84	41.34	0.88	0.015	F	0.0140	0.0129	4.75	6380	63530	5.7	4.2	6.9	Y
BD-2.0	Han et al	2017	20.67	9.84	41.34	0.88	0.015	F	0.0140	0.0129	4.75	6380	63530	5.7	4.0	6.7	Υ
SD-3.5	Han et al	2017	11.81	9.84	41.34	1.00	0.036	F	0.0167	0.0286	4.00	6380	64100	10.0	8.3	15.0	Υ
BD-3.5	Han et al	2017	11.81	9.84	41.34	1.00	0.035	F	0.0167	0.0286	4.00	6380	64100	10.0	8.5	19.9	Υ
D80-1.5	Kamin et al	2019	18.00	12.00	27.00	0.75	0.015	F	0.0105	0.0089	3.00	7600	83000	6.9	6.0	5.6	Υ
D100-1.5	Kamin et al	2019	18.00	12.00	27.00	0.75	0.013	F	0.0105	0.0089	3.00	8200	108000	5.3	4.3	5.4	Υ
D120-1.5	Kamin et al	2019	18.00	12.00	27.00	0.75	0.010	F	0.0105	0.0089	3.00	7600	116000	5.1	3.8	4.2	Υ
D80-2.5	Kamin et al	2019	18.00	12.00	45.00	0.75	0.024	F	0.0105	0.0089	3.00	8400	83000	7.7	6.4	9.7	Υ
D100-2.5	Kamin et al	2019	18.00	12.00	45.00	0.75	0.019	F	0.0105	0.0089	3.00	8000	108000	6.0	4.7	9.6	Υ
D120-2.5	Kamin et al	2019	18.00	12.00	45.00	0.75	0.016	F	0.0105	0.0089	3.00	7800	116000	6.6	4.8	8.9	Υ
D80-3.5	Kamin et al	2019	18.00	12.00	63.00	0.88	0.033	F	0.0105	0.0089	3.00	7800	84000	8.6	7.2	17.2	Υ
D100-3.5	Kamin et al	2019	18.00	12.00	63.00	0.75	0.024	F	0.0105	0.0089	3.00	7900	108000	6.9	5.5	14.8	Υ
D120-3.5	Kamin et al	2019	18.00	12.00	63.00	0.75	0.021	F	0.0105	0.0089	3.00	8200	116000	6.7	4.8	12.7	Y
CCB11	Kwan et al	2002	23.62	4.72	27.56	0.32	0.004	D	0.0155	0.0089	2.36	5483	74986	5.5	4.2	1.6	Y*
CB10-1	Lim et al	2016	19.69	9.84	19.69	1.00	0.020	F	0.0177	0.0118	4.00	7557	63760	5.9	4.2	2.0	N
CB20-1	Lim et al	2016	19.69	11.81	39.37	1.13	0.022	F	0.0143	0.0118	4.00	7557	67632	7.8	6.8	8.5	Y
CB30-DA	Lim et al	2016	19.69	11.81	59.07	1.27	0.027	D	0.0072	0.0085	5.91	5758	67444	7.8	6.7	13.5	N
CB30-DB	Lim et al	2016	19.69	11.81	59.07	1.27	0.027	F	0.0082	0.0067	3.94	5570	67444	7.8	6.8	15.7	N
CB24F	Naish et al	2008	15.00	12.00	36.00	0.88	0.023	F	0.0116		3.00	6850	70133	9.7	8.6	9.9	N
CB24D	Naish et al	2008	15.00	12.00	36.00	0.88	0.023	D	0.0163	0.0214	2.50	6850	70133	8.7	7.7	10.3	Y*
CB24F-RC	Naish et al	2008	15.00	12.00	36.00	0.88	0.023	F	0.0116		3.00	7305	70133	10.5	9.3	10.6	N
CB24F-PT	Naish et al	2008	15.00	12.00	36.00	0.88	0.023	F	0.0116	0.0109	3.00	7242	70133	8.9	7.8	12.0	N
CB24F-(1/2)-PT	Naish et al	2008	15.00	12.00	36.00	0.88	0.023	F	0.0058	0.0055	6.00	6990	70133	8.4	7.2	10.6	N
CB33F	Naish et al	2008	18.00	12.00	60.00	0.88	0.019	F	0.0116	0.0112	3.00	6850	70133	8.1	7.0	12.2	Y
CB33D	Naish et al	2008	18.00	12.00	60.00	0.88	0.019	D	0.0163	0.0214	2.50	6850	70133	6.5	5.3	10.9	Υ*
316	Paulay et al	1974	31.00	6.00	40.00	1.00	0.013	D	N/A	N/A	4.00	4825	41800	N/A	N/A	N/A	N
317	Paulay et al	1974	31.00	6.00	40.00	1.00	0.013	D	N/A	N/A	4.00	7348	44400	N/A	N/A	N/A	N
395	Paulay et al	1974	39.00	6.00	40.00	1.00	0.012	D	N/A	N/A	4.00	5150	37600	N/A	N/A	N/A	N
CB1	Poudel et al	2018	18.00	10.00	34.00	0.88	0.024	F	0.0082	0.0089	3.00	6000	62000	7.3	6.5	10.0	N
CB1A	Poudel et al	2018	18.00	10.00	34.00	0.88	0.024	F	0.0082	0.0089	3.00	6400	62000	7.4	6.2	9.2	N
CCB40	Jang et al	2018	11.81	7.87	23.62	0.38	0.011	F	0.0158		1.97	6048	69474	5.0	3.9	6.8	N
CCB80	Jang et al	2018	11.81	7.87	23.62	0.38	0.011	F	0.0158	0.0122	1.97	12372	69474	4.4	3.2	5.5	N
1DF0Y	Shin et al	2014	11.81	9.84	41.34	1.00	0.032	F	0.0199	0.0161	4.72	4235	69329	10.9	9.6	23.1	Y
CB-2A	Tassios et al	1996	19.70	5.12	19.70	0.39	0.006	D	0.0160	0.0160	2.00	4133	60000	4.4	2.2	0.7	Y*
CB-2B	Tassios et al	1996	11.81	5.12	19.70	0.39	0.010	D	0.0160	0.0160	2.00	3810	60000	5.1	2.2	1.6	Y*
X1	Tegos et al	1988	7.90	7.90	15.80	0.38	0.004	F	0.0107	0.0107	3.00	2990	47140	3.5	3.1	20.4	N

*Compliant, except for ACI 318-19 Section 18.10.7.4(c). $A_{sh,y}/A_{sh,req'd} = 0.31$ and $A_{sh,x}/A_{sh,req'd} = 0.46$ for DCB-2. $A_{sh,y}/A_{sh,req'd} = 0.39$ and $A_{sh,x}/A_{sh,req'd} = 0.22$ for CCB-11. $A_{sh,y}/A_{sh,req'd} = 0.90$ and $A_{sh,x}/A_{sh,req'd} = 1.19$ for CB24D and CB33D. $A_{sh,y}/A_{sh,req'd} = 0.55$ and $A_{sh,x}/A_{sh,req'd} = 0.55$ for CB-2A. $A_{sh,y}/A_{sh,req'd} = 0.60$ and $A_{sh,x}/A_{sh,req'd} = 0.60$ for CB-2B.

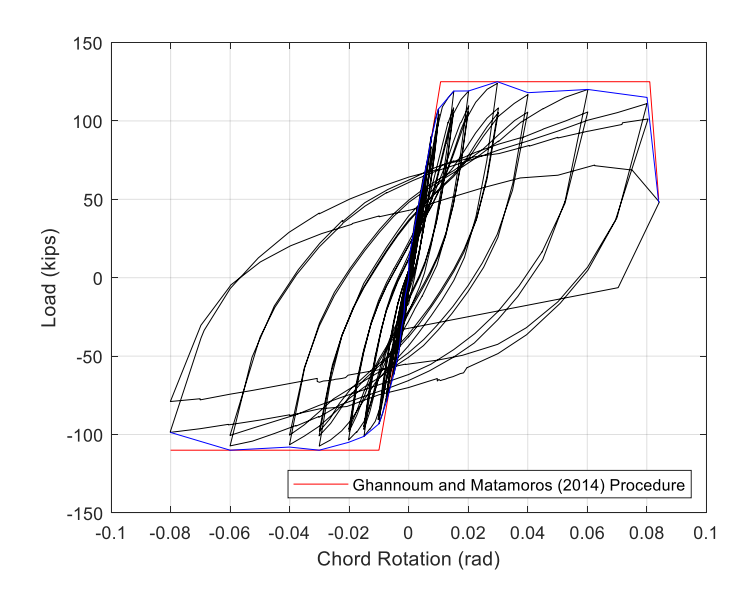


Figure 3.1. Ghannoum and Matamoros (2014) Backbone Model Fit to CB33F

As shown in Table 3.1, the 12 beams with transverse reinforcement confining each diagonal bundle were non-compliant with ACI 318-19. Fourteen of the 30 specimens that utilized full-section confinement were non-compliant with ACI 318-19. A footnote in Table 3.1 indicates which coupling beams did not satisfy Section 18.10.7.4(c)(ii) but satisfied the other provisions in ACI 318-19. ACI 318-19 Section 18.10.7.4(c)(ii) prescribes that A_g for diagonal bundles be calculated assuming the concrete cover specified in Section 20.5.1 is provided on all four sides of the bundle. As an indication of the margin by which this provision was not satisfied, the footnote in Table 3.1 provides the ratio of transverse reinforcement provided to that required by the provision in both the x- and y- cross-sectional direction. Due to the lack of correlation between the level of transverse reinforcement and the deformation capacity indicated by d, as well as the large values attained for d in some instances, these six beams were treated as ACI 318-19 compliant for subsequent analysis.

Statistical values of *d* and *a* were determined from the subset of database tests that reached 20% strength degradation. Values for *d* and *a* that were not included in this subset are indicated by a shaded cell in Table 3.1. Beams in the database that were ACI 318-19 compliant had an average *a* of 6.0% rotation with a coefficient of variation of 29% and an average *d* of 7.3% rotation with a coefficient of variation of 23%. Non-compliant beams had an average *a* of 5.5% rotation with a coefficient of variation of 37% and an average *d* of 6.6% rotation with a coefficient of variation of 32%. These values are well in excess of the ASCE-SEI 41-17 and ACI 374 recommended values of 3.0% rotation for *d*. This suggests that existing recommendations are overly conservative, and the formulation of new recommendations is appropriate.

Strength degradation in the force-deformation behavior of diagonally reinforced concrete coupling beams typically occurs due to concrete crushing or bar buckling. Parameters such as longitudinal reinforcement ratio, ρ , ratio of spacing of transverse reinforcement to diagonal bar diameter, s/d_b , ratio of area of transverse reinforcement to area of core concrete, ρ_t , and span-to-depth (aspect) ratio, L/h, were expected to influence deformation capacity. It is evident from Figure 3.2 that deformation capacity increases with an increase in ρ , ρ_t , and L/h and decreases with an increase in s/d_b . The r-value for linear correlation was 0.76 for ρ , 0.47 for ρ_t , 0.51 for L/h, and 0.56 for s/d_b . Modeling described in subsequent sections was used to further examine deformation capacity.

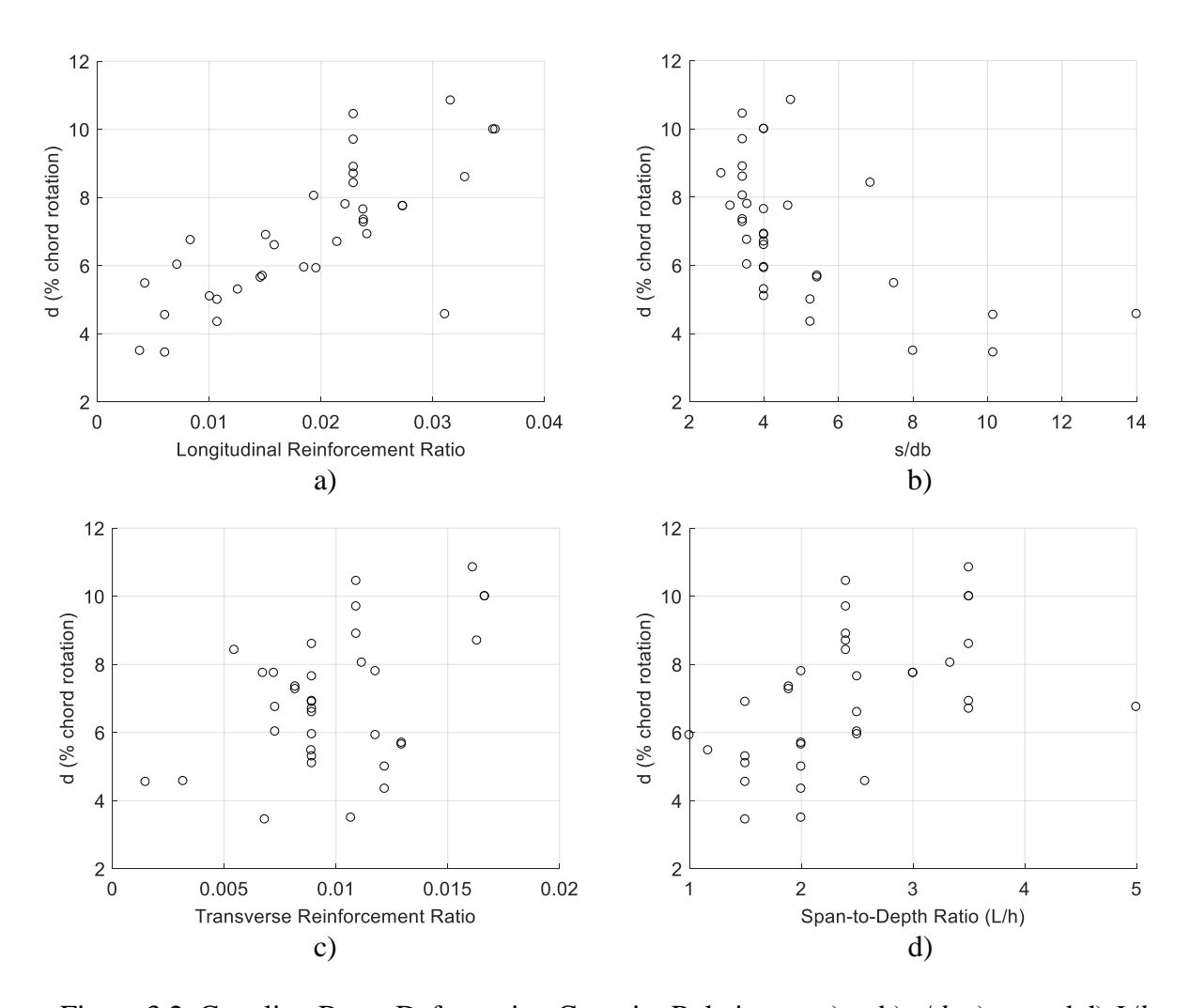


Figure 3.2. Coupling Beam Deformation Capacity Relative to: a) ρ , b) s/d_b c) ρ_t , and d) L/h

3.2 Deformation Capacity

3.2.1 Beam Model

3.2.1.1 Model Development

A deformation capacity model was developed, validated with test data, and used to better understand the parameters influencing deformation capacity of diagonally reinforced concrete coupling beams. The model, shown in Figure 3.3, is conceptually consistent with that formulated by Naish et al (2013b) and consists of an elastic frame element with a plastic hinge at each end and an additional moment rotation hinge that considers slip/extension of diagonal reinforcement embedded into the wall. Test data from Naish et al (2013a) has shown that plasticity in diagonally reinforced concrete coupling beams concentrates at the ends of the beam where the moment demand is the greatest. Bond slip contributes significantly to coupling beam deformation (Naish et al, 2013a), such that coupling beam deformation capacity models should consider bond slip. The Alsiwat and Saatcioglu (1992) bond slip model was used in this study, consistent with that used by Naish et al (2013b).

The model is based on initiation of damage at the ends of the beam. The majority of beams in the database showed damage initiating and concentrating at the ends of the beam. The exceptions were DCB-1 from Fortney et al (2008) and P12 from Galano et al (2000). DCB-1 did not have transverse reinforcement provided over the intersection of diagonal bars at mid-length of the beam and was reported to fail from buckling of diagonal reinforcement in this region. P12 did not satisfy ACI

318-19 provisions and had span-to-depth ratio of 1.5 with transverse reinforcement ratios and concrete strength that were relatively low compared to other beams in the database. Galano et al (2000) reported failure due to crushing of the concrete compression strut and instability of diagonal bars.

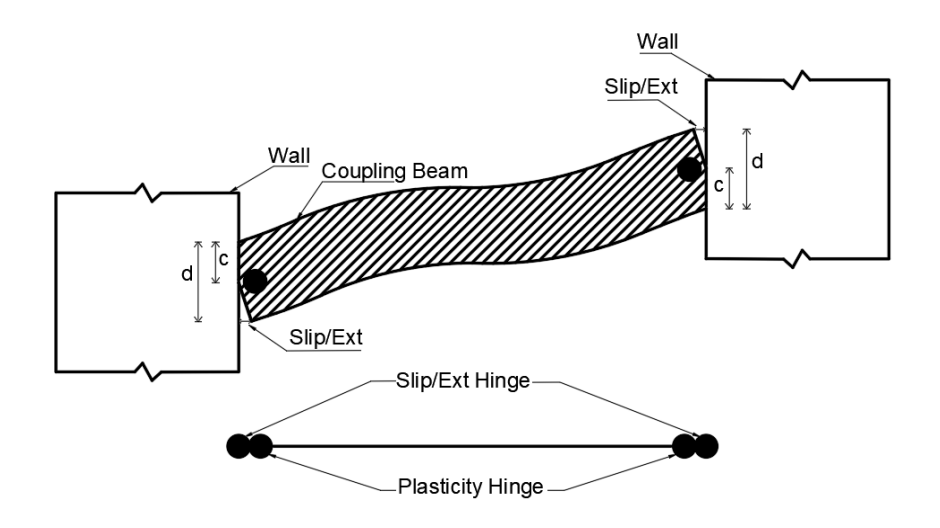


Figure 3.3. Diagonally Reinforced Coupling Beam Deformation Model

Consistent with the recommended values in ACI 318-19 Section A.8.4 and PEER TBI (2017), the elastic frame element was modeled with a flexural rigidity of $0.07 \left(\frac{L}{h}\right) E_c I_g$ and a shear rigidity of $0.4E_c A_g$, where L is the span length, h is the section height, E_c is the modulus of elasticity of concrete, I_g is the gross moment of inertia of the section, and A_g is the gross area of the section. In the plastic hinge model, the relationship between plastic rotation, θ_p , and plastic curvature, ϕ_p , is:

$$\theta_p = \phi_p L_p = (\phi - \phi_v) L_p \tag{3.1}$$

where L_p is the plastic hinge length, and ϕ and ϕ_y are the curvature and yield curvature, respectively, in the beam at the beam-wall interface. Based on plane section behavior, the following relationships exist between curvature and strain:

$$\phi = \frac{\varepsilon_c}{(c - c_c)} = \frac{\varepsilon_s}{(d_s - c)} = \frac{\varepsilon_s'}{(c - d_s')}$$
(3.2)

where ε_c is the concrete compressive strain at the outermost fiber of the confined concrete core, ε_s and ε_s' are the strain in the outermost diagonal reinforcement in tension and compression, respectively, c is the neutral axis depth, c_c is the concrete cover to the confined core, and d_s and d_s' are the effective depth to the outermost diagonal reinforcement in tension and compression, respectively. ϕ_s is computed as:

$$\phi_{y} = \frac{\varepsilon_{y}}{(d_{s} - c_{y})} \tag{3.3}$$

where ε_y is the yield strain of diagonal reinforcement, and c_y is the neutral axis depth at yielding of the outermost tension reinforcement. In this study, c and c_y were determined using plain strain fiber analysis. In Eq. (3.2) and Eq. (3.3), strain in the longitudinal direction was taken as the longitudinal component of the axial growth of the diagonal bar over L_p .

In addition to the longitudinal component of diagonal bar deformation, the transverse component of diagonal bar deformation was included in the model, which is more consistent with the strutand-tie modeling approach used by Barbachyn et al (2012), to reflect deep beam behavior. The transverse deformation from yielding of the diagonal reinforcement in both plastic hinges, δ_{tr} , is:

$$\delta_{tr} = 2(\varepsilon_s - \varepsilon_v) L_n \tan(\alpha) \tag{3.4}$$

In Eq. (3.4), strain in the transverse direction was taken as the transverse component of axial growth of the diagonal bar over $L_p \tan(\alpha)$. Plastic slip/extension of reinforcement at the interface, $\delta_{Pl\,slip/ext}$, was determined using the Alsiwat and Saatcioglu (1992) bond slip model. Elastic slip/extension was excluded from $\delta_{Pl\,slip/ext}$ due to flexibility from elastic bond slip being included in the effective stiffness terms recommended by PEER TBI (2017), which were used in the model. The resulting rotation from plastic slip/extension, $\theta_{Pl\,slip/ext}$, at the beam-wall interface is:

$$\theta_{Pl\,slip/ext} = \frac{\delta_{Pl\,slip/ext}*\cos(\alpha)}{(d_s - c)} \tag{3.5}$$

where α is the angle of the diagonal bars from horizontal, and the value for c is the same as that used in Eq. (3.2). The transverse component of plastic slip/extension in both ends of the beam, $\delta_{tr,slip/ext}$, is:

$$\delta_{tr,slip/ext} = 2\delta_{Pl\,slip/ext}\sin(\alpha) \tag{3.6}$$

For deformations larger than yielding, the total deformation, which is comprised of elastic flexure and shear, plastic flexure and shear, and bond slip/extension, is:

$$\delta = \frac{V_y L^3}{12\left[0.07\left(\frac{L}{h}\right)E_c I_g\right]} + \frac{V_y L}{0.4E_c A_g} + \theta_p \left(L - L_p\right)$$

$$+ 2(\varepsilon_s - \varepsilon_y) L_p \tan(\alpha) + \theta_{Pl \ slip/ext} L + 2\delta_{Pl \ slip/ext} \sin(\alpha) \tag{3.7}$$

where the shear at yielding, V_y , was determined by dividing the yield moment by the shear span, with the yield moment determined from plain strain fiber analysis of the cross-section at yielding in all tension reinforcement. This calculation for V_y was based on the assumption of flexural yielding, although Eq. (7) considers simultaneous deformation in flexure and shear from yielding of diagonal reinforcement. More detailed discussion, including justification for use of a flexural strength limit, is provided in Section 3.4. In Eq. (3.7), θ_p , $\theta_{Pl slip/ext}$, and $\delta_{Pl slip/ext}$ are strain-dependent, such that Eq. (3.7) provides a unique relationship between strain and deformation. Strain limits at onset of failure may be used to determine θ_p , $\theta_{Pl slip/ext}$, and $\delta_{Pl slip/ext}$ and to subsequently estimate deformation capacity using Eq. (3.7). For diagonally reinforced concrete coupling beams satisfying the provisions in ACI 318-19 Section 18.10.7, failure was typically due to buckling of diagonal reinforcement or crushing of core concrete. Existing models were used to estimate the strain at onset of crushing of confined concrete (Mander et al, 1988) and buckling (Rodriguez et al, 1999) of diagonal reinforcement.

The Mander et al (1988) confined concrete model was used for the computation of strain at the onset of crushing of core concrete. This model is based on an energy method that considers the onset of crushing of core concrete at the rupture of confining steel hoops. Priestley et al (1996) provided a conservative single-equation simplification of the Mander et al (1988) model for computing the strain at crushing of confined concrete, ε_{cu} , as:

$$\varepsilon_{cu} = 0.004 + \frac{1.4\rho_s f_{yh} \varepsilon_{su}}{f'_{cc}} \ge 0.005$$
 (3.8)

where f_{yh} is the transverse reinforcement yield stress, f'_{cc} is the confined concrete strength, ε_{su} is the transverse reinforcement steel strain at maximum stress, taken as 0.1, and ρ_s is the volumetric ratio of confining steel. For rectangular cross sections, ρ_s is defined as $\frac{A_{sx}}{sb_c} + \frac{A_{sy}}{sd_c}$ where A_{sx} and A_{sy} are the total area of transverse steel in the x- and y-directions of the cross-section, s is the spacing of transverse reinforcement along the length of the beam, b_c is the width of the concrete core measured to the centerline of the confining hoops, and d_c is the height of the concrete core measured to the centerline of the confining hoops. f'_{cc} was determined using Figure 4 from Mander et al (1988) for the computed ratios of the effective lateral confining stresses in the x- and y-directions of the cross-section, f'_{lx} and f'_{ly} , respectively, to the unconfined concrete strength. Mander et al (1988) specified f'_{lx} and f'_{ly} as:

$$f'_{lx} = k_e \frac{A_{sx}}{sd_c} f_{yh} \tag{3.9a}$$

$$f'_{ly} = k_e \frac{A_{sy}}{sb_c} f_{yh} (3.9b)$$

where k_e is the confinement effectiveness coefficient. For a rectangular cross-section, Mander et al (1988) defined k_e as:

$$k_e = \frac{\left(1 - \sum_{i=1}^{n} \frac{\left(w_i'\right)^2}{6b_c d_c}\right) \left(1 - \frac{s'}{2b_c}\right) \left(1 - \frac{s'}{2d_c}\right)}{(1 - \rho_{cc})}$$
(3.10)

where w_i is the *i*th clear distance between adjacent longitudinal or diagonal bars, s' is the clear spacing between hoops, and ρ_{cc} is the ratio of the area of longitudinal steel to area of core concrete.

Bar buckling was modeled using the following equations provided by Motter et al (2018), which were an extension of the bar buckling model and test data provided by Rodriguez et al (1999):

$$\varepsilon_p^* = 0.03 - 0.00167 \left(\frac{s}{d_b} - 6\right)$$
 when $6 \le \frac{s}{d_b} \le 16$ (3.11a)

$$\varepsilon_p^* = 0.09 - 0.015 \left(\frac{s}{d_b} - 2 \right)$$
 when $\frac{s}{d_b} < 6$ (3.11b)

where ε_p^* is the recompression buckling strain, s is the spacing of transverse reinforcement along the diagonal bar, and d_b is the bar diameter of the diagonal reinforcement. Based on the strain relationship shown in Figure 3.4:

$$\varepsilon_p^* = \varepsilon_s' + \varepsilon_s - \varepsilon_y \tag{3.12}$$

where the value used for ε_s' is the peak compression strain for the loading excursion at which bar buckling is being assessed, and the value used for ε_s is the peak tensile strain prior to this loading excursion. For fully reversed-cyclic (i.e., symmetric) loading protocols on a symmetric cross-section, relationships for plane-strain behavior in Eq. (3.2) can be substituted into Eq. (3.12) to produce:

$$\varepsilon_p^* = \phi(d_s - d_s') - \varepsilon_y \tag{3.13}$$

Eq. (3.11) can be used to determine ε_p^* based on s/d_b , and the resulting ε_p^* can be used in Eq. (3.13) to determine the curvature at the peak of the loading excursion immediately prior to the onset of diagonal reinforcement buckling during the subsequent loading excursion.

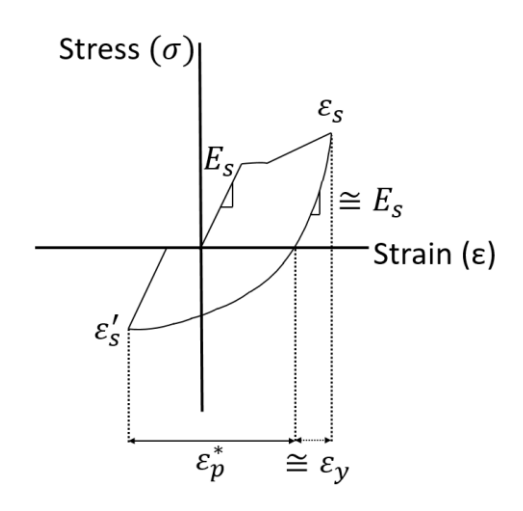


Figure 3.4. Compression Reloading Strain

In this study, c, ϕ_y , and c_y were determined from monotonic moment-curvature analysis. The stress-strain relationship used for diagonal reinforcement was quadra-linear with f_y and f_u taken as the tested values, an elastic modulus of 29000 ksi, a yield plateau with constant stress, linear strain hardening with a modulus of 1000 ksi and onset at a strain of 0.01, and constant stress beyond the strain at which ultimate stress was reached. The Mander et al (1988) confined concrete model was used for core concrete in combination with zero stress in the cover concrete on the basis that cover concrete had spalled. For beams which utilized confinement of each group of diagonal bars, the core concrete was considered to consist of the area of concrete within one of the diagonal bundles, measured to the centerline of the confining hoops. For each coupling beam in the database, a value of c was determined for both of the potential failure modes considered. At the onset of bar buckling, c was determined from moment-curvature analysis for the value of ϕ determined from

Eq. (3.13). At the onset of crushing of confined concrete, c was determined from moment-curvature analysis for the value of ε_{cu} determined from Eq. (3.8). Eq. (3.7) was used to determine the level of deformation at which these strain limit states occurred, with the lesser of the two limits indicating the predicted failure mechanism.

The use of monotonic moment-curvature analysis did not consider the axial elongation strain caused by loading cycles (Lee and Watanabe, 2003). Axial elongation strain for a given curvature would reduce the peak concrete compressive strain but would not change the curvature at bar buckling in Eq. (3.13), as $\varepsilon_s' + \varepsilon_s$ would remain constant in Eq. (3.12). As the majority of beams examined in this study failed in bar buckling rather than concrete crushing, with more detailed information provided in subsequent sections, use of monotonic moment-curvature analysis was deemed sufficient for determining curvature. Similarly, for the bond slip component of the model, determination of c from monotonic moment-curvature analysis was consistent with the monotonic bond slip model (Alsiwat and Saatcioglu, 1992) that was used. Increase in reinforcement bond slip from loading cycles is expected to be nearly the same at each end of a beam with symmetric cross-section for a fully-reversed cyclic loading protocol. As the majority of the beams in the database had symmetric cross-sections and were tested using fully-reversed cyclic loading protocols, the use of a more refined approach that modeled the cyclic bond slip contribution was deemed unnecessary.

3.2.1.2 Model Validation

Based on the model, the relationship between deformation and strain is dependent on the extent of plasticity, which is reflected by the plastic hinge length, L_p , in Eq. (3.7) and Eq. (3.1). A potential increase in the spreading of plasticity along the length of a diagonally reinforced concrete coupling beam, compared to a conventionally reinforced beam, could occur due to the reduction in moment resistance that occurs along the beam as the lever arm to the tension reinforcement decreases with the decrease in d_s . Therefore, the selection of L_p was examined using the data rather than adopting existing recommendations for L_p in reinforced concrete beams. Using load vs displacement data from LVDTs that were placed along the length of the coupling beams from Naish (2013), it was determined that plastic rotation concentrated in the ends of the beams within the LVDTs at these locations. The LVDTs used in the tests by Naish (2013) had a length equal to half the beam depth, such that plasticity was determined to be limited to within 0.5h of the beam ends. In the model, L_p was considered as a multiple of the beam depth, h, as well as a multiple of the length of the beam, L. Plastic hinge lengths that are a multiple of h are used in ASCE 41 and ACI 318. Beam length was considered to investigate use of a plastic hinge length that better accounts for spreading of plasticity due to variation in moment gradient. Recognizing that the angle of inclination of the diagonal bar may influence the spread of plasticity, consideration was also given to defining the plastic length along the diagonal bar as a multiple of L or h. This produced L_p values that were multiples of $L * \cos(\alpha)$ and $h * \cos(\alpha)$, noting that L_p represents the horizontal length from the beam-wall interface in which plasticity will spread along the beam.

In Table 3.2 and Figure 3.5, predicted rotations at failure using the recommended deformation capacity model are provided with the measured rotations at failure. Results are shown for plastic hinge lengths of 1.5h and 1.5h $\cos(\alpha)$, 1.0h and 1.0h $\cos(\alpha)$, 0.5h and 0.5h $\cos(\alpha)$, 0.5L and $0.5L\cos(\alpha)$, 0.375L and $0.375L\cos(\alpha)$, and $0.25L\cos(\alpha)$. An upper limit of 0.5L was used for L_p as this reflects a fully plastic beam. The average and coefficient of variation of error, determined as the ratio of the difference between the modeled and measured deformation capacity to the modeled deformation capacity, and linear regression lines for each plastic hinge length considered are provided in Figure 3.5. The seven beams in the database that did not reach 20% strength loss during testing were excluded. The two tests in Figure 3.5 in which deformation capacity is significantly overpredicted are Specimens C6 and C8 tested by Barney et al (1980). Despite having relatively low s/d_b in the span of the beam, it was reported that, at the later stages of testing, buckling of diagonal reinforcement occurred within the abutment walls where no reinforcement was provided to resist bar buckling. The model prediction in Figure 3.5 was based on s/d_b in the beam span. An increase in s/d_b in the proposed model, reflecting the lack of reinforcement provided within the abutment walls, leads to a decrease in predicted deformation capacity, consistent with the overprediction of Specimens C6 and C8. In addition to the lack of restraint against bar buckling in the embedment zone, Specimen C8 had L/h=5.0, which is in excess of the ACI 318-19 limit of L/h=4.0 for diagonally reinforced concrete coupling beams. Barney et al (1980) suggested that, at this span-to-depth ratio, diagonal reinforcement becomes ineffective and the diagonally reinforced beam behaves in a manner consistent with conventionally reinforced beams, which typically have lower deformation capacity due to sliding shear. Specimen C8 was the only beam in the dataset with L/h greater than 3.5. Results and trendlines for the proposed model with the exclusion of Specimens C6 and C8 are shown in Figure 3.6. It is evident from Figure 3.6 that the trendlines of the results from the proposed model better match test data with the exclusion of these two tests.

Table 3.2. Deformation Capacity and Failure Mechanism Predicted by Model

Specimen	20% Strength	Confinement	Predicted	d_measured	d_model (L_p =											
	Loss?		Mechanism	(% Rot)	1.5*h)	1.0*h)	0.5*h)	1.5*h*cos(α)				0.375*L*cos(α))		0.5*L) (% Rot)	0.375*L)	0.25*L) (% Rot)
C6	Y	F	BB	(% Rot) 6.0	(% Rot) 13.2	(% Rot) 12.3	(% Rot) 9.5	(% Rot) 13.0	(% Rot) 11.3	(% Rot) 8.8	(% Rot) 12.3	(% Rot) 11.0	(% Rot) 9.5	(% R0t)	(% Rot) 12.0	(% Rot) 10.3
C8	Y	F	BB	6.8	14.1	11.8	8.7	13.7	11.4	8.4	16.3	15.0	12.7	16.5	15.4	13.0
DCB-1	Ý	D	BB	4.6	2.1	2.0	1.5	2.1	2.0	1.5	2.1	2.0	1.7	2.1	2.0	1.7
DCB-2	N	D	BB	10.0	12.4	11.1	8.0	12.4	11.0	7.9	12.4	11.5	9.7	12.4	11.6	9.8
P07	Y	F	BB	4.6	2.2	2.2	1.8	2.2	2.2	1.6	2.0	1.7	1.4	2.2	1.9	1.5
P12	Ý	D	BB	3.5	2.1	2.1	1.7	2.1	2.1	1.6	2.0	1.7	1.3	2.1	1.8	1.4
SD-2.0	Y	F	BB	5.7	4.4	4.4	3.3	4.4	4.3	3.2	4.3	3.9	3.2	4.4	4.0	3.3
BD-2.0	Ý	F	BB	5.7	4.4	4.4	3.3	4.4	4.3	3.2	4.3	3.9	3.2	4.4	4.0	3.3
SD-3.5	Y	F	BB	10.0	11.4	10.0	7.4	11.4	10.0	7.4	11.7	11.0	9.4	11.7	11.0	9.5
BD-3.5	Y	F	BB	10.0	11.5	10.1	7.4	11.5	10.0	7.4	11.8	11.1	9.5	11.8	11.1	9.5
D80-1.5	Y	F	BB	6.9	6.3	6.3	5.4	6.3	6.3	5.2	6.1	5.5	4.6	6.3	5.7	4.7
D100-1.5	Y	F	BB	5.3	5.7	5.7	4.8	5.7	5.7	4.6	5.5	4.9	4.0	5.7	5.1	4.2
D120-1.5	Y	F	BB	5.1	7.2	7.2	6.3	7.2	7.2	6.1	7.1	6.4	5.5	7.2	6.6	5.7
D80-2.5	Y	F	BB	7.7	7.3	6.9	5.1	7.3	6.8	5.0	7.3	6.7	5.6	7.3	6.7	5.7
D100-2.5	Y	F	BB	6.0	6.9	6.5	4.6	6.9	6.4	4.6	6.8	6.2	5.1	6.9	6.3	5.2
D120-2.5	Y	F	BB	6.6	8.1	7.7	5.9	8.1	7.6	5.8	8.1	7.5	6.4	8.1	7.5	6.4
D80-3.5	Y	F	BB	8.6	10.3	8.9	6.4	10.3	8.9	6.3	10.6	9.9	8.3	10.6	9.9	8.4
D100-3.5	Y	F	BB	6.9	8.2	7.0	4.8	8.2	6.9	4.7	8.4	7.8	6.5	8.4	7.8	6.5
D120-3.5	Y	F	BB	6.7	9.2	8.0	5.8	9.2	7.9	5.7	9.4	8.8	7.5	9.5	8.9	7.5
CCB11	Y	О	BB	5.5	2.4	2.4	2.2	2.4	2.4	1.9	2.1	1.7	1.3	2.4	2.0	1.5
CB10-1	Y	F	BB	5.9	6.6	6.6	6.6	6.6	6.6	6.4	6.4	5.7	4.9	6.6	6.0	5.1
CB20-1	Y	F	BB	7.8	8.2	8.2	6.4	8.2	8.1	6.3	8.1	7.4	6.3	8.2	7.5	6.4
CB30-DA	Y	D	BB	7.8	8.0	7.3	5.4	8.0	7.2	5.4	8.0	7.5	6.5	8.0	7.6	6.5
CB30-DB	Y	F	BB	7.8	11.5	10.3	7.6	11.5	10.3	7.6	11.5	10.7	9.1	11.5	10.8	9.2
CB24F	Y	F	BB	9.7	9.1	8.7	6.4	9.1	8.5	6.3	9.0	8.2	6.9	9.1	8.3	7.0
CB24D	Y	D	BB	8.7	9.9	9.5	7.0	9.9	9.4	6.9	9.9	9.0	7.5	9.9	9.1	7.6
CB24F-RC	Y	F	BB	10.5	9.0	8.6	6.3	9.0	8.5	6.2	8.9	8.1	6.8	9.0	8.3	6.9
CB24F-PT	Y	F	BB	8.9	9.1	8.7	6.5	9.1	8.6	6.3	9.1	8.3	6.9	9.1	8.4	7.0
CB24F-(1/2)-PT	Y	F	BB	8.4	4.1	3.9	3.0	4.1	3.9	3.0	4.1	3.8	3.2	4.1	3.8	3.3
CB33F	Y	F	BB	8.1	9.7	8.3	5.7	9.6	8.2	5.6	9.9	9.1	7.5	9.9	9.2	7.6
CB33D	N	D	BB	6.5	10.6	9.1	6.2	10.6	9.0	6.1	10.8	9.9	8.2	10.8	10.0	8.3
316	N	D	N/A	N/A	N/A	N/A	N/A	N/A	N/A	N/A	N/A	N/A	N/A	N/A	N/A	N/A
317	N	D	N/A	N/A	N/A	N/A	N/A	N/A	N/A	N/A	N/A	N/A	N/A	N/A	N/A	N/A
395	N	D	N/A	N/A	N/A	N/A	N/A	N/A	N/A	N/A	N/A	N/A	N/A	N/A	N/A	N/A
CB1	Y	F	BB	7.3	8.2	8.2	6.6	8.2	8.2	6.4	8.1	7.4	6.3	8.2	7.6	6.4
CB1A	Y	F	BB	7.4	8.1	8.1	6.5	8.1	8.1	6.4	8.0	7.3	6.2	8.1	7.5	6.3
CCB40	Y	F	BB	5.0	4.5	4.5	3.3	4.5	4.4	3.2	4.4	4.0	3.2	4.5	4.0	3.3
CCB80	Y	F	BB	4.4	4.2	4.2	3.1	4.2	4.2	3.0	4.2	3.7	3.0	4.2	3.8	3.1
1DF0Y	Y	F	BB	10.9	10.3	9.1	7.0	10.2	9.1	7.0	10.5	9.9	8.6	10.5	9.9	8.7
CB-2A	N	D	BB	4.4	3.6	3.6	3.6	3.6	3.6	3.5	3.5	3.0	2.5	3.6	3.2	2.6
CB-2B	N	D	BB	5.1	5.2	5.2	4.2	5.2	5.2	4.1	5.0	4.5	3.7	5.2	4.7	3.9
X1	Y	F	BB	3.5	3.8	3.8	2.8	3.8	3.5	2.5	3.5	3.1	2.5	3.8	3.4	2.8

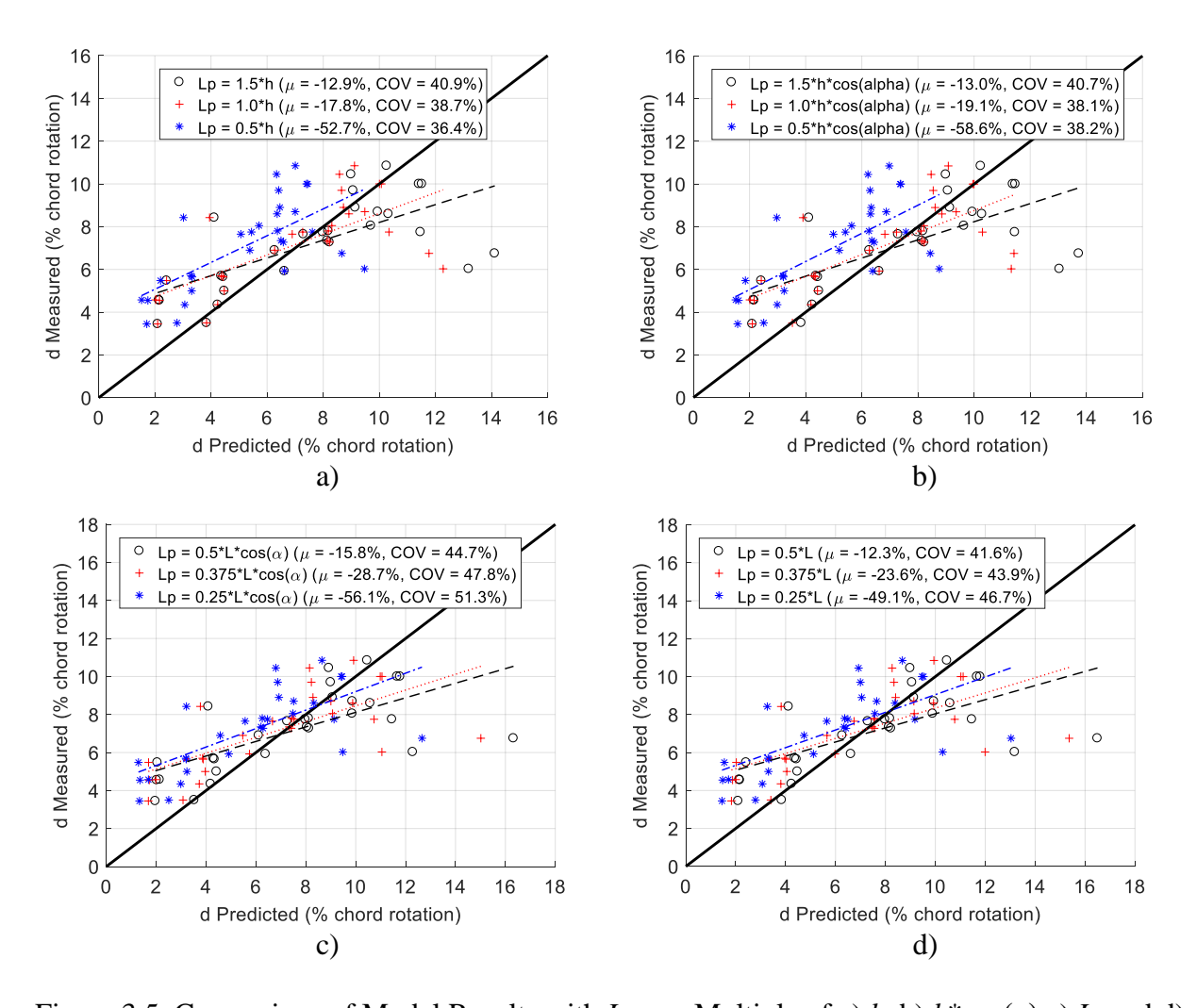


Figure 3.5. Comparison of Model Results with L_p as a Multiple of a) h, b) $h*\cos(\alpha)$ c) L, and d) $L*\cos(\alpha)$

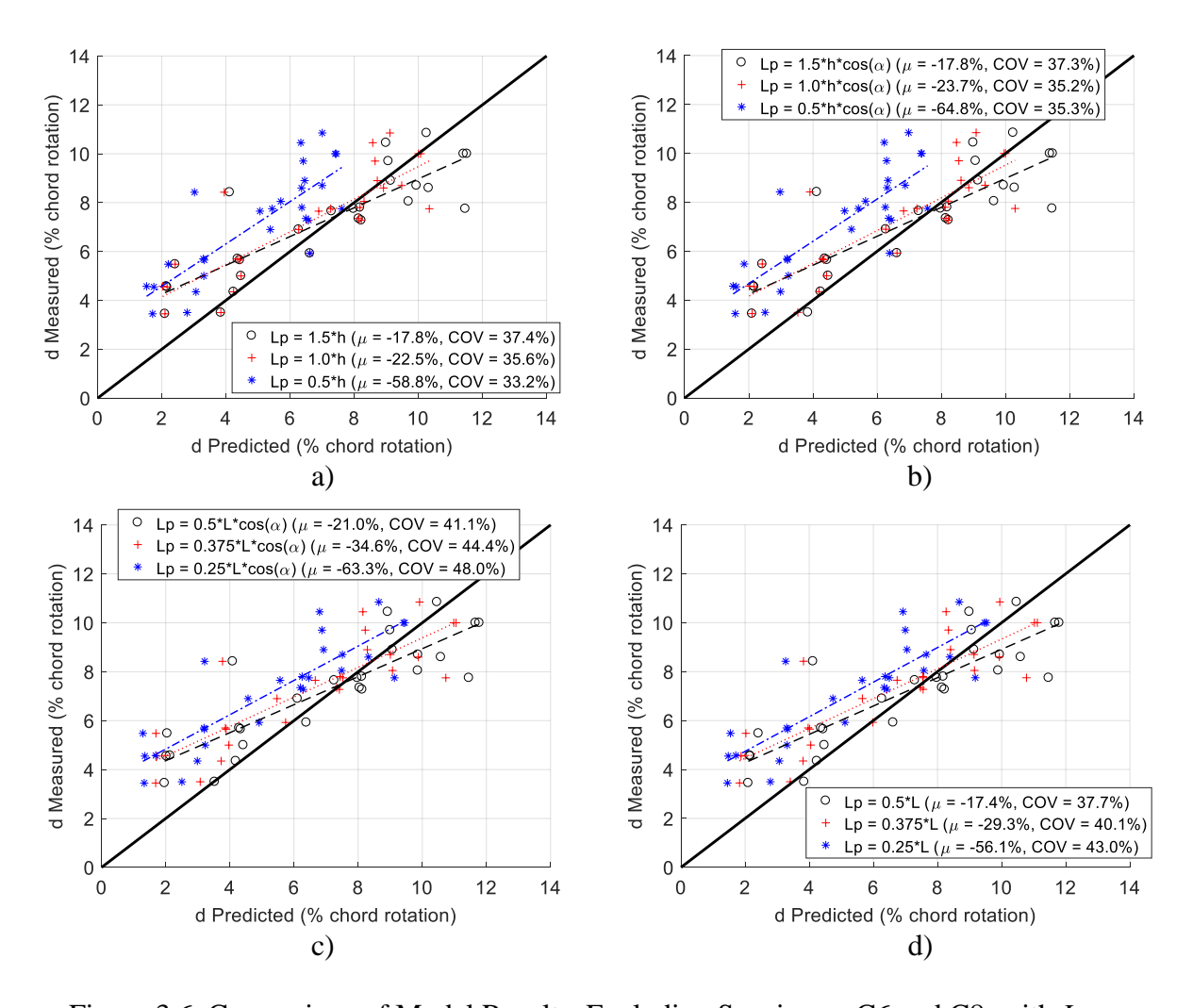


Figure 3.6. Comparison of Model Results, Excluding Specimens C6 and C8, with L_p as a Multiple of a) h, b) $h*\cos(\alpha)$ c) L, and d) $L*\cos(\alpha)$

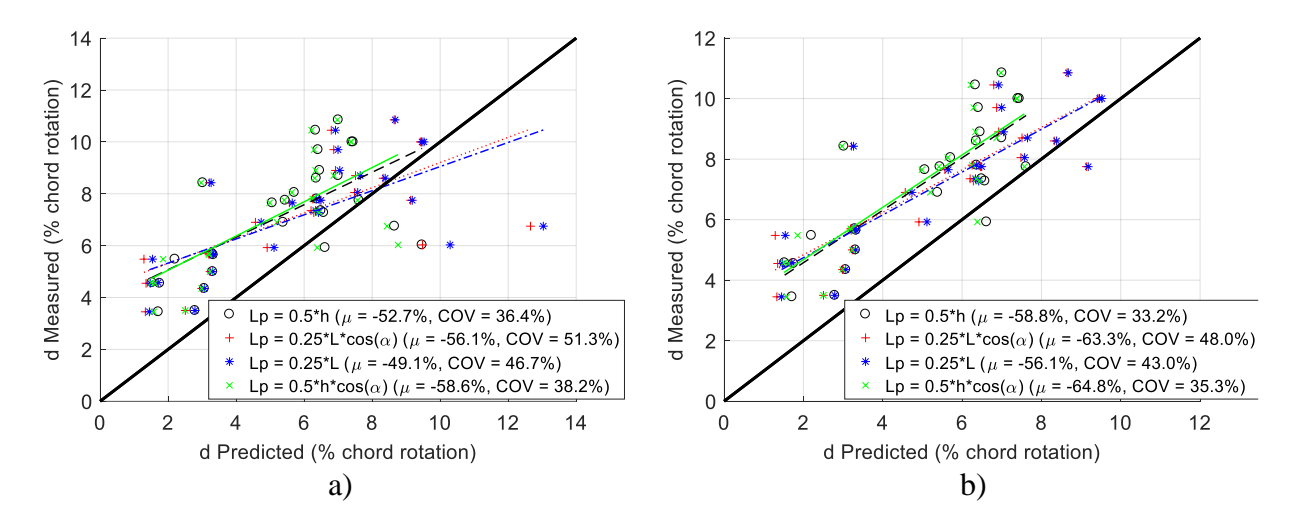


Figure 3.7. Select Model Results with L_p as a Multiple of h, $h*\cos(\alpha)$, L, and $L*\cos(\alpha)$, a) Including Specimens C6 and C8, and b) Excluding Specimens C6 and C8

Model results using select values for L_p for each definition of plastic hinge length considered are provided in Figure 3.7 to facilitate comparison. It is evident from the trendlines in Figure 3.7 that the inclusion of $\cos(a)$ in the definitions of plastic hinge length had little effect on the fit of modeling results to test data. Among all plastic hinge lengths considered, $L_p=0.5L$ provided the lowest absolute average error while $L_p=0.5h$ provided the least amount of scatter. The use of $L_p=0.5L$ was deemed unreasonable, as the beam would be fully plastic, and beams failing in bar buckling typically had damage concentrated at the ends. The use of $L_p=0.5h$ in the proposed deformation capacity model is recommended, as this is more consistent with observed damage, resulted in a trendline in Figure 3.5a with a slope closest to 1.0, and provided the least amount of under-prediction. Considering all tests with normal strength reinforcement that also reached 20% strength loss, the slope of the trendline was 0.63 but increased to 0.87 when excluding Specimens C6 and C8. The under-prediction of the trendline was deemed reasonable, given that the bar buckling equations used (Eq. 3.11) were lower bound values for the onset of bar buckling and that

20% strength loss may occur after the onset of bar buckling. Due to the expected under-prediction, it is recommended to increase the model results by 2.25% chord rotation to provide a best estimate for deformation capacity, as this reduces the average error to 0.1% when excluding Specimens C6 and C8. Use of a best estimate for deformation capacity is consistent with the approach used by Ghannoum and Matamoros (2014), in which recommended values for the modeling parameters "a" and "b" for columns were selected as the best estimates in order be used in backbone models to produce median values from nonlinear time history analyses.

Buckling of diagonal reinforcement was predicted as the failure mechanism for all beams in the database in which enough information was provided to make a prediction of the failure mechanism. An attempt was made to determine if the predicted failure mechanism matched the reported damage photos and failure mechanisms. Beams predicted to fail due to buckling of diagonal reinforcement generally had large cracks with visibly buckled bars and considerable spalling of cover concrete. It is evident from test data in Figure 3.2b that a decrease in s/d_b correlates with an increase in d, and this is attributed to the increased resistance to bar buckling from reduced s/d_b .

In Figure 3.8, the test data from Figure 3.2 are plotted with the predicted deformation capacity using the proposed model (with $L_p=0.5h$ and the 2.25% chord rotation increase). It is evident from Figure 3.8 that the trends in deformation capacity with respect to ρ , s/d_b , ρ_t , and L/h are consistent between test data and the proposed model.

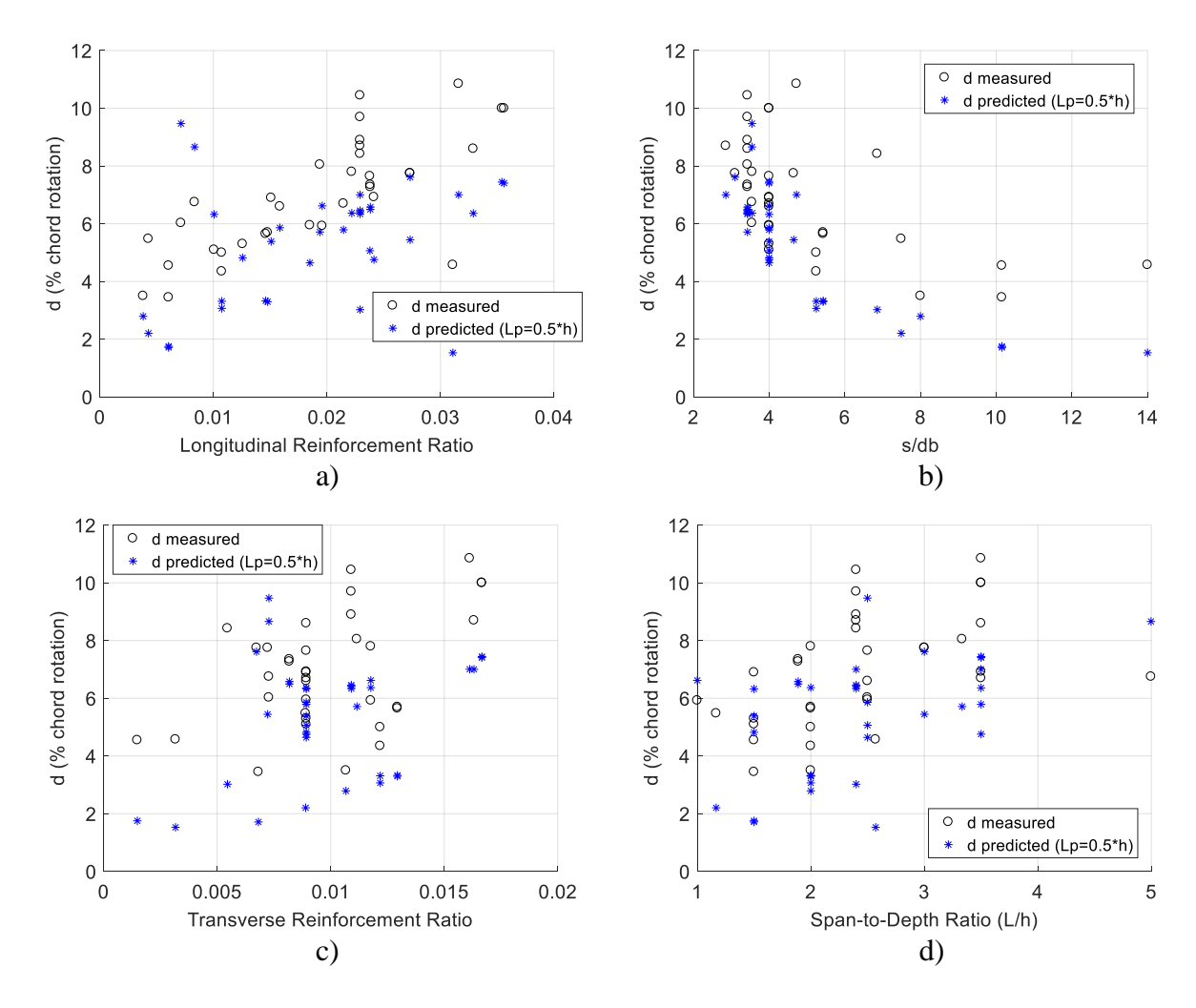


Figure 3.8. Predicted Coupling Beam Deformation Capacity Relative to: a) ρ , b) s/d_b , c) ρ_t , and d) L/h

Consideration was given to including a limit state for diagonal compression failure in the refined model. To investigate this, the limit of $10\sqrt{f_c'}b_wd$ from ACI 318-19 Section 18.10.7.4 was compared to the peak measured strength during testing. In many instances the $10\sqrt{f_c'}b_wd$ limit was exceeded without a diagonal compression failure occurring. In addition, the observed damage in the majority of tests was inconsistent with diagonal compression failure. For these reasons, the $10\sqrt{f'c}b_wd$ shear limit was excluded from the refined model. A more detailed discussion on this limit is presented in Section 3.4.

One of the limitations of the model was applicability to diagonally reinforced concrete coupling beams with high strength reinforcement (e.g., Grade 100). The Rodriguez et al (1999) bar buckling equations were calibrated with experimental data that did not include high strength reinforcement. The increase in yield and ultimate stress in high strength reinforcement allows for higher forces to be carried by the diagonal reinforcement and may allow for buckling of reinforcement to occur at lower strain levels than predicted by the Rodriguez et al (1999) bar buckling equations. This is highlighted by the overprediction of deformation capacity when using the recommended model (with a plastic hinge length of $L_p = 0.5h$ and 2.25% chord rotation increase) for the following six beams with Grade 100 or Grade 120 reinforcement tested by Weber-Kamin et al (2019): D100-1.5, D120-1.5, D100-2.5, D120-2.5, D100-3.5, and D120-3.5. Therefore, test beams using Gr. 100 or 120 reinforcement were excluded from comparisons between model and test data.

3.2.3 Empirical Model

Relative to the model presented in the previous section, a less-refined empirical model to determine d was formulated. Least squares regression was performed on the data shown in Figure 3.2 to formulate the following empirically-derived equation to determine d:

$$d = 5.3 + 110\rho - 0.3\frac{s}{d_h} + 20\rho_t + 0.5\frac{L}{h}$$
(3.14)

The average of the ratio of the measured value of d to the predicted using Eq. (3.14) was 0.97 with coefficient of variation of 16%. For this dataset, ρ was found to increase as L/h increased, and s/d_b was found to decrease as ρ_t increased. It was reported in the previous section that the refined model

predicted failure due to bar buckling rather than concrete crushing for the majority of the tests. Strain at bar buckling was dependent on s/d_b , while strain at crushing was dependent on ρ_t . Since crushing was not expected, exclusion of ρ_t from the regression was examined. Exclusion of L/h was also examined, due to correlation between L/h and ρ . Least squares regression performed using ρ and s/d_b as independent variables led to the following equation for d:

$$d = 6.15 + 140\rho - 0.35 \frac{s}{d_b} \tag{3.15}$$

The average of the ratio of the measured value of d to the predicted using Eq. (3.15) was 1.00 with coefficient of variation of 16%. Therefore, the more refined Eq. (3.14) does not offer improvement over Eq. (3.15) in predicting d for this dataset. When conducting least squares regression with a single independent variable, d was found to have a stronger correlation with ρ than s/d_b (0.76 and 0.56, respectively). Least squares regression with ρ as the independent variable led to the following equation for d:

$$d = 3.5 + 180\rho \tag{3.16}$$

The average of the ratio of the measured value of d to the predicted using Eq. (3.16) was 1.00 with coefficient of variation of 18%. Therefore, the inclusion of s/d_b in Eq. (3.15) relative to Eq. (3.16) led to a slight reduction in variability and better accounted for the influence of s/d_b , with the fit between predicted and measured d provided in Figure 3.9. Eq. (3.15) provides an average value, while the following equation, formulated from least squares regression, provides a mean minus standard deviation of d:

$$d = 6.1 + 140\rho - 0.4 \frac{s}{d_h} \tag{3.17}$$

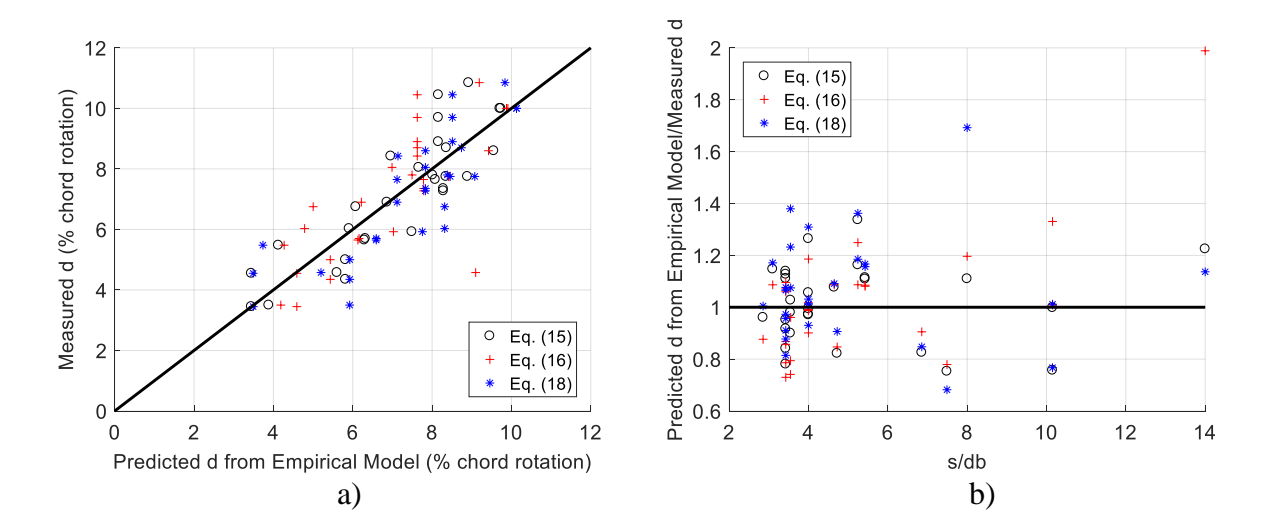


Figure 3.9. a) Comparison of Predicted d using Empirical Model to Measured d, b) Comparison of Ratio of Predicted to Measured d to s/d_b

Despite the correlation between d and ρ in the test data, prediction of d from the refined model is not overly sensitive to changes in ρ . The refined model is sensitive to changes in bar diameter of diagonal reinforcement, as bond slip is dependent on bar diameter. If bar diameter is normalized to the depth of the beam as d_b/h , a correlation of r = 0.80 was found between ρ and d_b/h . The correlation between the measured d and d_b/h was r = 0.70, compared to r = 0.76 for d and ρ . The increase in measured d with increase in ρ may be caused by the increase in d_b/h with increase in ρ for the dataset. Given that the refined model is sensitive to d_b/h and not ρ , least squares regression was performed using s/d_b and d_b/h as independent variables to produce:

$$d = 5.8 + 70\frac{d_b}{h} - 0.40\frac{s}{d_b} \tag{3.18}$$

The average of the ratio of the measured value of d to the predicted using Eq. (3.18) was 0.99 with coefficient of variation of 18%. Although this coefficient of variation is larger than 16% for Eq. (3.15) with ρ , the use of Eq. (3.18) is recommended over Eq. (3.15), as use of d_b/h rather than ρ is consistent with the sensitivity of these parameters in the refined model. The use of $d_b*cos(\alpha)/h$ rather than d_b/h was investigated but led to minimal changes to the predicted d and coefficient of variation. Eq. (3.18) provides an average value, while the following equation, formulated from least squares regression, provides a mean minus standard deviation of d:

$$d = 4.9 + 55 \frac{d_b}{h} - 0.50 \frac{s}{d_b} \tag{3.19}$$

For the beams in the database, predicted and measured d versus d_b/h and s/d_b are provided in Figure 3.10. Predicted d using the proposed refined model are included in Figure 3.10 for comparison.

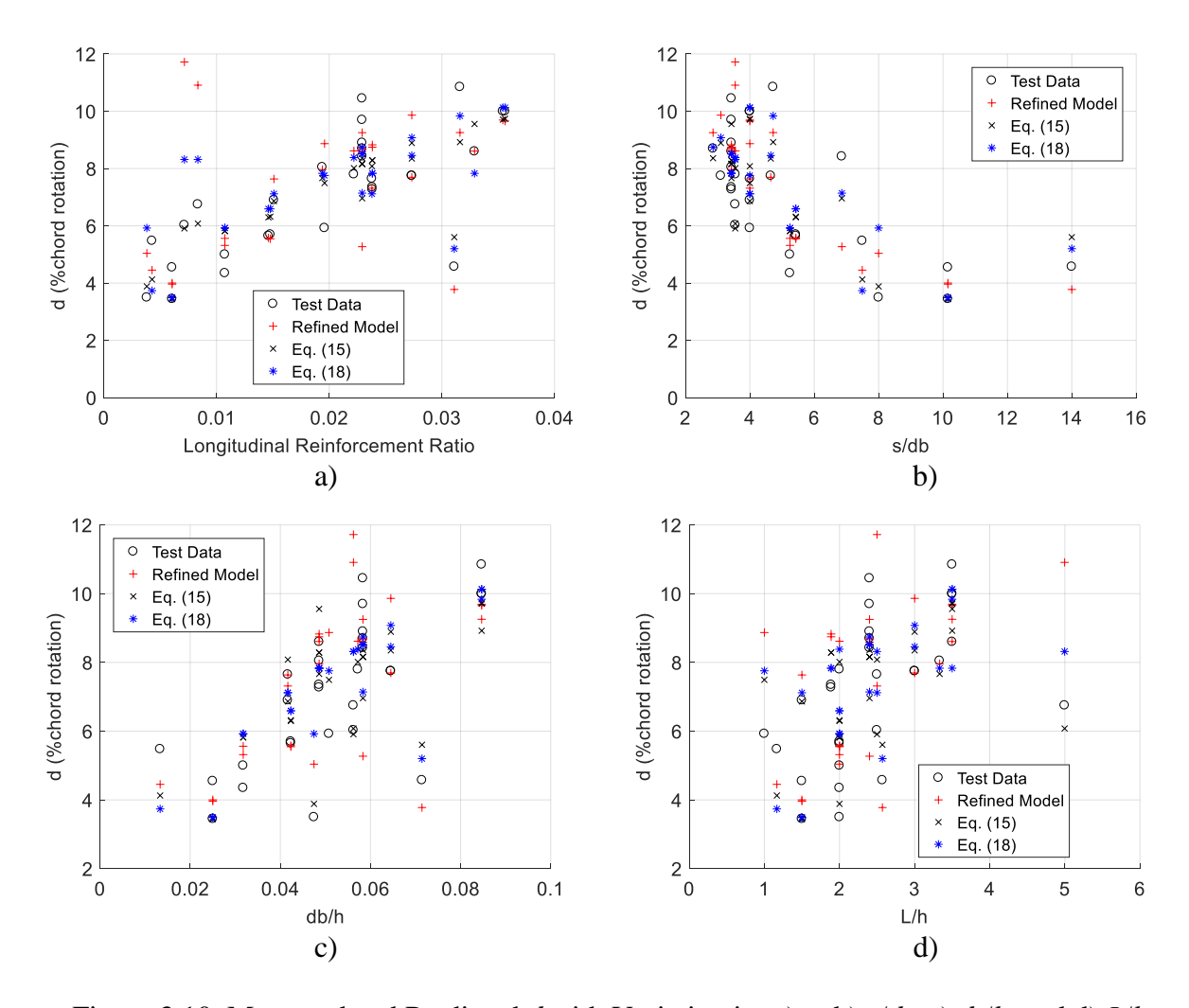


Figure 3.10. Measured and Predicted d with Variation in: a) ρ , b) s/d_b , c) d_b/h , and d) L/h

For ρ , the measured d has lower correlation (r = 0.76) than the predicted d using the empirical model provided by Eq. (3.15) (r = 0.88) and better correlation than the predicted d using the refined model (r = 0.39). For d_b/h , the measured d has lower correlation (r = 0.70) than the predicted d using the empirical model provided by Eq. (3.18) (r = 0.82) and better correlation than the predicted d using the refined model (r = 0.57). For s/d_b , the measured d has lower correlation (r = 0.56) than the predicted d using either the empirical models or the refined model (r = 0.69 for Eq. (3.15), r = 0.74 for Eq. (3.18), and r = 0.76 for the refined model). The dataset used to develop both the empirical model and refined model consisted of beams that reached 20% strength loss and

beams that had Grade 80 and lower reinforcement. For the reasons mentioned in the previous section, Specimens C6 and C8 were also excluded. Considering this dataset, the empirical model given by Eq. (3.18) predicted the deformation capacity to within 2% on average with 18% coefficient of variation versus 0.1% on average with 21% coefficient of variation for the refined model (with $L_p=0.5h$ plus 2.25% chord rotation increase). The empirical model was calibrated to this dataset through regression, while the more refined model was mechanics-based with calibration of a plastic hinge length and adjustment factor. Use of the empirical model as a predictive tool outside of this dataset warrants continued examination. For the six beams in the database with Grade 100 or Grade 120 reinforcement, which were excluded in the regression analysis, the empirical model overpredicted d by 14% with a 12% coefficient of variation, compared to 19% with a 15% coefficient of variation for the refined model. For Specimens C6 and C8, the empirical model overpredicted by 28% and 19%, respectively, and the refined model overpredicted by 49% and 38%, respectively.

3.2.4 Parametric Study

The refined model (with $L_p = 0.5h$ plus the recommended 2.25% chord rotation increase term) and the empirical model provided by Eq. (3.18) were both used to predict the deformation capacity for 24 theoretical beams with variation in ρ , s/d_b , and L/h. Ranges for these parameters were chosen to be representative of the values in the experimental database and from actual buildings. Mohr (2007) reported parameters for 13 diagonally reinforced concrete coupling beams from four buildings. In that study, span-to-depth ratio ranged from 1.1 to 3.2, longitudinal reinforcement ratio ranged from 0.0027 to 0.0217, and transverse reinforcement ratio ranged from 0.0021 to

0.0065. As shown in Figure 3.11 and Table 3.3 for the parametric study, values ranging from 0.004 to 0.024 were used for ρ , values of 2.8, 3.5, and 4.6 were used for s/d_b , values of 0.014 and 0.025 were used for ρ_t , and values of 1.0, 2.0, 3.0, and 4.0 were used for L/h. The beams had full section confinement, and one set of four beams with diagonal confinement were included to match beams with full section confinement at the upper range of ρ .

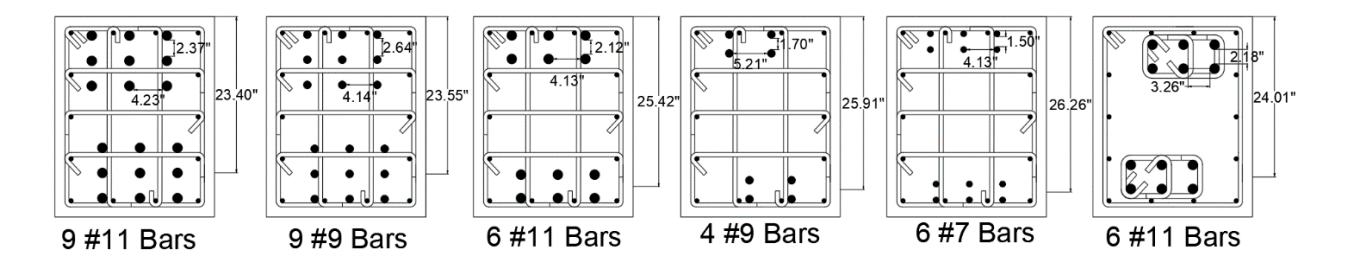


Figure 3.11. Cross-Sectional Drawings for Beams in Parametric Study

Table 3.3. Variation in Parameters for Beams in Parametric Study

Specimen	Confinement	Longitudingal Reinf Ratio ρ	Transverse Reinf Ratio ρ_t	S/d_b	Effective Depth $d_{\mathcal{S}}$ (in)	d_c (in)	b_c (in)	W_ix (in)	W_iy (in)
FSC, (L/h) = 1.0, 6#7 FSC, (L/h) = 2.0, 6#7 FSC, (L/h) = 3.0, 6#7 FSC, (L/h) = 4.0, 6#7		0.004 0.005 0.006 0.006		4.6	26.26			5.75	
FSC, (L/h) = 1.0, 4#9 FSC, (L/h) = 2.0, 4#9 FSC, (L/h) = 3.0, 4#9 FSC, (L/h) = 4.0, 4#9		0.005 0.006 0.006 0.006		3.5	25.91		20.38		
FSC, (L/h) = 1.0, 9#9 FSC, (L/h) = 2.0, 9#9 FSC, (L/h) = 3.0, 9#9 FSC, (L/h) = 4.0, 9#9	F	0.012 0.015 0.015 0.016	0.014		23.55	26.38			5.66
FSC, (L/h) = 1.0, 6#11 FSC, (L/h) = 2.0, 6#11 FSC, (L/h) = 3.0, 6#11 FSC, (L/h) = 4.0, 6#11		0.012 0.014 0.015 0.015			25.42				
FSC, (L/h) = 1.0, 9#11 FSC, (L/h) = 2.0, 9#11 FSC, (L/h) = 3.0, 9#11 FSC, (L/h) = 4.0, 9#11		0.019 0.023 0.024 0.024		2.8	23.40				
DCS, (L/h) = 1.0, 6#11 DCS, (L/h) = 2.0, 6#11 DCS, (L/h) = 3.0, 6#11 DCS, (L/h) = 4.0, 6#11	D	0.013 0.015 0.016 0.016	0.025		24.01	5.75	11.25	3.26	2.18

Drawings of the beam cross-sections at the beam-wall interface are provided in Figure 3.11. The beams in the parametric study were selected to be 24" wide by 30" deep with 1.5" clear cover. All beams used Gr. 60 reinforcement and 6 ksi concrete with No. 5 or No. 6 transverse hoops and ties spaced at 4". Spacing of transverse reinforcement was selected to maintain the s/d_b ratio for beams with equivalent bar size. Beams were designed to be in compliance with, but not significantly exceed, provisions in ACI 318-19. The set of beams using confinement of the diagonal bundle required No. 6 hoops to meet the provision prescribed in ACI 318-19 Section 18.10.7.4 (ii), which specifies that A_{sh} be computed for a value of A_g determined by assuming the concrete cover specified in Section 20.5.1 is provided on all four sides of the bundle. Satisfying this provision resulted in a larger value for ρ_t for beams with confinement of the diagonal bundle than beams with full section confinement. The dimensions of the diagonal bundles were selected to meet the ACI 318-19 prescribed minimum dimensions of $\frac{b_w}{2}$ for width and $\frac{b_w}{5}$ for height and the required spacing between diagonal bars as prescribed in ACI 318-19 Section 25.2.3. The depth and width of the confined section measured center-to-center of the confining hoop, d_c , and b_c , respectively, and the horizontal and vertical clear spacing between longitudinal bars, w_{ix} and w_{iy} , respectively, used in the Mander et al (1988) equation are provided in Table 3.3. For beams with full section confinement, w_{ix} and w_{iy} is the clear spacing between longitudinal bars around the perimeter of the beam, while, for beams with diagonal confinement, it is the clear spacing between diagonal bars within the confined bundle.

The deformation capacity of each beam in the parametric study was determined using the previously described refined model and Eq. (3.18). The resulting predicted deformation capacities are provided in Figure 3.12, and the corresponding sources of deformation are provided in Table

3.4. For the ranges of ρ and s/d_b considered, all beams using diagonal confinement or full section confinement failed due to bar buckling. The proposed model relies on the strain at bar buckling to determine the onset of failure, which is based on s/d_b . Therefore, the model predicted approximately the same level of deformation capacity for beams with full section confinement and diagonal confinement that have equivalent values for ρ and s/d_b , with differences coming from variation in computed neutral axis depth. Sensitivity to L/h in the refined model arises from the change in angle of the diagonal bars and change in plastic hinge length relative to beam length. An increase in angle of inclination of the diagonal bars causes an increase in the predicted horizontal deformations given by Eq. (3.4) and Eq. (3.6). The resulting overall chord rotation from Eq. (3.4) and Eq. (3.6) is also reduced by an increase in length. These trends are reflected by results shown in Table 3.4, in which plastic shear deformation increases as L/h decreases. It is evident from Table 3.4 that an increase in d_b increases the percentage of overall deformation that is attributed to slip and extension. This is due to the increased slip/extension for larger bars in the Alsiwat and Saatcioglu (1992) bond slip model. An increase in plastic deformation with an increase in d_b is also evident from Table 3.4, which can be attributed to the decrease in s/d_b when spacing of transverse reinforcement is held constant and the diagonal bar diameter is increased.

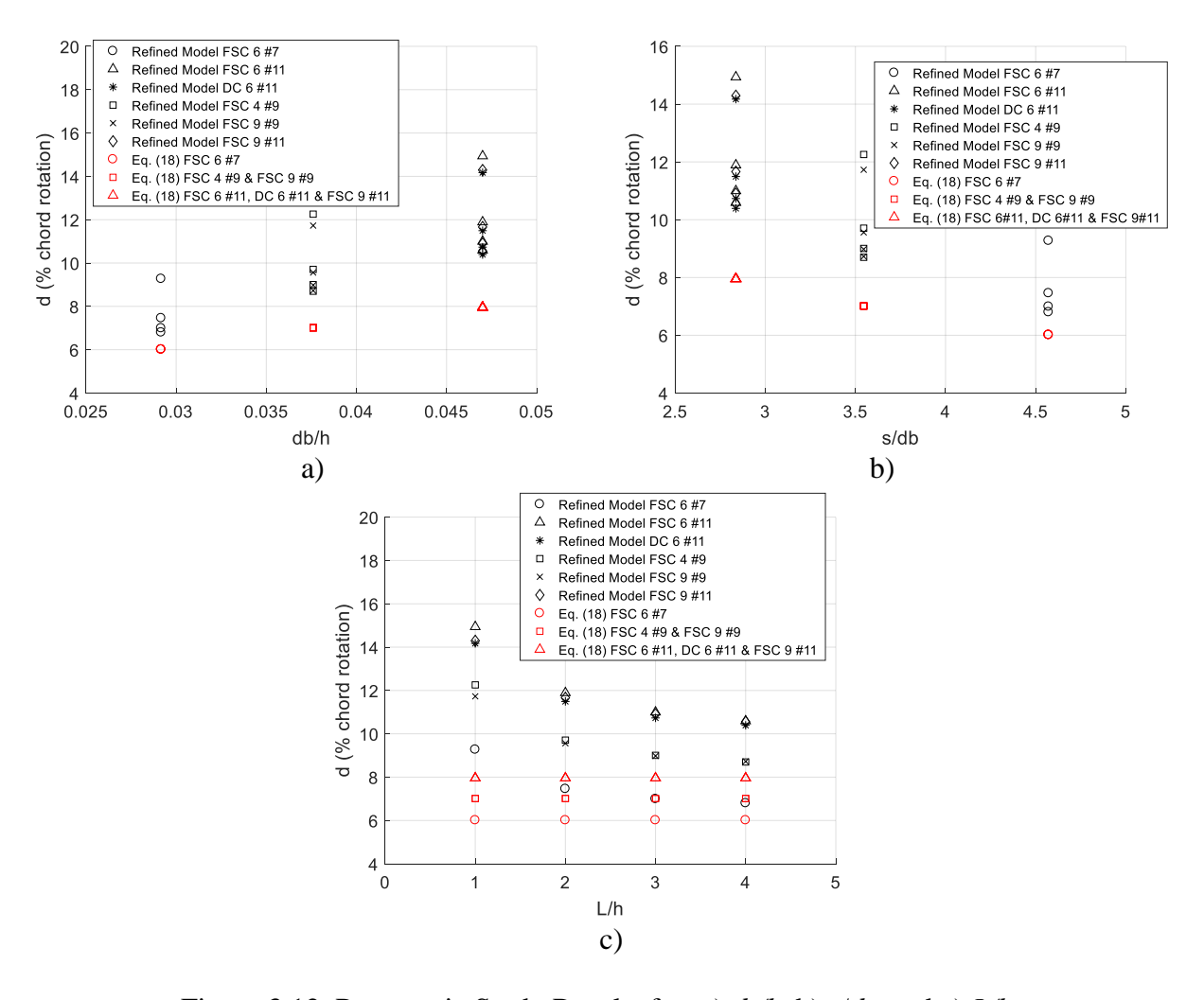


Figure 3.12. Parametric Study Results for: a) d_b/h , b) s/d_b , and c) L/h

Table 3.4. Sources of Deformation at Deformation Capacity for Beams in Parametric Study

	Computed	Elastic	Elastic	Slip/	Slip/Ext	Plastic Hinge	Hinge	Plastic Shear	Shear	Total +2,25%	Eq. (19)	N/A Depth
Specimen	N.A. Depth	Flexure/ Shear	% of Total	Extension	% of Total	Rotation	% of Total		% of Total	10tal +2.25%	Eq. (19)	@ BB
	(in)	(% Chord Rot)	/6 UI TULAI	(% Chord Rot)	/6 OI 10tai	(% Chord Rot)	/0 UI 10tai	(% Chord Rot)	70 OI TOTAL	(% Chord Rot)	% Rotation	(in)
FSC, (L/h) = 1.0, 6#7	4.04	0.1	2.0	2.6	36.5	1.2	16.6	3.2	45.0	9.3	5.4	3.56
FSC, (L/h) = 2.0, 6#7	4.08	0.2	3.0	2.0	37.9	2.1	40.9	1.0	18.4	7.5	5.4	4.21
FSC, (L/h) = 3.0, 6#7	4.09	0.2	3.4	1.7	35.2	2.5	52.2	0.4	9.4	7.0	5.4	4.32
FSC, (L/h) = 4.0, 6#7	4.10	0.2	3.5	1.5	33.0	2.6	58.1	0.3	5.6	6.8	5.4	4.38
FSC, (L/h) = 1.0, 6#11	4.89	0.3	2.7	6.0	47.0	1.8	14.2	4.6	36.3	14.9	7.5	5.55
FSC, (L/h) = 2.0, 6#11	4.97	0.4	3.9	4.6	47.9	3.3	33.9	1.4	14.4	11.9	7.5	5.65
FSC, (L/h) = 3.0, 6#11	4.99	0.4	4.4	3.9	44.9	3.8	43.5	0.6	7.4	11.0	7.5	5.67
FSC, (L/h) = 4.0, 6#11	4.99	0.4	4.6	3.5	42.4	4.1	48.7	0.4	4.4	10.6	7.5	5.67
DCS, (L/h) = 1.0, 6#11	6.30	0.3	2.6	5.6	47.0	1.8	15.5	4.2	34.9	14.2	7.5	2.74
DCS, $(L/h) = 2.0, 6#11$	6.40	0.4	3.8	4.4	47.2	3.3	35.7	1.2	13.4	11.5	7.5	2.78
DCS, (L/h) = 3.0, 6#11	6.42	0.4	4.3	3.7	44.1	3.8	45.0	0.6	6.7	10.7	7.5	2.80
DCS, $(L/h) = 4.0, 6#11$	6.43	0.4	4.4	3.4	41.7	4.1	50.0	0.3	4.0	10.4	7.5	2.83
FSC, (L/h) = 1.0, 4#9	4.16	0.2	1.5	4.2	42.3	1.5	15.4	4.1	40.9	12.3	6.5	3.9
FSC, (L/h) = 2.0, 4#9	4.22	0.2	2.3	3.3	43.7	2.8	37.5	1.2	16.6	9.7	6.5	4.49
FSC, (L/h) = 3.0, 4#9	4.24	0.2	2.6	2.8	40.9	3.2	48.1	0.6	8.5	9.0	6.5	4.63
FSC, (L/h) = 4.0, 4#9	4.24	0.2	2.7	2.5	38.5	3.5	53.8	0.3	5.1	8.7	6.5	4.7
FSC, (L/h) = 1.0, 9#9	6.31	0.3	3.1	4.0	41.8	1.5	16.2	3.7	39.0	11.7	6.5	5.52
FSC, (L/h) = 2.0, 9#9	6.49	0.3	4.6	3.1	42.3	2.8	38.1	1.1	15.2	9.6	6.5	5.63
FSC, (L/h) = 3.0, 9#9	6.53	0.3	5.0	2.6	39.3	3.2	48.1	0.5	7.7	9.0	6.5	5.65
FSC, (L/h) = 4.0, 9#9	6.55	0.3	5.2	2.4	36.9	3.5	53.4	0.3	4.6	8.7	6.5	5.66
FSC, (L/h) = 1.0, 9#11	6.78	0.4	3.7	5.6	46.6	1.8	14.9	4.2	34.9	14.3	7.5	5.76
FSC, (L/h) = 2.0, 9#11	6.92	0.5	5.3	4.4	46.8	3.3	34.7	1.3	13.4	11.7	7.5	5.83
FSC, (L/h) = 3.0, 9#11	6.95	0.5	5.8	3.8	43.7	3.8	43.8	0.6	6.8	10.9	7.5	5.85
FSC, (L/h) = 4.0, 9#11	6.96	0.5	6.1	3.4	41.2	4.0	48.8	0.3	4.0	10.6	7.5	5.85

3.3 Effective Stiffness

To compare the recommended effective stiffness values given by ASCE/SEI 41-17 and PEER TBI to the measured stiffness values, an equivalent EI_{eff} that accounts for both shear rigidity, AG, and flexural rigidity, EI, is:

$$(EI_{eff}) = \frac{EI}{1 + (EI)\frac{12}{L^2AG}}$$
(3.20)

Eq. (3.20) was used to compute stiffness values for each beam in the database using the ASCE/SEI 41-17 recommended flexural rigidity of $0.3E_cI_g$ and shear rigidity of $0.4E_cA_W$, as well as the ACI 318-19 Section A.8.4 and PEER TBI (2017) recommended flexural rigidity of $0.07 \left(\frac{l}{h}\right) E_cI_g$ and shear rigidity of $0.4E_cA_g$. The comparison of these results to the measured stiffness values are shown in Figure 3.13 and are provided in Table 3.1 as k. Two outliers, Specimens CB-2A and CB-

2B, which exhibited considerably low stiffness during testing, were excluded from the analysis and statistical results. Normalizing the computed effective stiffness values by $\%E_cI_g$, and taking the difference between predicted and measured values, the ASCE/SEI 41-17 method predicts stiffness that is on average 15.4% of E_cI_g larger than the measured value with a coefficient of variation of 10%. The PEER TBI method predicts stiffness that in on average 5.8% of E_cI_g larger than the measured value with a coefficient of variation of 36%.

If the term $0.07 \left(\frac{l}{h}\right) E_c I_g$ in the ACI 318-19 Section A.8.4 and PEER TBI (2017) recommended flexural rigidity is changed to $0.05 \left(\frac{l}{h}\right) E_c I_g$, and the shear rigidity is maintained as $0.4 E_c A_g$, the predicted stiffness is, on average, 1.3% of $E_c I_g$ larger than measured values with a coefficient of variation of 35%. Although changing the coefficient from 0.07 to 0.05 provides a better fit to measured test data, it is noted in the PEER TBI (2017) Section 4.6.3 Commentary that the recommended values were increased relative to test data to account for test specimen scale and presence of the floor diaphragm.

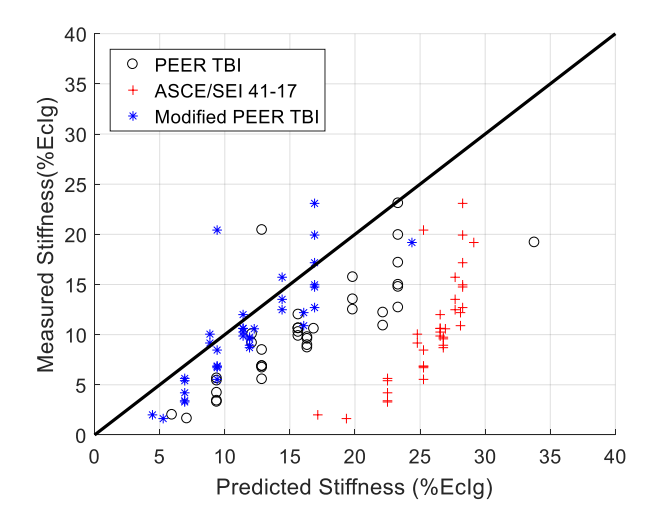


Figure 3.13. Comparison of Predicted to Measured Stiffness

3.4 Strength

For each test in the database, the ratio of measured strength to ACI 318-19 nominal strength is provided in Figure 3.14a. Nominal strength was taken as the smaller of the nominal shear strength, V_n , and the shear at nominal moment strength, $V@M_n$. V_n was based on the nominal shear strength equation in ACI 318-19 Section 18.10.7.4, which is:

$$V_n = 2A_{vd}f_y\sin(\alpha) \le 10\sqrt{f_c'}A_{cw}$$
(3.21)

where A_{vd} is the total area of reinforcement in each group of diagonal bars, A_{cw} is the area of the concrete resisting shear in the coupling beam, α is the angle of inclination of the diagonal bars, and f_y is the yield stress of the diagonal bars. M_n was computed by plain strain fiber analysis of the cross section using the stress-strain relationship developed from Hognestad (1955) with 0.002 used as the strain at peak stress.

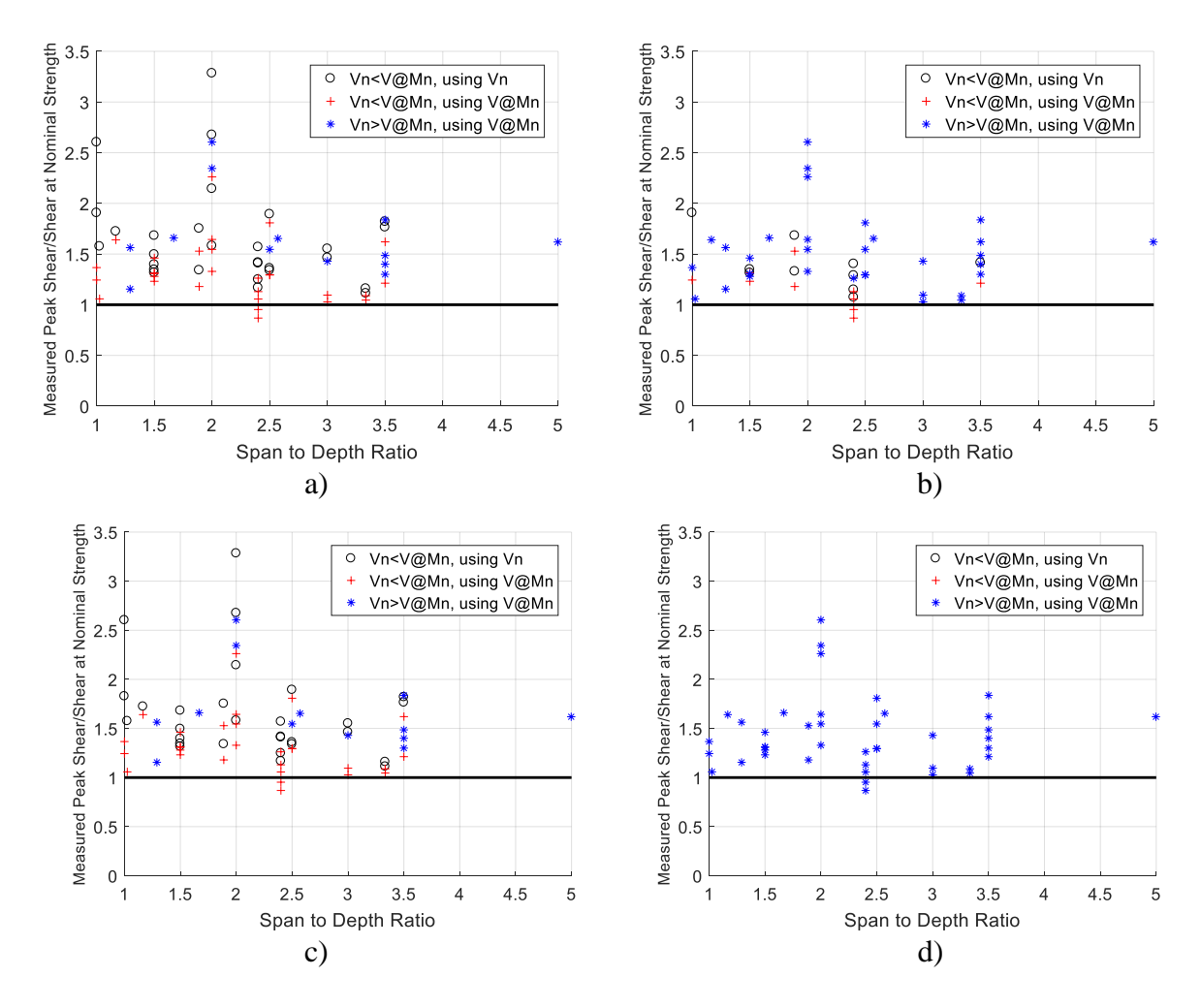


Figure 3.14. Ratio of Measured Maximum Shear Force to Nominal Strength for a) V_n from ACI 318-19, b) Proposed V_n from Eq. (3.22) c) V_n from ACI 318-19 Without $10\sqrt{f'c}b_wd$ Limit, and d) Proposed V_n from Eq. (3.22) Without $10\sqrt{f'c}b_wd$ Limit

In Figure 3.14a, indication is provided as to whether the nominal strength was based on V_n or $V@M_n$. In cases where V_n controlled, the ratio of measured strength to nominal strength is shown for both V_n and $V@M_n$. The equation for V_n in ACI 318-19 does not include the shear strength from concrete and transverse reinforcement. A new equation for V_n of diagonally reinforced coupling beams that considers the shear strength from concrete and transverse reinforcement, in addition to the shear strength from the horizontal component of the diagonal reinforcement, is:

$$V_n = 2A_{vd}f_y \sin(\alpha) + \left((max\left(2, 8(\rho)^{\frac{1}{3}}\right)) * \sqrt{f_c'} + \frac{N_u}{6A_a} \right) * bd + \frac{A_v f_{yt} d_s}{s} \le 10\sqrt{f_c'} A_{cw}$$
 (3.22)

where ρ is the longitudinal reinforcement ratio of tension reinforcement, b is the width, d_s is the depth to the outermost longitudinal tension reinforcement, N_u is the axial force normal to the cross section, A_g is the gross area of the concrete section, A_v is the area of transverse reinforcement, f_{yt} is the yield strength of transverse reinforcement, and s is the spacing of transverse reinforcement. Transverse reinforcement contributing to A_v enclosed the outermost diagonal reinforcement, such that confinement of individual diagonal bar bundles was not counted toward A_v . A comparison of predicted strength using Eq. (3.22) to measured test data is shown in Figure 3.14b.

Using Eq. (3.21) for the 42 beams in the experimental database, 29 beams were controlled by V_n and 13 were controlled by $V@M_n$. When controlled by V_n , the average ratio of measured peak load to nominal strength was 1.66 with a 0.29 coefficient of variation. When controlled by $V@M_n$, the average ratio of measured peak load to nominal strength was 1.66 with a 0.23 coefficient of variation. Using Eq. (3.22), 10 beams were controlled by V_n and 32 were controlled by $V@M_n$. When controlled by V_n , the average ratio of measured peak load to nominal strength was 1.39 with a 0.17 coefficient of variation. When controlled by $V@M_n$, the average ratio of measured peak load to nominal strength was 1.50 with a 0.24 coefficient of variation. Using Eq. (3.21) and Eq. (3.22), measured peak load exceeded nominal strength for all beams in the database. Overall, the use of Eq. (3.22) led to significant improvement in the underprediction of nominal shear strength and is recommended for use over Eq. (3.21).

Diagonal compression failure, which is reflected by the $10\sqrt{f'c}A_{cw}$ limit in Eq. (3.21) and Eq. (3.22), was not typically observed. For 28 of 42 beams in the database, the measured peak load exceeded $10\sqrt{f'c}A_{cw}$, as shown in Figure 3.15. An attempt was made to identify the failure mechanism using the reported beam behavior during testing and damage photos. No beams in the database were determined to have sustained damage that was clearly indicative of diagonal compression failure prior to buckling of diagonal reinforcement, which was the reported failure for the majority of the beams. Additionally, all beams were able to maintain load-carrying capacity for several cycles after the peak load was reached, which is inconsistent with shear failure from diagonal crushing. Excluding the $10\sqrt{f'c}A_{cw}$ limit led to minimal change for Eq. (3.21) and improved the prediction using Eq. (3.22), as shown in Figure 3.14c and 3.14d. This change in Eq. (3.22) caused all 10 beams with Vn<V@Mn to change to Vn>V@Mn, and the ratio of measured peak load to nominal strength for the 10 beams and the full dataset changed from an average of 1.39 and 1.47, respectively, with a coefficient of variation of 0.17 and 0.23 respectively, to an average of 1.17 and 1.42, respectively, with a coefficient of variation of 0.15 and 0.25, respectively. This change in Eq. (3.22) caused two data points, which were Specimens CB24F-PT and CB24F-(1/2)PT from Naish et al (2008), to shift from being underpredicted with ratio of measured peak load to nominal strength of 1.40 and 1.29, respectively, to being overpredicted with values of 0.95 and 0.87, respectively. For these beams, which both had pretensioned tendons with $A_{ps}f_{se} < 0.4(A_{ps}f_{pu} + A_sf_y)$, the axial load from pre-stressing was included in Eq. (3.22). Alternatively, if using ACI 318-19 Section 22.5.6 to compute V_c for prestressed members, the ratio of peak measured load to predicted strength changed to 0.93 for Speciment CB24F-(1/2)PT and was unchanged for Specimen CB24F-PT due to Vn>V@Mn. Both Specimens CB24F-PT and CB24F-(1/2)PT were reported to fail from buckling of diagonal reinforcement. Due to the reduction in the extent of underprediction and the lack of diagonal compression failure observed in tests, it is recommended to exclude the $10\sqrt{f'c}A_{cw}$ limit in the computation of V_n .

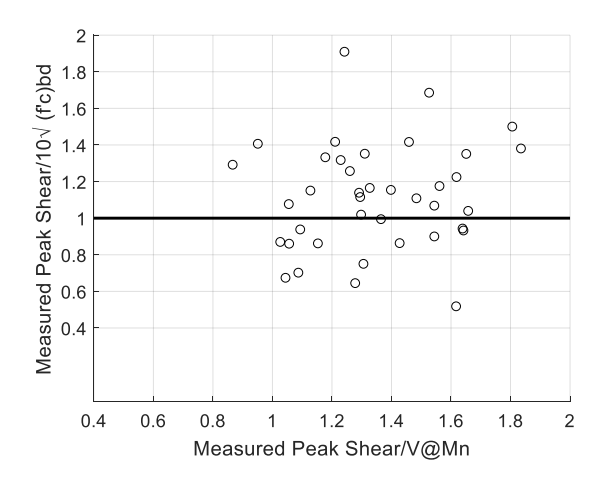


Figure 3.15. Comparison of Peak Measured Shear Demand to $10\sqrt{f'c}b_wd$ Limit

4. EXPERIMENTAL PROGRAM

The simplified model and empirical equation described in the previous section were developed to estimate the deformation capacity of diagonally reinforced concrete coupling beams. The model was not intended to predict axial elongation and capture the resulting influence of axial restraint on coupling beam deformation capacity. In the majority of previous tests, the coupling beams were not subjected to axial restraint. In an effort to better characterize the influence of axial restraint on reinforced concrete coupling beam behavior, including deformation capacity, an experimental program was conducted on coupling beams subjected to axial restraint.

4.1 Beam Details

Seven one-half-scale reinforced concrete coupling beams were constructed and tested at the Simpson Strong-Tie Experimental Testing Laboratory (SST Lab), which is part of the Composite Materials and Engineering Center (CMEC) at Washington State University (WSU). A test matrix is provided in Table 4.1 and drawings are provided in Figure 4.1 through Figure 4.4. The seven tests included three nominally identical pairs, of which one pair was conventionally reinforced and two pairs were diagonally reinforced. The two beams in each pair were tested at a different level of constant stiffness axial restraint, indicated by k_{axial} in Table 4.1. For the diagonally reinforced beams, additional test variables included longitudinal reinforcement ratio (ρ), bar diameter of longitudinal or diagonal reinforcement, and span-to-depth ratio (aspect ratio), with the values for these variables provided in Table 4.1. Beam names are shown in Table 4.1, and test variables are reflected in the naming convention. The first letter indicates the reinforcement configuration, with

"C" for conventionally reinforced and "D" for diagonally reinforced. The numerical value in parentheses indicates the size of the primary reinforcement used in each beam. The second numerical value indicates the span-to-depth ratio of the beam. The last numerical value indicates the level of applied axial compressive stiffness normalized to $A_g f'_c$.

Table 4.1. Test Matrix

Beam Name	Aspect	α	Configuration	Primary	Long.	k _{axial}	ACI	M_n	$V_@M_n$	A_{shx}	A_{shy}
	Ratio			Rein.	Reinf.	(k/in)	Shear	(k*in)	(k)	(in^2)	(in^2)
					Ratio		Strength				
					(ρ)		V _n (kip)				
C(#5)-3.0-0.69		0	Conventional	4 #5	0.75%	500	74.9	934.9	41.6	0.307	0.153
C(#5)-3.0-0.35			Conventional	4 #5	0.75%	250	74.9	934.9	41.6	0.307	0.153
D(#4)-3.0-0.69	3.0		Diagonal	6 #4	0.78%	500	31.1	834.3	37.1	0.383	0.537
D(#4)-3.0-1.38		12.7	Diagonal	6 #4	0.78%	1000	31.1	834.3	37.1	0.383	0.537
D(#6)-3.0-0.69			Diagonal	6 #6	1.74%	500	69.9	1607.6	71.5	0.383	0.537
D(#6)-3.0-1.38			Diagonal	6 #6	1.74%	1000	69.9	1607.6	71.5	0.383	0.537
D(#6)-1.5-0.69	1.5	24.5	Diagonal	6 #6	1.63%	500	131.9	1515.1	134.7	0.383	0.537

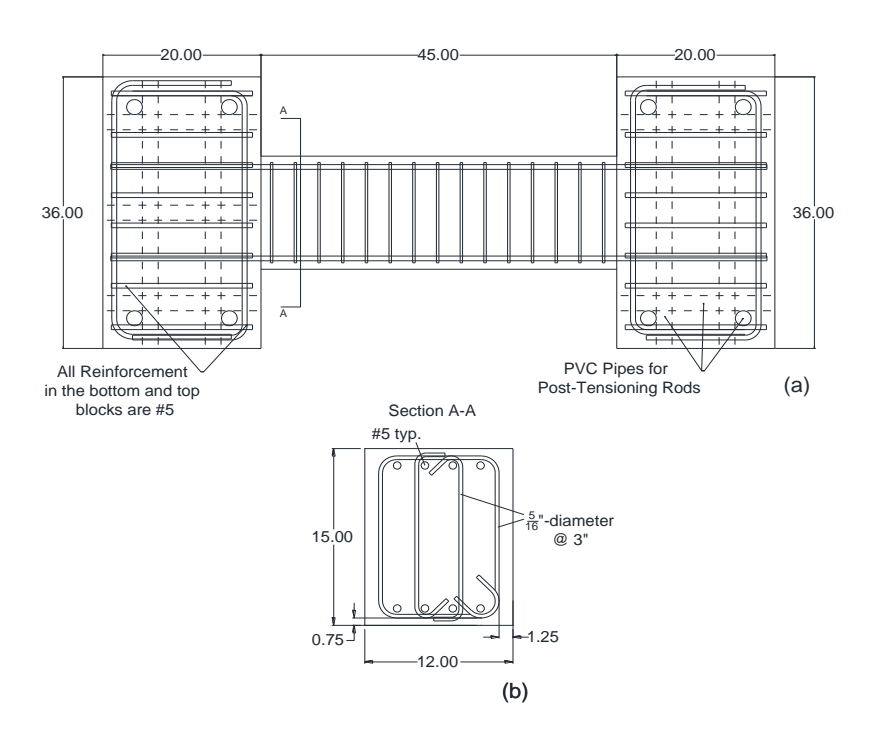


Figure 4.1. C(#5)-3.0-0.69 and C(#5)-3.0-1.38: a) Elevation View and b) Beam Cross Section

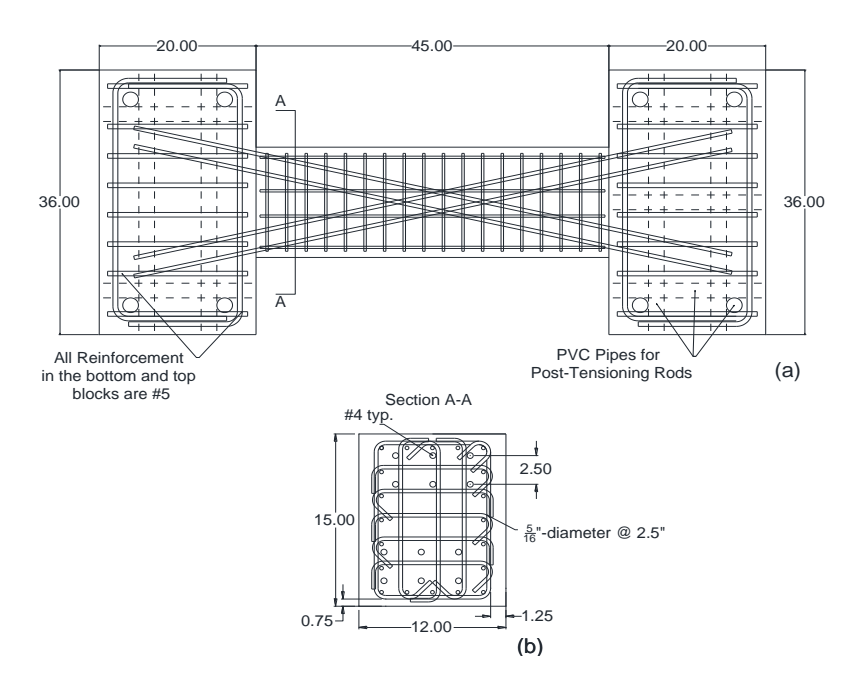


Figure 4.2. D(#4)-3.0-0.69 and D(#4)-3.0-0.69: a) Elevation View and b) Beam Cross Section

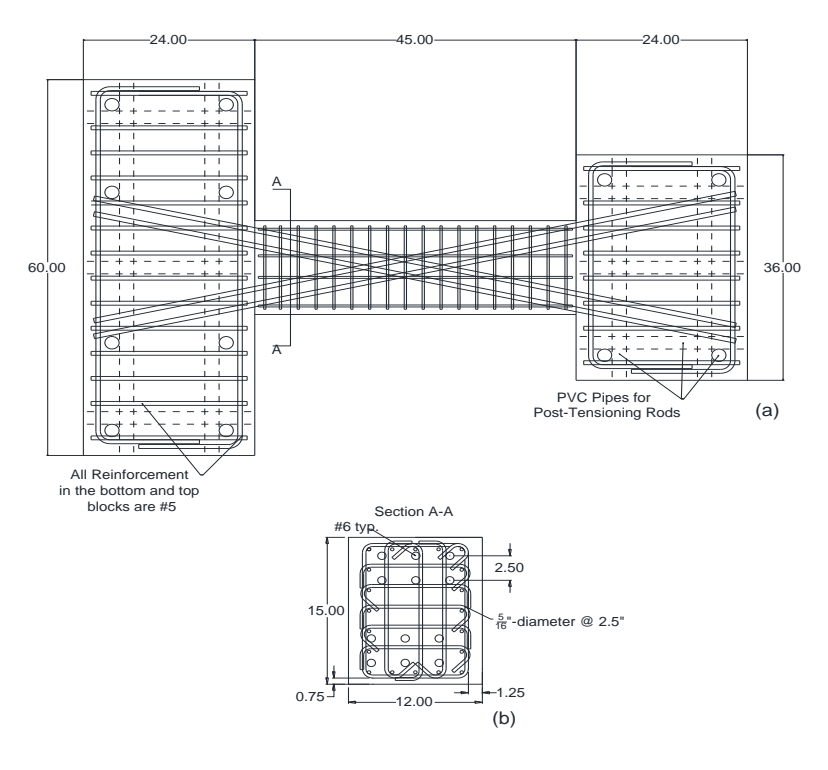


Figure 4.3. D(#6)-3.0-0.69 and D(#6)-3.0-0.69: a) Elevation View and b) Beam Cross Section

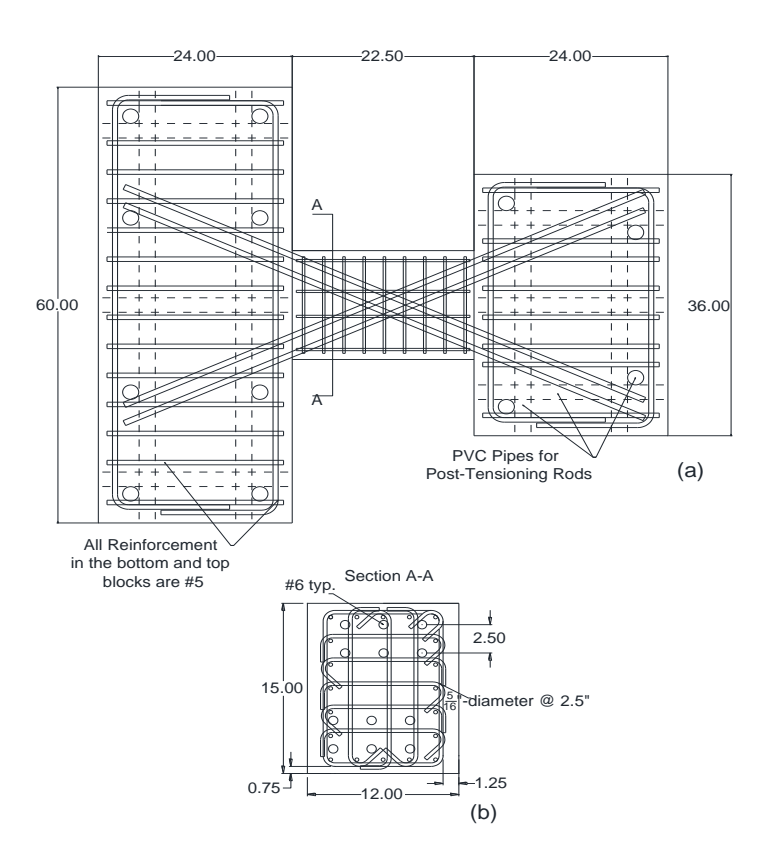


Figure 4.4. D(#4)-1.5-0.69: a) Elevation View and b) Beam Cross Section

The one-half-scale test beams with 12" by 15" cross-section were based on full-scale beams with 24"x30" cross-section. For the full-scale beams, primary reinforcement was assumed to range from #8 to #11, with six bars in each diagonal bar bundle. The diagonal reinforcement in the test beams was 6#6 or 6#4 in each diagonal bar bundle. The resulting longitudinal reinforcement ratios were 0.78%, 1.74%, and 1.63%, which were deemed to reasonably cover the range of 0.27% to 2.17% reported by Mohr (2007) for a survey of sample buildings. The conventionally reinforced beams had 4#5 longitudinal reinforcement top and bottom. The resulting longitudinal reinforcement ratio of 0.75% fell within the range of 0.46% to 1.16% reported by Mohr (2007) for conventionally reinforced coupling beams. The span-to-depth ratio was 3.0 for the conventionally reinforced beams and ranged from 1.5 to 3.0 for the diagonally reinforced beams. These values fell within the ranges reported by Mohr (2007), which were 2.7-3.4 for conventionally reinforced and 1.1-3.2

for diagonally reinforced. Transverse reinforcement, as well as longitudinal reinforcement in diagonally reinforced beams, was 5/16" diameter A36 smooth bar. The 5/16" bar size was selected to represent #5 transverse reinforcement at full-scale.

For the purpose of designing the transverse reinforcement, the beams were designed based on 4 ksi concrete compressive strength, 60 ksi yield stress for diagonal or longitudinal reinforcement, and 54 ksi yield stress for transverse reinforcement. 54 ksi is the expected yield strength of A36 reinforcement per PEER TBI (2017). Although the use of expected strength for design is atypical, it was used here due to the large difference in expected versus specified strength for A36 relative to A615.

For the two conventionally reinforced beams, the design of the transverse reinforcement followed ACI 318-19. Capacity design was used to provide a factored nominal shear strength, φV_n , that exceeded the design shear force, V_e , determined in accordance with ACI 318-19 Section 18.6.5 as:

$$V_e = \frac{M_{pr1} + M_{pr2}}{l_n} \pm \frac{w_u * l_n}{2} \tag{4.1}$$

where M_{pr} is the probable flexural strength, w_u is the factored gravity and vertical earthquake loads along the beam span, and l_n is the span length of the beam. Gravity load was not applied to the test beams, such that w_u was taken as zero. M_{pr} was calculated for a steel tensile stress of $1.25f_y$ and an extreme fiber compressive strain of 0.003 in accordance with ACI 318-19 Section 18.6.5. Although the beams were tested with axial restraint applied, axial load was not included in the computation of M_{pr} for shear design purposes, as this is not uncommon in current design practice.

 M_{pr} was computed to be 1157.5 kip-in, resulting in a shear demand of 51.4 kip computed using Eq. (4.1). For the configuration of shear reinforcement provided, φV_n was computed to be 56.2 kips, with V_s computed using ACI 318-19 Section 22.5.8.5 and V_c taken as zero in accordance with ACI 318-19 Section 18.7.6.2.1.

For diagonally reinforced beams, ACI 318-19 has the option to provide transverse reinforcement for each diagonal bar group (Section 18.10.7.4(c)) or for the entire cross-section (Section 18.10.7.4(d)). The latter was used for the test beams. ACI 18.10.7.4(d) limits the spacing of transverse reinforcement to 6" or $6d_b$ in the longitudinal direction and 8" horizontally and vertically within the plane of the cross-section. At one-half scale for the test beams, this limited the spacing to 3" longitudinally and 4" within the plane of the cross-section. ACI 18.10.7.4(d) also requires that the total cross-sectional area of transverse reinforcement, A_{sh} , in each orthogonal direction meet or exceed the following:

$$A_{sh} = 0.09sb_c \frac{f'_c}{f_{vt}} \tag{4.2}$$

$$A_{sh} = 0.3sb_c(\frac{A_g}{A_{ch}} - 1)\frac{f'_c}{f_{vt}}$$
(4.3)

where s is the center to center spacing of the transverse reinforcement in the longitudinal direction, b_c is the cross-sectional dimension of member core measured to the outside edges of the transverse reinforcement, f'_c is the specified compressive strength of concrete, f_{yt} is the specified yield strength of transverse reinforcement, A_g is the gross area of concrete section, and A_{ch} is the cross-sectional area of a member measured to the outside edges of transverse reinforcement. Based on these requirements, s was selected as 2.5" with seven and five legs of transverse reinforcement

over the height and width of the cross-section, respectively, at each spacing interval. The resulting spacing between the crossties in each orthogonal direction within the cross-section was 2.2".

As shown in Figure 4.1 through Figure 4.4, each test beam included two concrete blocks at the beam ends. The blocks enabled anchorage of the beam specimen to the laboratory strong floor and to the loading beam. PVC pipes were installed in the top and bottom block in all directions to create voids for anchor rods. The provided embedment length of the diagonal reinforcement into the blocks was determined using $1.25f_y$ in accordance with ACI 318-19 Section 18.10.7. The longitudinal reinforcement in the diagonally reinforced beams was not embedded into the blocks, consistent with the recommendation of Barbachyn et al (2012), rather than embedded a short distance as shown in ACI 318-19 Fig. R18.10.7.b.

The calculated nominal shear strength, V_n , and shear at nominal moment, $V@M_n$ are included in Table 4.1 for the test beams, in order to provide an indication as to whether the beams were expected to yield in shear, flexure, or both. For the diagonally reinforced beams, M_n was calculated using the horizontal projection of the diagonal bars and neglecting the longitudinal reinforcement, which was not embedded into the concrete blocks. Because gravity load was not applied to the coupling beams during testing, $V@M_n$ was computed based on a fixed-fixed beam, such that $V@M_n = 2M_n/L$, where L is the length of the beam. The nominal shear capacity for the diagonally reinforced beams was calculated using Eq. (3.23) in accordance with ACI 318-19 Section 18.10.7.4.

4.2 Construction

Construction began with the assembly of formwork. Reinforcement was then cut and bent. Strain gauges were installed on reinforcement as shown in Figure 4.5. More details on the locations of strain gauges are provided in Section 4.5. Reinforcement was tied into cages, as shown in Figure 4.6 through Figure 4.10. The cages were placed in formwork with spacers used to set the concrete clear cover to the edge of reinforcement. PVC pipes were installed in the bottom and top concrete blocks. Holes were drilled into formwork to allow the installation of ¼" diameter threaded rods, which passed through the beams. The threaded rods were used to facilitate the attachment of instrumentation, with more details provided in Section 4.5. The test beams were oriented horizontally during concrete placement, as shown in Figure 4.11, with a free surface over the width and length of the beam. This simulated the orientation used during field construction of coupling beams. Concrete was placed in two pours, with the first pour to the surface of the beam. A cold joint was located in the footing block and top block at this height, such that the second pour did not include any concrete in the beam. After concrete was allowed to set, formwork was removed to complete construction.



Figure 4.5. Strain Gauge Installation



Figure 4.6. Reinforcement Cages for Top and Bottom Blocks



Figure 4.7. Reinforcement Cages for C(#5)-3.0-0.69 and C(#5)-3.0-0.35



Figure 4.8. Reinforcement Cage for D(#4)-3.0-0.69 or D(#4)-3.0-1.38



Figure 4.9. Reinforcement Cage for D(#6)-3.0-0.69 or D(#6)-3.0-1.38



Figure 4.10. Reinforcement Cage for D(#6)-1.5-0.69



Figure 4.11. Reinforcement Cages in Formwork Prior to Pouring Concrete to Top of Beams

4.3 Material Properties

Material testing was conducted to obtained measured material properties. 6" by 12" concrete cylinders were cast during placement of concrete to the top of the beams. After casting C(#5)-3.0-0.69, C(#5)-3.0-0.35, D(#4)-3.0-0.69, and D(#4)-3.0-1.38, water was added to the concrete mix prior to casting D(#6)-3.0-0.69, D(#6)-3.0-1.38, and D(#6)-1.5-0.69. Separate cylinders were cast for the concrete after water was added. Within a week of testing each of C(#5)-3.0-0.69, C(#5)-3.0-0.35, D(#4)-3.0-0.69, D(#4)-3.0-1.38, three cylinder compression tests were conducted, with the results provided in Table 4.2. Minimal variation in the average compressive strengths are evident over the time elapsed for these four tests, such that an overall average value of 3.45 ksi was used as the measured concrete strength for subsequent calculations on these four beams. After testing these four beams, testing of D(#6)-3.0-0.69, D(#6)-3.0-1.38, and D(#6)-1.5-0.69 progressed in this sequence. After completion of testing of D(#6)-1.5-0.69, three cylinder compression tests were conducted. The average value of 3.05 ksi was used as the measured concrete strength for subsequent calculations for these three beams.

Table 4.2. Measured Concrete Compressive Strength from 6"x12" Cylinder Tests

	Concrete	Measured Compressive Strength (ksi)							
	Age (days)	Test 1	Test 2	Test 3	Average				
C(#5)-3.0-0.69	217	3.76	3.48	3.00	3.42				
C(#5)-3.0-0.35	228	3.50	3.69	3.28	3.49				
D(#4)-3.0-0.69	247	3.44	3.29	3.61	3.45				
D(#4)-3.0-1.38	259	3.38	3.64	3.30	3.44				
D(#6)-1.5-0.69	355	2.95	3.13	3.08	3.05				

Reinforcement samples obtained from the same batches of reinforcement used in the beams were tested in tension to obtain the measured stress-strain responses shown in Figure 4.12. The resulting yield and ultimate tensile strength obtained from the stress-strain responses are provided in Table 4.3.

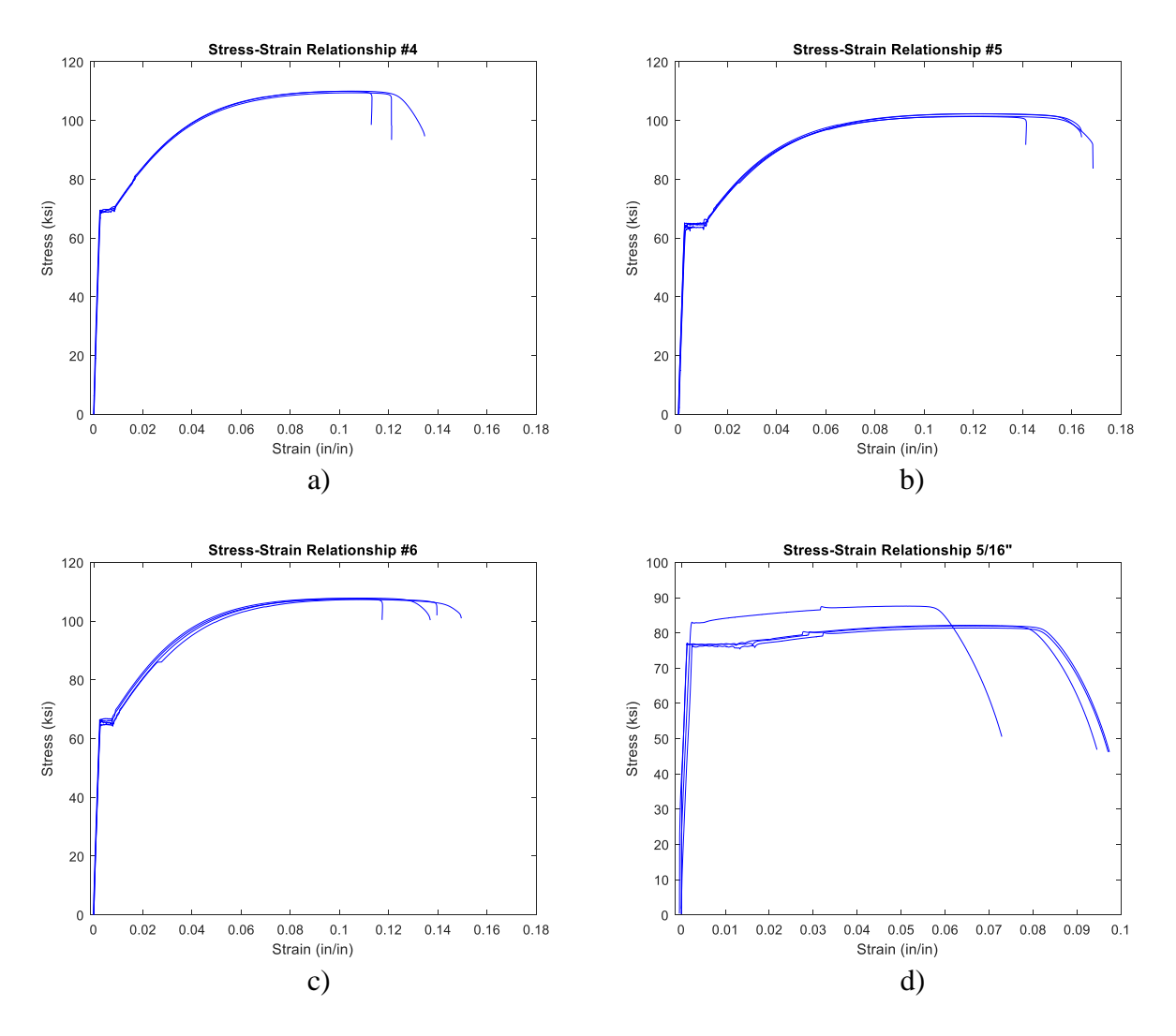


Figure 4.12. Stress-Strain for: a) #4 Reinforcement, b) #5 Reinforcement, c) #6 Reinforcement, and d) 5/16"-Diameter Reinforcement

Table 4.3. Measured Yield and Ultimate Tensile Strength of Reinforcement

Bar	7	ield ter	nsile str	ength (k	csi)	Ultimate tensile strength (ksi)						
Size	Test 1	Test 2	Test 3	Test 4	Average	Test 1	Test 2	Test 3	Test 4	Average		
#5	62.8	64.2	65.1	63.8	64.0	101.5	101.4	102.3	102.3	101.9		
#4	69.5	69.0	69.5	-	69.3	110.0	109.5	110.0	-	109.8		
#6	66.0	66.1	64.7	66.5	65.8	107.7	107.4	107.8	107.4	107.6		
5/16"	77.1	77.1	83.0	76.6	78.4	82.2	82.0	81.4	87.6	83.3		

4.4 Test Set-Up

Drawings and a photo of the test setup are shown in Figure 4.13 through Figure 4.15. The beams were tested in the vertical orientation. Three actuators were used during testing. A laterally oriented actuator with +/- 10" stroke and 200-kip capacity was aligned with the beam midspan and used to apply reversed cyclic loading. Two vertically oriented actuators with +/- 36" stroke and 300-kip capacity were used to apply axial restraint while also applying any necessary moment to maintain zero rotation at the bottom of the steel loading beam.

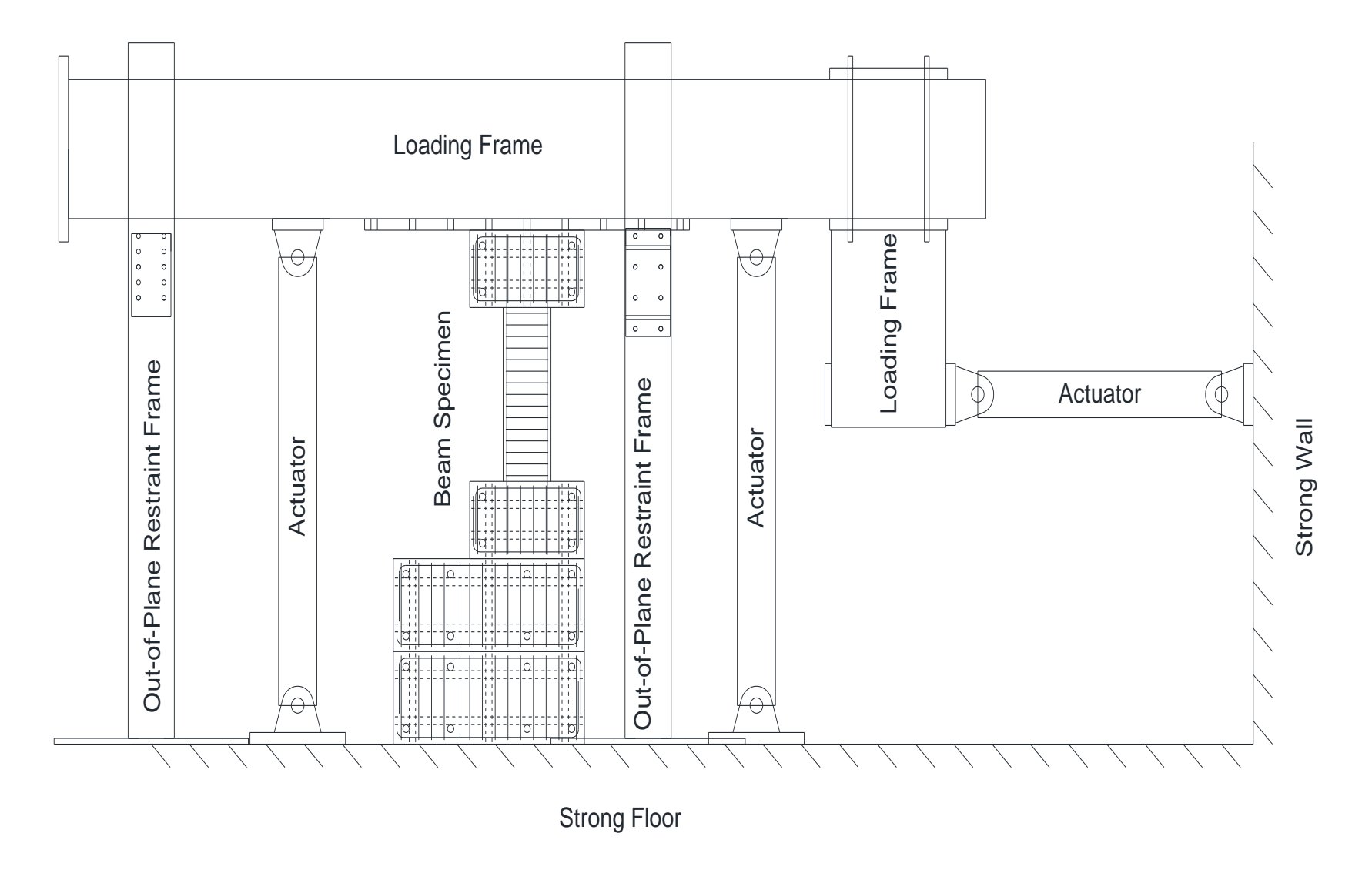


Figure 4.13. 2D Drawing of Test Set Up

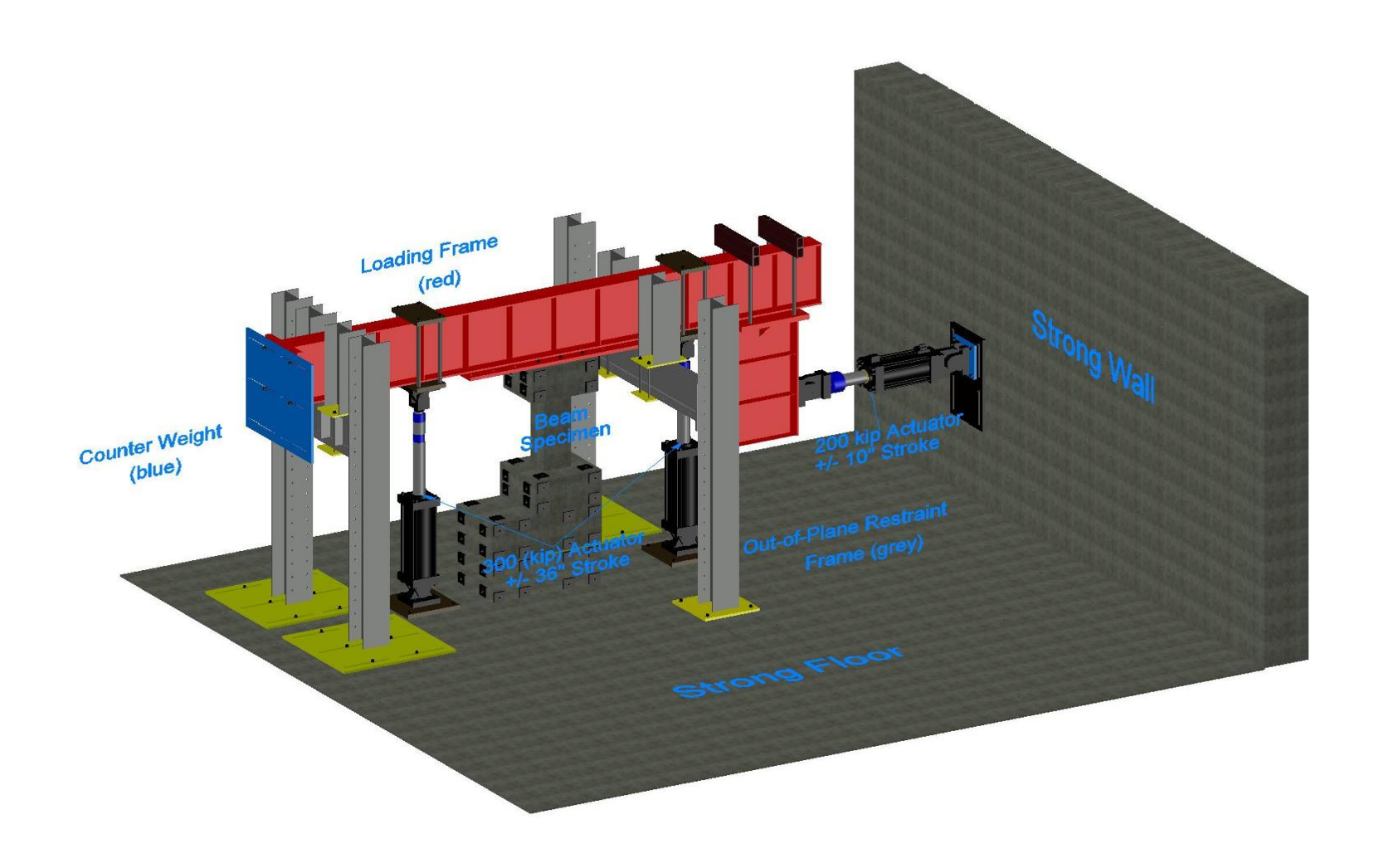


Figure 4.14. 3D Rendering of Test Set-Up

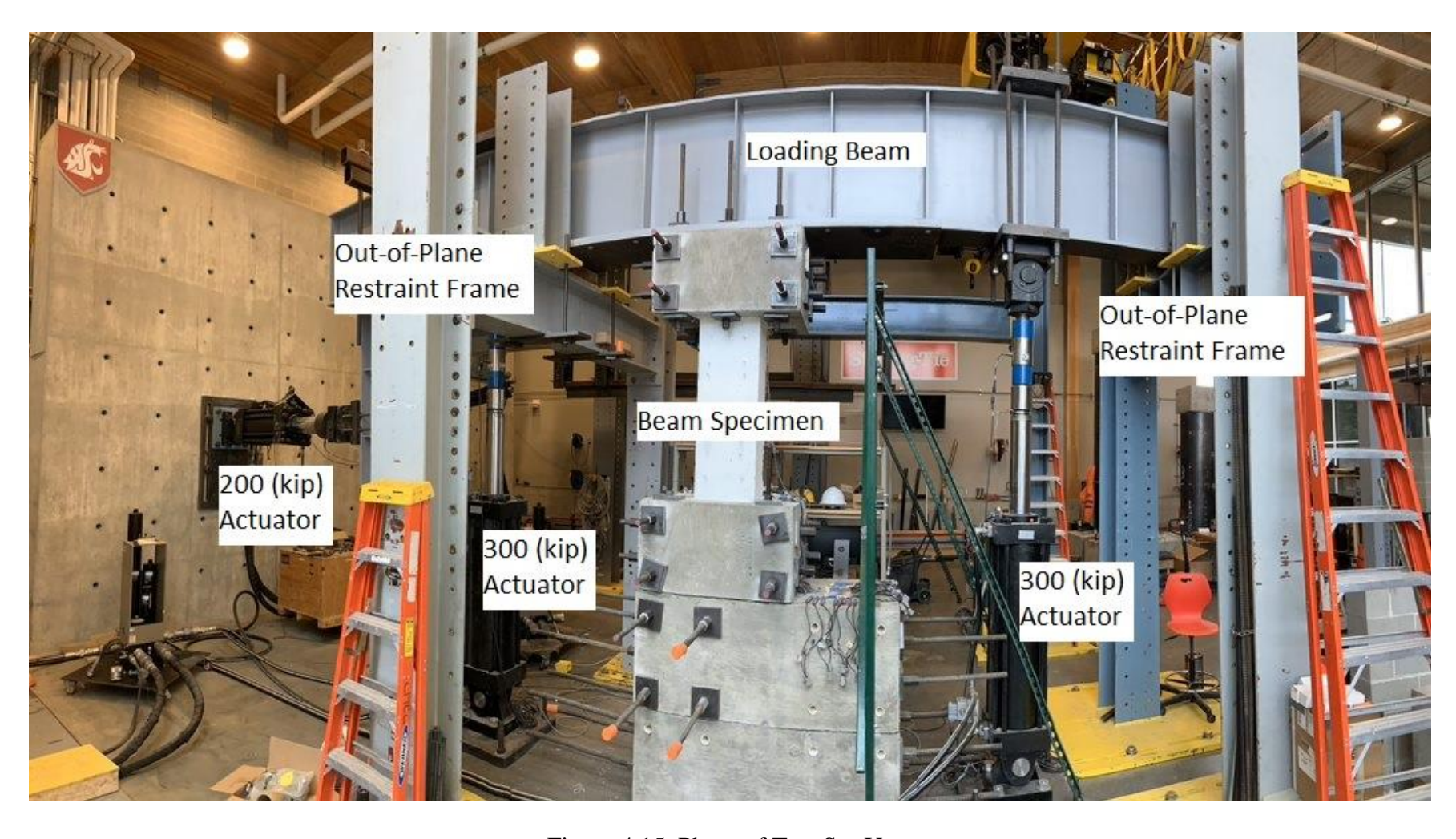


Figure 4.15. Photo of Test Set-Up

The loading frame consisted of W36x160 structural steel, with a 24' long horizontal member and 6' long vertical member. The vertical and horizontal members of the loading frame were attached with post-tensioned rods. The lateral actuator was post-tensioned to the vertical member. The two vertical actuators and the specimen top block were post-tensioned to the horizontal member of the loading frame. The bottom block of the specimen was post-tensioned to the strong floor. Two 24" tall concrete spacers were used to elevate the beam specimens from the ground in order to accommodate the length of the vertical actuators. A 4.0-kip plate was attached to the end of the horizontal member of the loading frame to counter the weight of the vertical steel beam and the lateral actuator.

To restrain the beam specimen from moving out-of-plane, two frames were created and used to prevent out-of-plane movement of the horizontal member of the loading frame near the two ends. Each frame was comprised of two 15' long W14x90 structural steel columns, a structural steel beam, and two 4' long W14x90 structural steel columns. The two longer columns were anchored to the laboratory strong floor with a steel beam spanning between. The two short columns were connected to the steel beam with a small gap between the columns and the horizontal member of the loading frame.

4.5 Instrumentation

Each beam was instrumented with linear variable differential transformers (LVDTs) and strain gauges. The LVDT layout is shown in Figure 4.16. Vertical LVDTs within the beam (L2-L9 and L12-L19) were used to measure axial-flexural deformations. Bond slip of longitudinal or diagonal

reinforcement in the bottom and top block was included in the displacement measured by the vertical sensors spanning 1" into the beam from the top and bottom block, shown in Figure 4.16 as L1, L9, L11 and L20. Diagonally oriented sensors were used to measured shear deformations. Shear sliding at the top and bottom of the beam was measured using horizontal sensors spanning between the beam and the top and bottom concrete blocks (L43 and L44). Axial elongation of the beam was recorded using vertical LVDTs spanning over the length of the beam and attached at the top and bottom blocks (L22 and L25). Bottom block uplift was measured using vertical LVDTs spanning from the top of the bottom block to the floor (L21 and L24). The top block rotation was determined from displacement values measured with LVDTs spanning from the bottom of the top block to the loading beam (L23 and L26). Lateral displacement at the top of the test beam was measured at the bottom of the top block using an LVDT (L46) and a string potentiometer (P1) that had longer stroke than the LVDT. Sliding of the bottom block was measured at the top of the bottom block using an LVDT (L45). LVDTs were attached to the ½" threaded rods cast into the beams, and a photo of one of the instrumented test beams is shown in Figure 4.17.

Eleven strain gauges were installed in each beam with span-to-depth ratio of 3.0, and eight strain gauges were installed in the beam with span-to-depth ratio of 1.5. All strain gauges in each beam were installed on one of the diagonal bars in the diagonally reinforced beams and one of the longitudinal bars in the conventionally reinforced beams. Some of the gauges were located in the beam and some were located in the support, as shown in Figure 4.18. The layout of strain gauges was intended to collect data that would aid in the understanding of the spread of plasticity into the beam and into the support (bottom or top block).

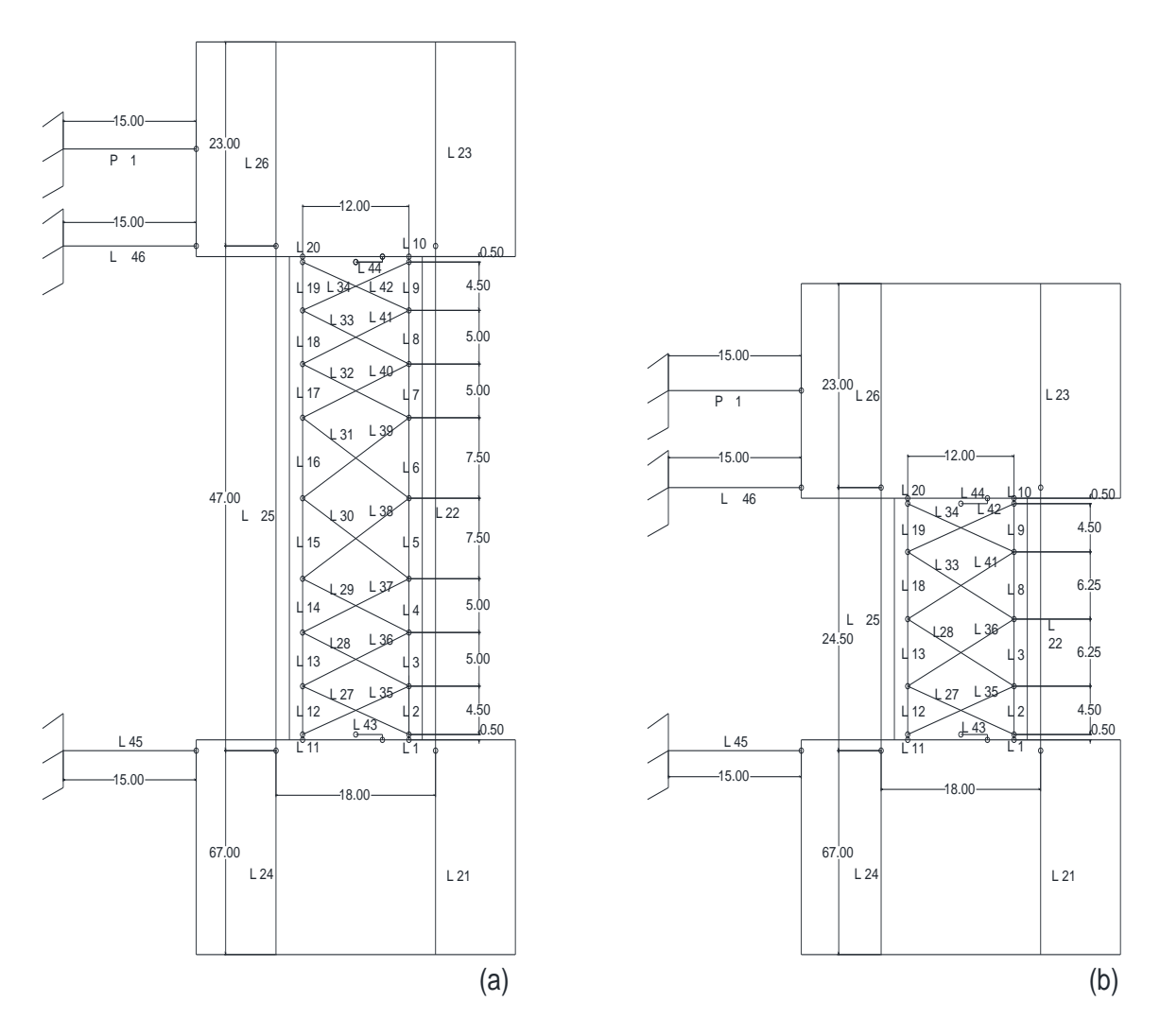


Figure 4.16. LVDT Layout for: a) Beams with Span-to-Depth Ratio of 3.0 and b) Beam with Span-to-Depth Ratio of 1.5

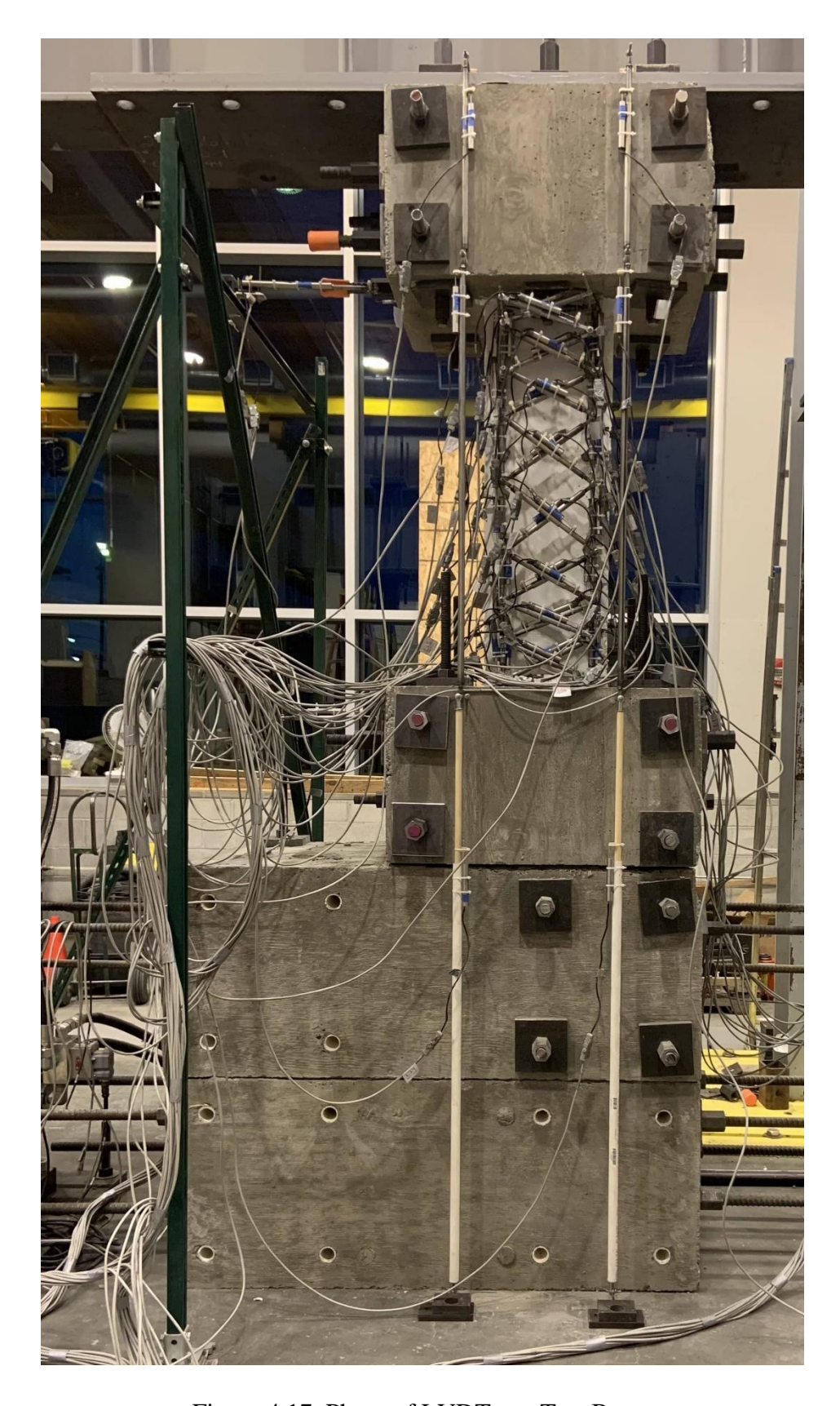


Figure 4.17. Photo of LVDTs on Test Beam

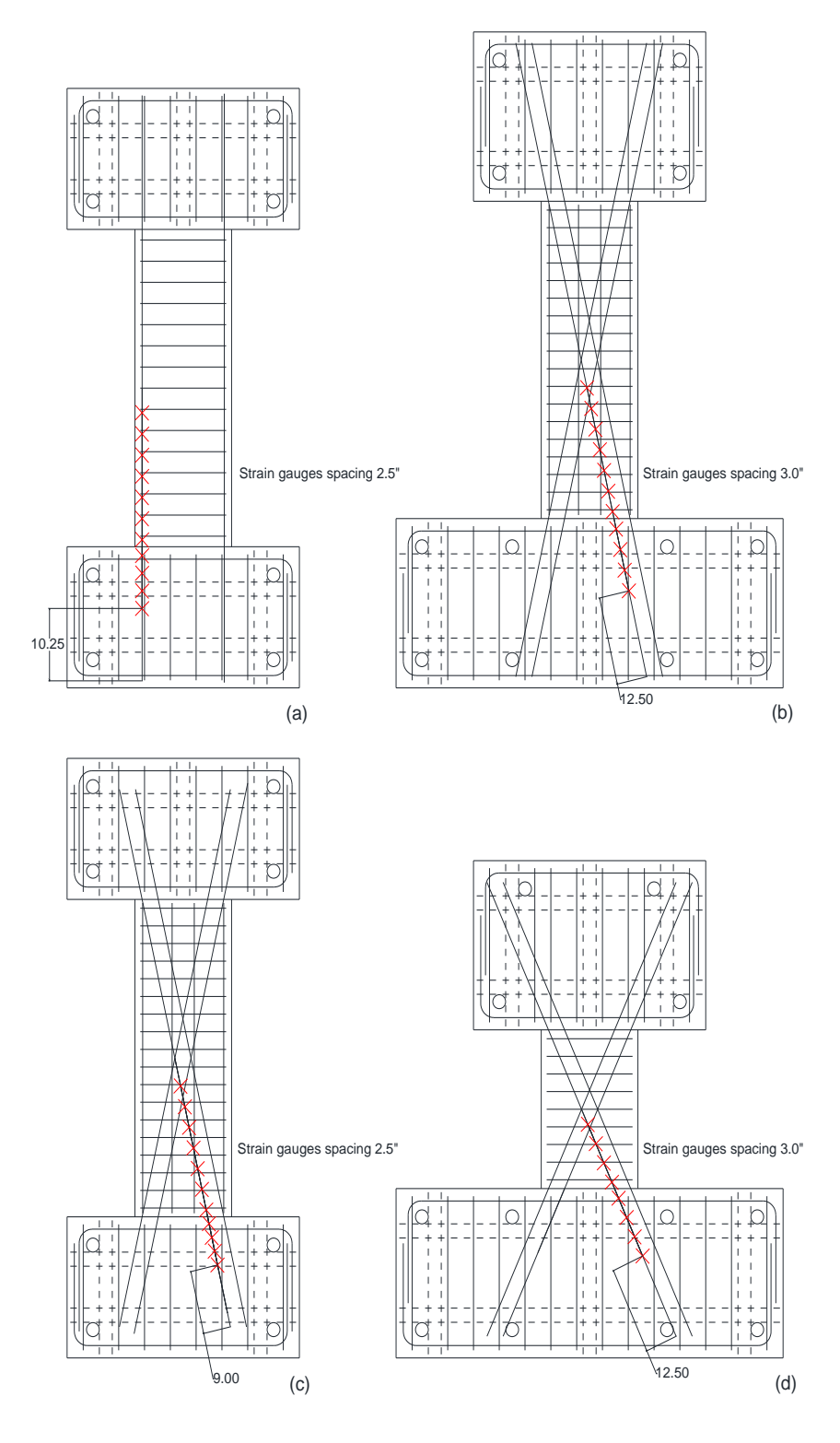


Figure 4.18. Strain Gauge Layout for: a) C(#5)-3.0-0.69 and C(#5)-3.0-0.35, b) D(#6)-3.0-0.69 and D(#6)-3.0-1.38, c) D(#4)-3.0-0.69 and d) D(#4)-3.0-1.38, and d) D(#6)-1.5-0.69

4.6 Loading Protocol

The test beam was subjected to both axial and lateral loads. The two vertical actuators were programmed to apply a total vertical load that was proportional to axial elongation of the beam while maintaining zero rotation over the height of the actuators. The programming and controlling of the vertical actuators was done using MTS MultiPurpose TestWare software. Two external channels and two virtual calculated channels were defined for control. The two external channels were the recorded axial elongation using LVDTs L22 and L25. The virtual calculated channels were for the calculated force and calculated displacement used to command the applied force and displacement of the actuators as:

$$A1F = \frac{L22 + L25}{2} * k_{axial} - A2F \tag{4.4}$$

$$A2D = A1D \tag{4.5}$$

where A1F and A2F are the forces in the first and second vertical actuators, respectively, A1D and A2D are the displacements of these actuators, L22 and L25 are the axial elongation measured by these LVDTs, and k_{axial} was the axial compressive stiffness. k_{axial} was constant during each test, with the values provided in Table 4.1.

Fully reversed cyclic lateral loading was applied through displacement controlled cycles (percent chord rotation increments) as shown in Figure 4.19. Three cycles were applied at each of 0.125%, 0.25%, 0.375%, 0.50%, 0.75%, 1.0%, 1.5%, 2.0% and 3.0% chord rotation. This was followed by application of two cycles at each of 4.0%, 6.0%, 8.0%, and 10.0% chord rotation. Control of the

horizontal actuator was independent of control of the vertical actuators, and the horizontal actuator was manually controlled throughout the test. The chord rotation, θ , used to control the cyclic lateral load was determined as:

$$\theta = \frac{L46 - L45}{H} - \frac{L24 - L21}{L} - \frac{L25 - L22}{2L} \tag{4.6}$$

where H is the height of the beam, and L is the horizontal distance between the two sensors, as shown in Figure 4.20. In Eq. (4.6), the first term includes a correction for sliding of the bottom block, the second term is a correction for rotation of the bottom block, and the third term is a correction for rotation over the length of the beam (i.e., rotation of the top block relative to the bottom block). The correction for the rotation of the beam was taken as half of the rotation measured over the length of the beam. A demonstration of the deformed shape of the beam specimen and the LVDTs associated with calculating the corrected chord rotation is shown in Figure 4.20. Beyond 6.0% rotation for the beams with span-to-depth ratio of 3.0, the reading from the string potentiometer, P1, was used in place of L46 for the calculation of the corrected chord rotation in Eq. (4.6).

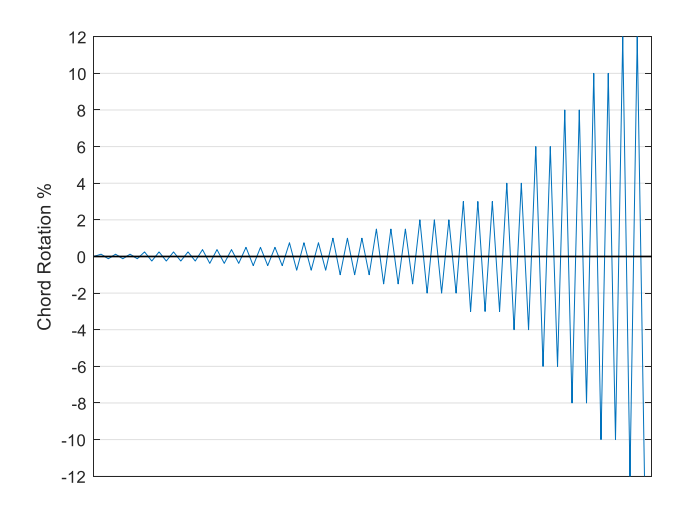


Figure 4.19. Loading Protocol

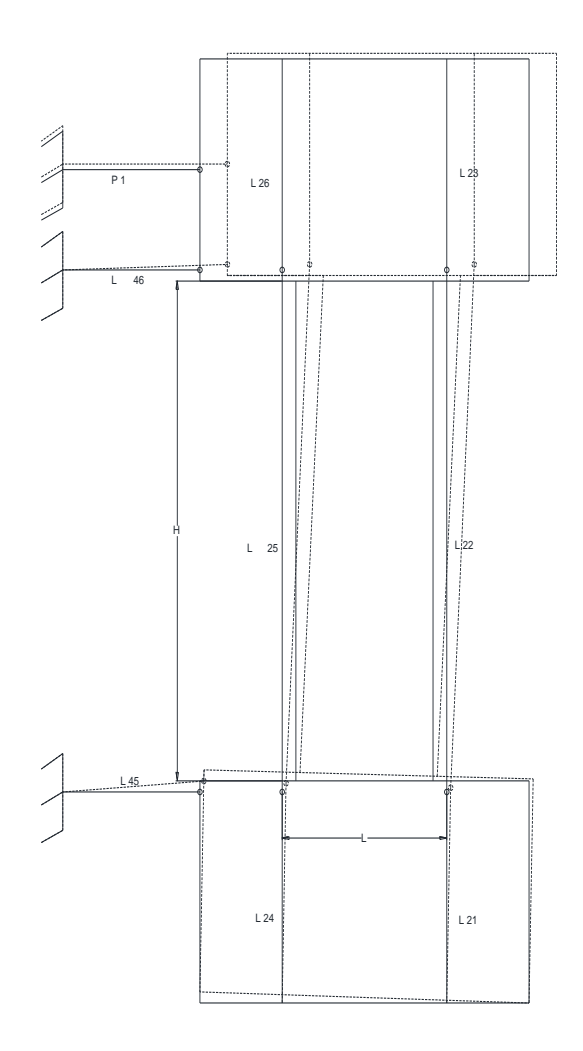


Figure 4.20. LVDTs Use to Determine Measured Chord Rotation

5. EXPERIMENTAL RESULTS AND DISCUSSION

5.1 Observed Damage

Damage photos for the test beams at peak deformation are provided in Figure 5.1 through Figure 5.7. The cycle at which damage states were first observed for each beam are summarized in Table 5.1. Axial-flexural cracks refer to those perpendicular to the beam length and initiating at the extreme fibers. Shear cracks refer to diagonal cracks crossing the centerline of the beam.

Axial-flexural cracking initiated in all test beams at 0.125% rotation. For the two frame beams, C(#5)-3.0-0.69 and C(#5)-3.0-0.35, larger axial compressive stiffness was associated with the onset of shear cracking at larger chord rotation and the onset of concrete crushing and spalling at smaller chord rotation. Shear cracks widened with increased deformation demand, characteristic of a shear yielding response. A large extensive flexural shear crack (0.1" width crack) was observed at the top south corner at 2.0% rotation for C(#5)-3.0-0.69, whereas the same size flexural shear crack was measured in C(#5)-3.0-0.35 at 3.0% rotation. Crack widths at the first cycle of each chord rotation increment are provided in Table 5.2. Concrete crushing concentrated at the top south end for C(#5)-3.0-0.69 and at the top and bottom north end for C(#5)-3.0-0.35, and core concrete spalled at locations where damage concentrated. At completion of the tests, longitudinal reinforcement had not fractured.

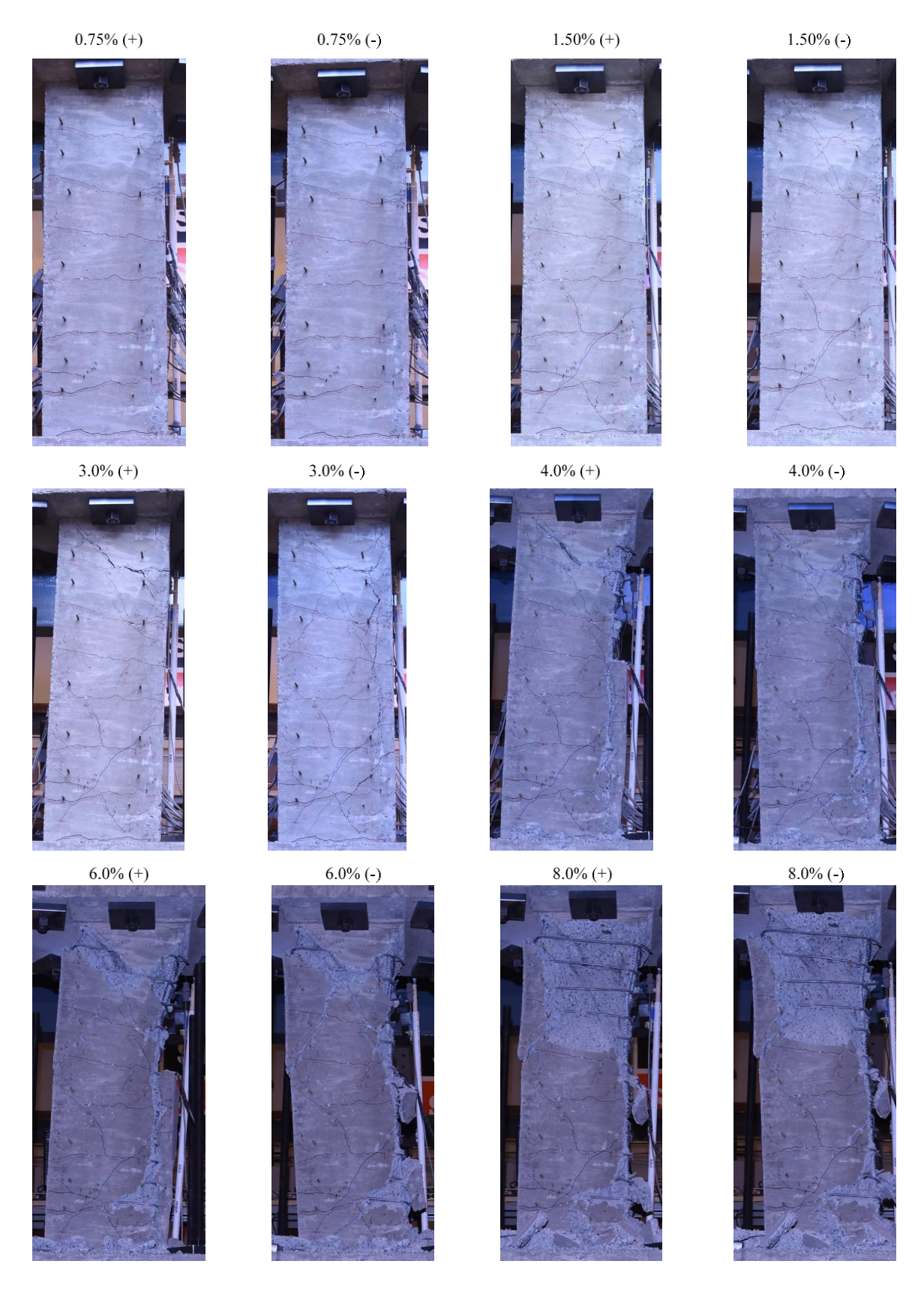


Figure 5.1. Damage Photos for C(#5)-3.0-0.69 at First Cycle Displacement Peaks

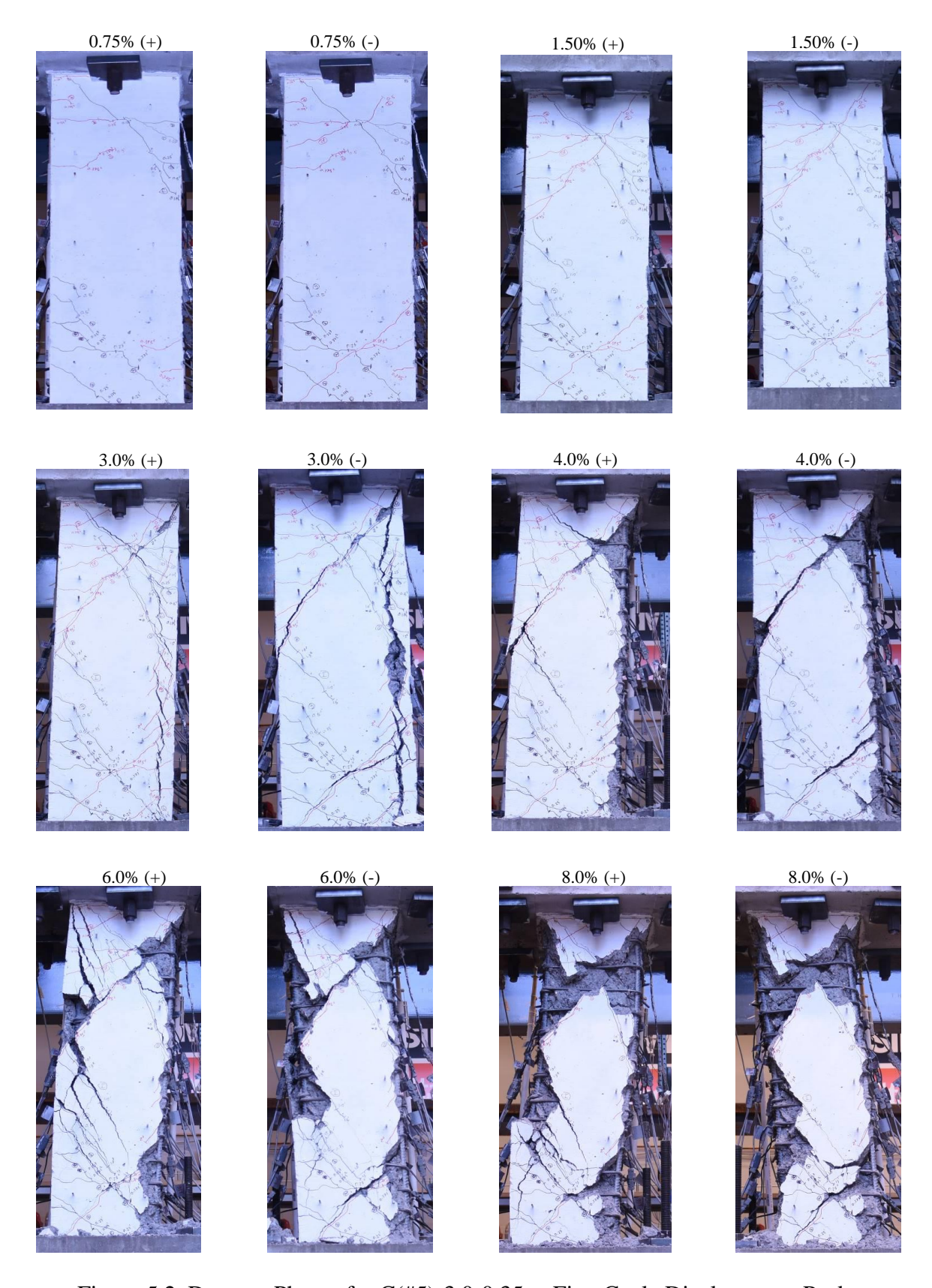


Figure 5.2. Damage Photos for C(#5)-3.0-0.35 at First Cycle Displacement Peaks

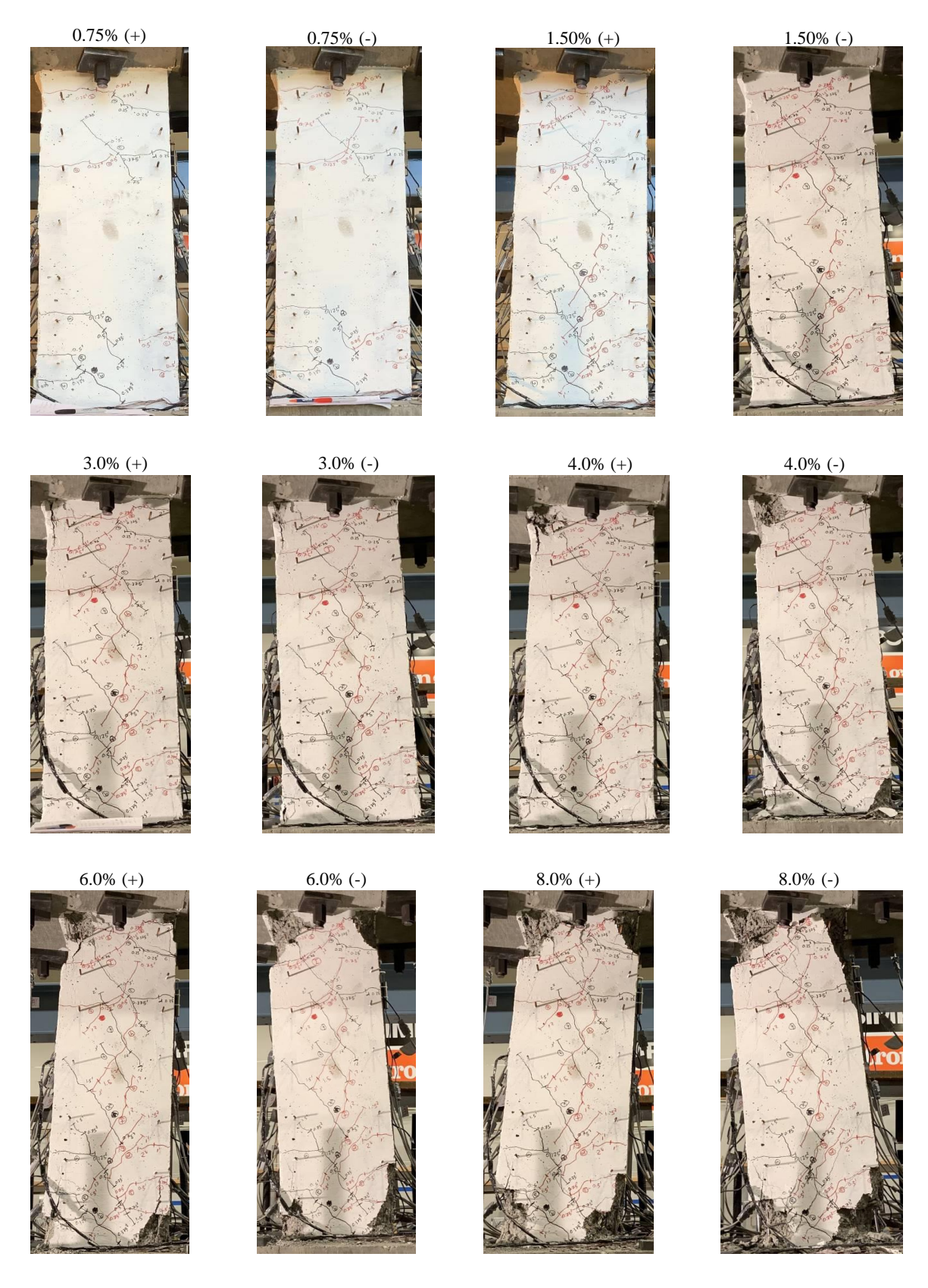


Figure 5.3. Damage Photos for D(#4)-3.0-0.69 at First Cycle Displacement Peaks

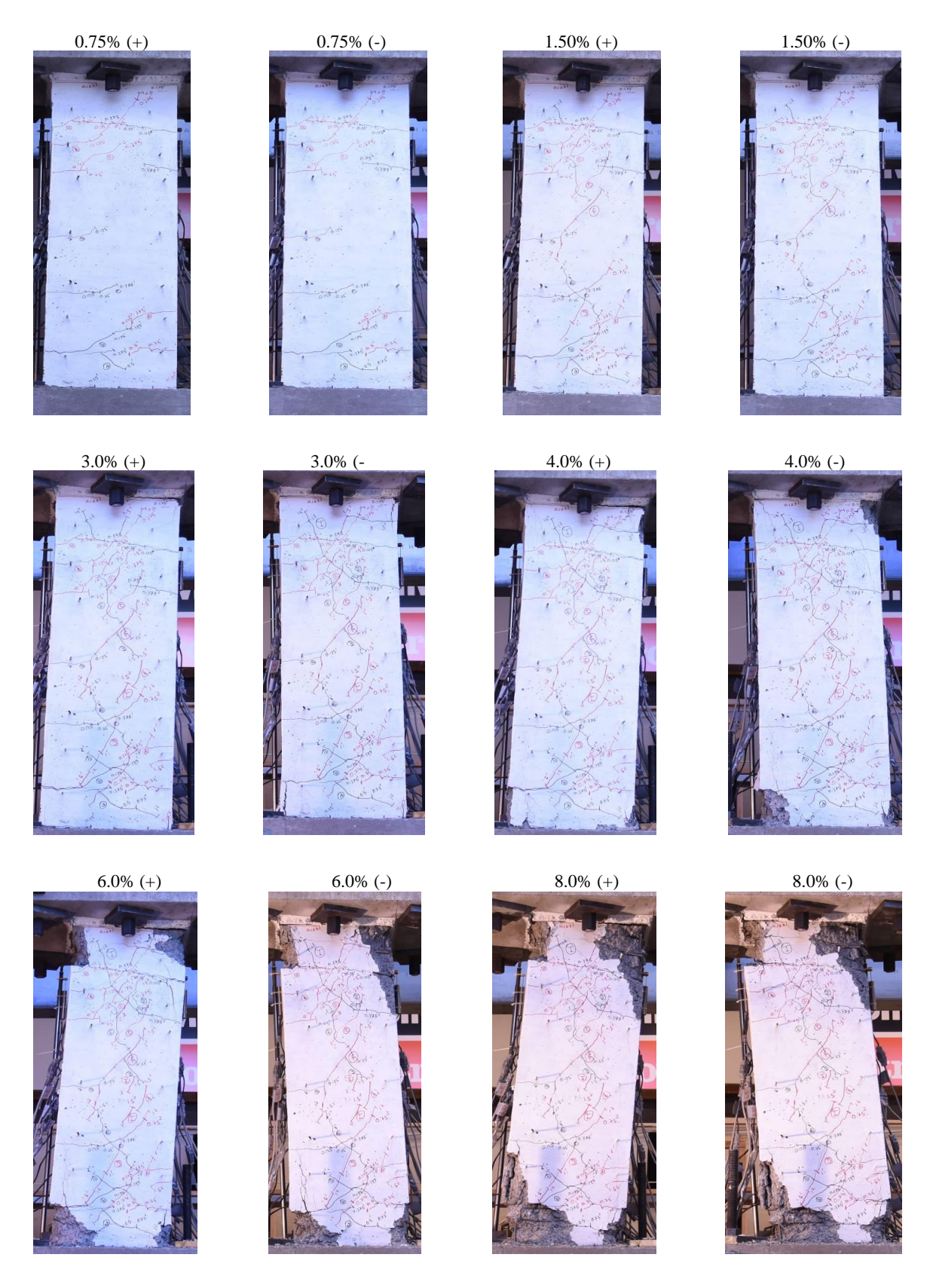


Figure 5.4. Damage Photos for D(#4)-3.0-1.38 at First Cycle Displacement Peaks



Figure 5.5. Damage Photos for D(#6)-3.0-0.69 at First Cycle Displacement Peaks



Figure 5.6. Damage Photos for D(#6)-3.0-1.38 at First Cycle Displacement Peaks



Figure 5.7. Damage Photos for D(#6)-1.5-0.69 at First Cycle Displacement Peaks

Table 5.1. Chord Rotation at Onset of Major Damage Events

Beam Name	First axial-	First axial-	First	Concrete	Concrete	Bar	Bar
	flexure	flexure	shear	crushing	spalling	buckling	fracture
	crack at	crack within	crack				
	interface	beam span					
C(#5)-3.0-0.69	0.125%	0.125%	0.75%	2.0%	3.0%	None	None
C(#5)-3.0-0.35	0.125%	0.125%	0.25%	3.0%	4.0%	None	None
D(#4)-3.0-0.69	0.125%	0.125%	0.375%	2.0%	4.0%	6.0%	8.0%
D(#4)-3.0-1.38	0.125%	0.125%	0.375%	2.0%	3.0%	6.0%	6.0%
D(#6)-3.0-0.69	0.125%	0.125%	0.375%	2.0%	3.0%	10.0%	10.0%
D(#6)-3.0-1.38	0.125%	0.125%	0.25%	1.5%	2.0%	10.0%	12.0%
D(#6)-1.5-0.69	0.125%	0.125%	0.25%	2.0%	3.0%	10.0%	10.0%

Table 5.2. Maximum Measured Crack Widths

Beam Name	Chord Rotation Level											
	0.25%		0.50%		1.0	%	2.0)%	3.0%			
	Flexure	Shear	Flexure	Shear	Flexure	Shear	Flexure	Shear	Flexure	Shear		
C(#5)-3.0-0.69	0.016	-	0.024"	-	0.102"	0.047"	0.102"	0.102"	0.177"	0.157"		
C(#5)-3.0-0.35	0.02"	0.016"	0.028"	0.028"	0.039"	0.047"	0.118"	0.072"	0.196"	0.102"		
D(#4)-3.0-0.69	0.007"	-	0.016"	0.004"	0.031"	0.016"	0.087"	0.024"	0.236"	0.031"		
D(#4)-3.0-1.38	0.016"	_	0.031"	0.012"	0.063"	0.016"	0.196"	0.02"	0.079"	0.024"		
D(#6)-1.5-0.69	0.008"	_	0.020"	0.004"	0.063"	0.012"	0.197"	0.012"	0.25"	0.031"		

For the diagonally reinforced beams, shear cracks were first observed at 0.25% rotation for D(#6)-3.0-1.38 and D(#6)-1.5-0.69 and 0.375% for the other three test beams. Of the four test beams with span-to-depth ratio of 3.0, D(#6)-3.0-1.38 was expected to have the largest compression demands at a given drift level, due to the greater neutral axis depth caused by a combination of high axial load and high longitudinal reinforcement ratio. Concrete crushing was observed to initiate at 1.5% for this beam relative to 2.0% for the other three. Spalling was first observed at 2.0% for this beam, compared to 3.0% for D(#6)-3.0-0.69 and D(#4)-3.0-1.38 and 4.0% for D(#4)-3.0-0.69, noting that D(#4)-3.0-0.69 was expected to have the lowest compression demands at a given drift level. For

the beams with span-to-depth ratio of 3.0, concrete spalling and reinforcement buckling and fracture concentrated at the top and bottom of the diagonally reinforced beams, characteristic of a flexure-yielding beam response with plasticity at the beam ends. For the beam with aspect ratio 1.5, spalling also occurred at mid-depth at mid-span and buckling and fracture of diagonal reinforcement spread over the length of the beam. Buckling of diagonal reinforcement was first observed at 6% rotation for the two beams with #4 diagonal reinforcement and 10% rotation for the three beams with #6 diagonal reinforcement. The trend is qualitatively consistent with previous research (e.g., Rodriguez et al, 1999) that demonstrates an increased likelihood for bar buckling as the ratio of transverse reinforcement spacing to longitudinal bar diameter, s/d_b , is increased. The difference in axial stiffness and the associated effect on the strain history in the reinforcement had little impact on the initiation of bar buckling relative to the change in s/db. A summary of the bar fractures in each test is provided in Table 5.3.

Table 5.3. Number of Bar Fractures at Each Cycle

Beam Name		Chord Rotation Level and Cycle Number														
	6% (1)		1) 6% (2)		8% (1)		8%	8% (2) 10% (1)		10% (2)		12% (1)		12% (2)		
	+	-	+	-	+	-	+	-	+	-	+	-	+	-	+	_
C(#5)-3.0-0.69		None														
C(#5)-3.0-0.35		None														
D(#4)-3.0-0.69	0	0	0	0	3	0	3	0	0	0	0	0	-	-	-	-
D(#4)-3.0-1.38	0	0	1	0	1	0	7	0	2	0	0	4	4	1	-	-
D(#6)-3.0-0.69	0	0	0	0	0	0	0	0	0	0	2	0	-	-	-	-
D(#6)-3.0-1.38	0	0	0	0	0	0	0	0	0	0	0	0	1	2	2	3
D(#6)-1.5-0.69	0	0	0	0	0	0	0	0	0	0	1	2	2	3	1	1

5.2 Axial Elongation and Axial Restraint

Axial elongation of the beams was measured over the length of the beam with two LVDTs, shown in Figure 4.16 and discussed in Section 4.6. The axial force applied to each beam was based on k_{axial} , as discussed in Section 4.7. The chord rotation versus axial elongation is provided in Figure 5.8 for each test beam. The response is generally close to linear elastic for all beams, until damage caused the elongation at cycle peaks to decrease as demand increased. At the largest applied deformation levels, many of the beams had shortened due to damage, such that axial tension was applied. The responses of D(#4)-3.0-1.38 and D(#6)-3.0-0.69 have noticeable asymmetry. This was attributed to out-of-plane rotation of the top block, which influenced the axial elongation sensor used to control the applied axial load. The measured peak axial force (P_{max}), peak axial elongation (Δ_{max}), chord rotation at which the maximum axial force was achieved ($\theta_{e}P_{max}$), and the normalized maximum axial force ($P_{max}/(A_g f^*c)$) are provided in Table 5.4 for each beam. For each of the three pairs of nominally identical beams, the average peak axial load is larger for the beam with larger axial stiffness, as expected. However, due to the asymmetry for D(#4)-3.0-1.38 and D(#6)-3.0-0.69, this trend is not true when comparing values in the positive and negative direction.

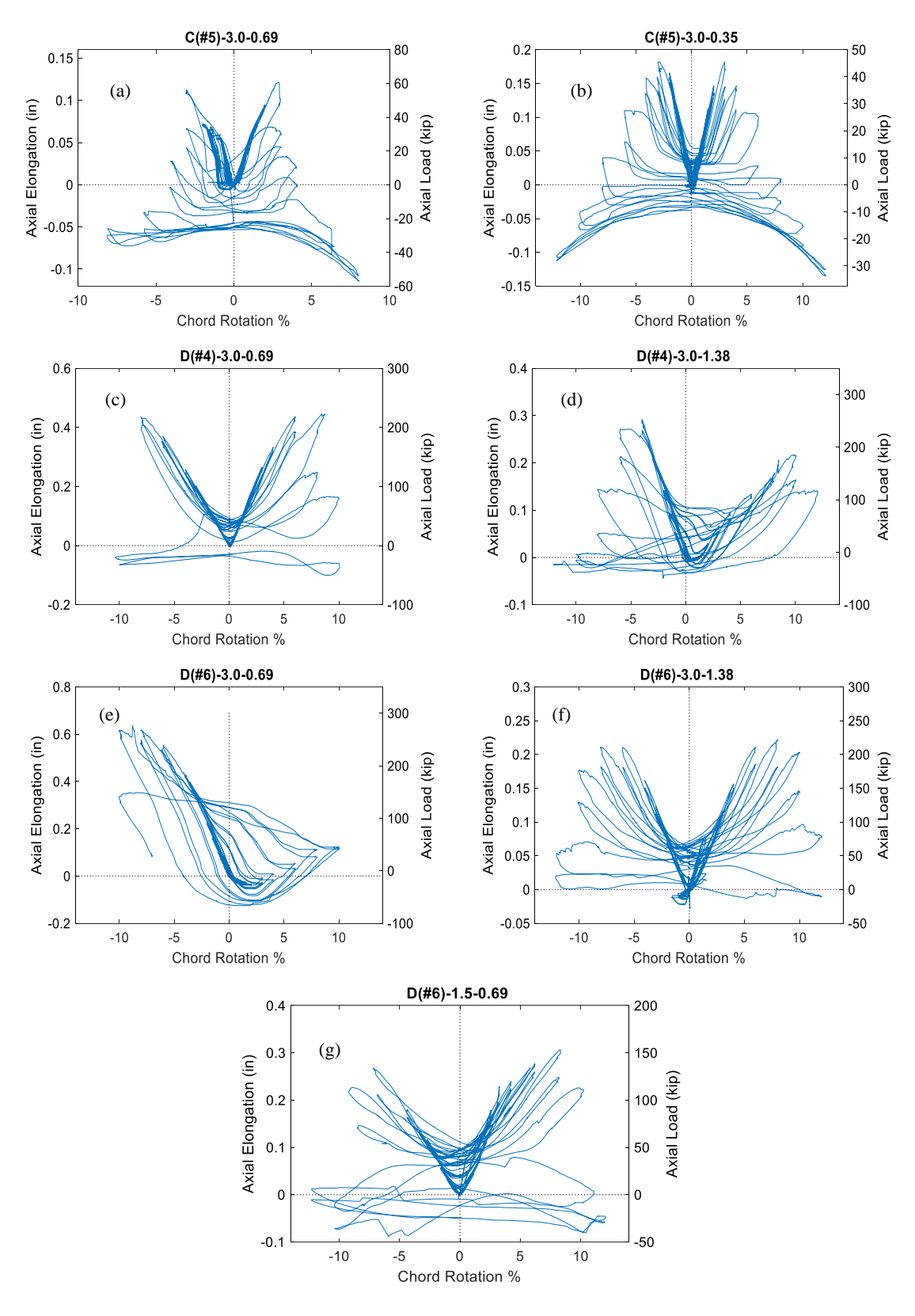


Figure 5.8. Axial Elongation and Force for: a) C(#5)-3.0-0.69, b) C(#5)-3.0-0.35, c) D(#4)-3.0-0.69, d) D(#4)-3.0-1.38, e) D(#6)-3.0-0.69, f) D(#6)-3.0-1.38, and g) D(#6)-1.5-0.69

Table 5.4. Measured Peak Axial Load and Corresponding Deformation

Beam Name	+P _{max}	-P _{max}	Pavg	$+\Delta_{\max}$	$-\Delta_{max}$	$+\theta_{@Pmax}$	-θ@Pmax	P _{max} /f'c*A _g	Pavg/f'c*Ag
	(kip)	(kip)	(kip)	(in)	(in)	(%)	(%)		
C(#5)-3.0-0.69	60.5	55.9	58.2	0.121	0.112	-3.0%	3.0%	0.096	0.092
C(#5)-3.0-0.35	45.4	45.4	45.4	0.182	0.182	-3.0%	3.0%	0.072	0.072
D(#4)-3.0-0.69	217	223	220	0.446	0.434	-8.4%	8.0%	0.352	0.349
D(#4)-3.0-1.38	216	291	253.5	0.216	0.291	-10.0%	4.0%	0.462	0.402
D(#6)-3.0-0.69	61	319	190	0.122	0.637	-9.8%	8.8%	0.506	0.301
D(#6)-3.0-1.38	211	222	216	0.222	0.211	-8.0%	8.0%	0.351	0.342
D(#6)-1.5-0.69	151	134	142	0.302	0.267	-8.3%	7.2%	0.274	0.259

The maximum axial force was reached in the two frame beams at 3.0% rotation, and there was extensive shear cracking at that level. Axial shortening followed at 4.0% rotation and the subsequent chord rotation increments. More gradual axial shortening was experienced for C(#5)-3.0-0.35 than C(#5)-3.0-0.69. The axial elongation of the frame beams was less than the diagonally reinforced beams, as the frame beams were observed to yield in shear. In comparing the diagonally reinforced concrete coupling beams, the maximum axial force was reached at 4.0% chord rotation for D(#4)-3.0-1.38 and around 8.0% for the other four beams. The peak axial compressive stress ranged from 0.35-0.51 P_{max}/(A_gf'c) for the beams with span-to-depth ratio of 3.0 and was 0.27 for D(#6)-1.5-0.69 with span-to-depth ratio of 1.5, indicating that significant compressive demands were acting on the beams at peak axial load. In these calculations, f'c was taken as the measured concrete compressive strength reported in Section 4.3. Despite the high levels of compressive demand, fracture of transverse reinforcement associated with crushing failure of the confined core concrete was not observed. In comparing the beams with span-to-depth ratio of 3.0 with the same axial stiffness and different bar size, the larger bar size led to a 14-15% increase in P_{max,avg} and more gradual axial shortening due to damage. Shorter beam length led to reduced axial elongation.

5.3 Force-Deformation

The force-deformation response of each test beam is provided in Figure 5.9. Measured strength and deformation at various levels are provided in Table 5.5. This includes the peak shear force, V_{max} , in the positive and negative directions, the chord rotation when these peak shear forces were attained, $\theta_{@V_{max}}$, and the chord rotation at which lateral failure occurred, $\theta_{>20\%}$. Lateral failure was defined to occur at the first cycle peak at which a 20% or greater loss of peak strength occurred and was sustained for the remainder of the test. In Table 5.5, the peak shear strength is also provided with normalization to the following: The nominal shear strength (V_{n}) calculated in accordance with ACI 318-19 (Eq. (3.21), termed $V_{n,ACI}$ in Table 5.5) and using the modified equation (Eq. 3.22, termed $V_{n,new}$ in Table 5.5); the shear force at nominal moment calculated at the measured peak axial force; and $\sqrt{f'c}$ *Acv. $V_{n,new}$ was computed using the larger of the absolute value of positive and negative P_{max} provided in Table 5.4. Calculation of $V_{@Mn}$ was consistent with the approach described in Section 3.1.

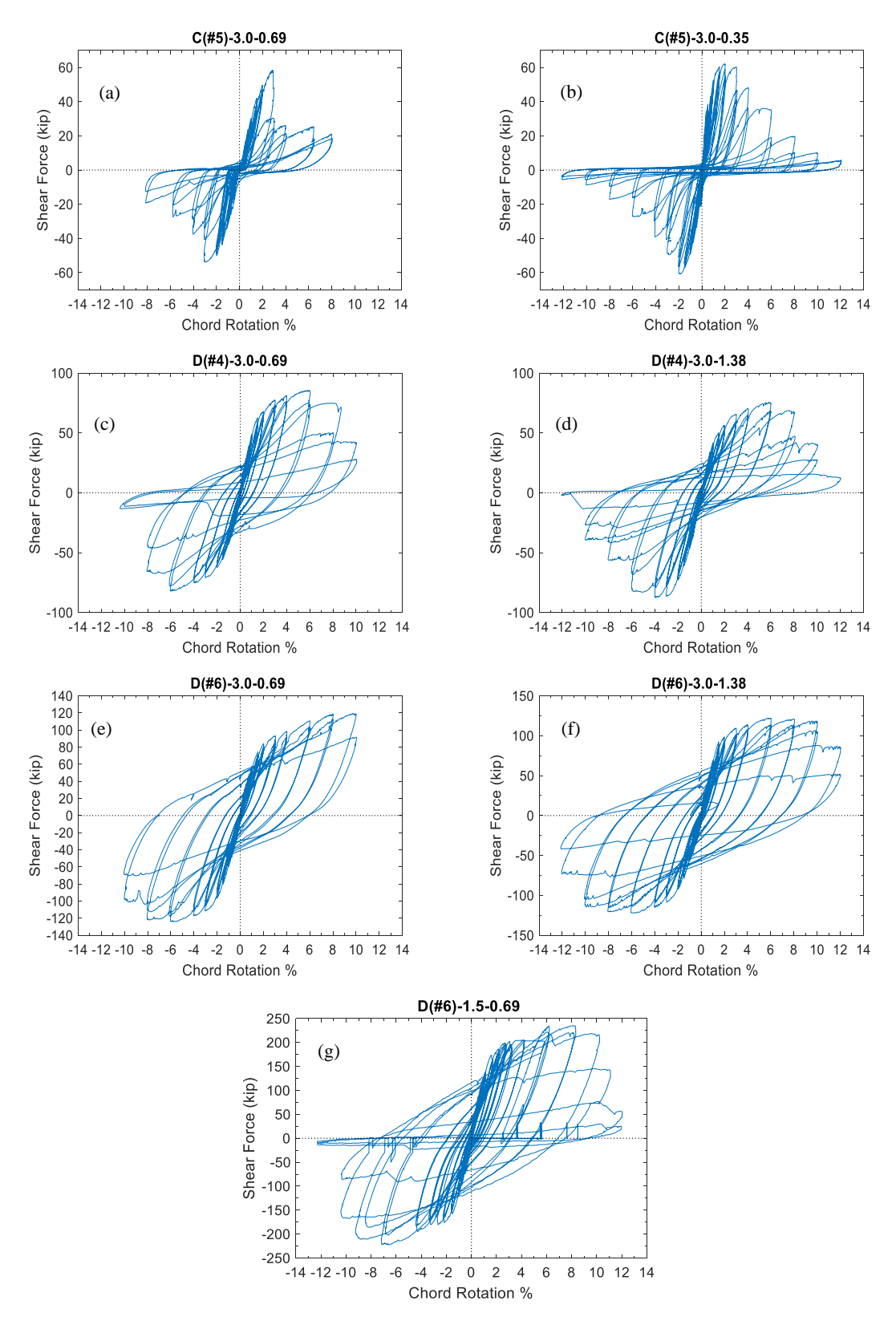


Figure 5.9. Load-Displacement Responses of: a) C(#5)-3.0-0.69, b) C(#5)-3.0-0.35, c) D(#4)-3.0-0.69, d) D(#4)-3.0-1.38, e) D(#6)-3.0-0.69, f) D(#6)-3.0-1.38, and g) D(#6)-1.5-0.69

Table 5.5. Measured Strength

Beam Name	V _{max} (k)		θ _{@Vmax} %		θ _{>20% str}	$\frac{V_{max}}{V_{n\ ACI}}$	$\frac{V_{max}}{V_{@M_n}}^a$	$\frac{V_{max}^{b}}{V_{@M_n}}$	$\frac{V_{max}}{A_{cw}\sqrt{f_c'}}$	$\frac{V_{max}^{c}}{V_{n new}}$	$\frac{V_{max}}{V_{n \ new}}^d$	
	(+)	(-)	(+)	(-)	(+)	(-)						
C(#5)-3.0-0.69	54	58	3.0%	3.0%	3.0% (2) ^e	3.0% (2)	0.53	0.98	1.32	5.45	0.55	0.42
C(#5)-3.0-0.35	61	62	2.0%	2.0%	3.0% (2)	3.0% (2)	0.57	1.11	1.41	5.82	0.58	0.46
D(#4)-3.0-0.69	82	84	6.0%	6.0%	8.0% (2)	8.0% (2)	2.34	1.28	2.10	7.89	0.79	0.38
D(#4)-3.0-1.38	88	76	4.0%	6.0%	6.0% (2)	8.0% (2)	2.45	1.39	2.20	8.26	0.83	0.38
D(#6)-3.0-0.69	124	119	6.0%	10.0%	10.0% (2)	10.0% (2)	1.62	1.53	1.67	11.64	1.16	0.45
D(#6)-3.0-1.38	122	122	6.0%	6.0%	12.0% (1)	12.0% (1)	1.59	1.37	1.64	11.46	1.15	0.47
D(#6)-1.5-0.69	221	235	7.0%	8.0%	10.0% (1)	10.0% (2)	1.62	1.36	1.68	23.6	2.36	0.74

a: V_{@Mn} was calculated for the peak measured axial compressive load during the test.

In comparing the two frame beams, $\theta_{\text{@Vmax}}$ was reached at 3.0% chord rotation for C(#5)-3.0-0.69 and 2.0% chord rotation for C(#5)-3.0-0.35. Post-peak strength degradation was rapid, and $\theta_{\text{>20\%}}$ occurred at the second cycle of 3.0% for both beams. Both beams experienced opening of shear cracks indicative of shear yielding, as shown in Figure 5.1 and Figure 5.2, with crack widths reported in Table 5.2. The shear strength of the beams was less than the nominal shear strength, with ratios of V_{max}/V_n provided in Table 5.5. The lack of deformations on the transverse reinforcement may have affected the anchorage, as this reinforcement did not fracture, despite the opening of significant diagonal crack widths. $\theta_{>20\%}$ for the shear yielding frame beams was significantly less than that of the flexure-yielding diagonally reinforced beams, as expected. Similarly, the rate of strength degradation and the level of pinching in the load-deformation response were larger for the shear yielding frame beams. For the two frame beams, strength degradation was more pronounced for C(#5)-3.0-0.69 than C(#5)-3.0-0.35.

b: V@Mn was calculated without considering the axial load.

c: $V_{\text{n new}}$ was calculated considering the upper limit $10\sqrt{f_c'}A_{cw}$.

d: $V_{\text{n new}}$ was calculated without considering the upper limit $10\sqrt{f_c'}A_{cw}$.

e: Percentage is chord rotation and the numeric between brackets is the cycle number.

In comparing $\theta_{>20\%}$ values for the diagonally reinforced concrete coupling beams in Table 5.5, deformation capacity of the test beams was more heavily influenced by the difference in reinforcement bar size than the level of axial restraint. Comparing the response of the beams reinforced with #4 bars with the beams reinforced with #6 bars under the same level of axial restraint, the beams with #6 bars had significantly larger deformation capacity. This is consistent with the observation that initiation of bar buckling and fracture occurred at lower rotation levels for the beams with #4 reinforcement, likely due to the lower s/d_b . Strength degradation primarily occurred due to buckling and fracture of reinforcement rather than crushing of confined concrete. Greater pinching is evident in the load-deformation response of the beams with #4 reinforcement relative to those with #6 reinforcement, similarly due to the bar buckling of the #4 reinforcement at lower levels of deformation demand.

 V_{max} was greater than $V_{n,ACI}$ by 134% for D(#4)-3.0-0.69, 145% for D(#4)-3.0-1.38, 62% for D(#6)-3.0-0.69, 59% for D(#6)-3.0-1.38, and 62% for D(#6)-1.5-0.69. This suggests that the ACI 318-19 V_n equation for diagonally reinforced coupling beams significantly underestimates shear strength, consistent with findings discussed in Section 3.4. For the proposed equation for V_n of diagonally reinforced concrete coupling beams (Eq. (3.22)), which considers the shear strength from concrete and transverse reinforcement in addition to the shear strength from the horizontal component of the diagonal reinforcement, calculations with and without inclusion of $10\sqrt{f_c'}A_{cw}$ are included in Table 5.5. It is evident from the values in Table 5.5 that V_{max} for the diagonally reinforced beams with #6 bars exceeded $10\sqrt{f_c'}A_{cw}$. This is consistent with the finding of Barney et al (1980) that diagonally reinforced coupling beams may develop shear forces in excess of $10\sqrt{f_c'}A_{cw}$. When

the $10\sqrt{f_c'}A_{cw}$ limit was excluded, the diagonally reinforced beams did not reach V_n , although it is noted that $V_{max}/V@M_n$ was at least 1.28 for each of the five diagonally reinforced beams. It was shown in Section 3.4 that Eq. (3.22) corrects for the significant underprediction of nominal shear strength of the beams in the database and is recommended for use over the ACI equation.

The load-deformation response of the shear yielding frame beams tested in this study differed significantly from flexure-yielding frame beams tested in other studies, such as FB33 reported by Naish et al. (2013) and HB3-6L-T100 reported by Xiao et al. (1999). FB33 and HB3-6L-T100 displayed significant flexural yielding, with sustained post-yield strength until at least 4% chord rotation, as shown in Figure 5.10, and damage concentration at the ends of the beams, as shown in Figure 5.11. However, C(#5)-3.0-0.35 yielded in shear, with rapid post-peak strength degradation and diagonal cracking. The flexure-yielding response was associated with larger deformation capacity, as expected, with values of 4.0% for FB33, 3.7% for HB3-6L-T100, and 3.0% for C(#5)-3.0-0.35.

In Figure 5.12, the load-displacement response of D(#6)-3.0-1.38 is shown with that of CB33F (Naish et al., 2013), tested without axial restraint. CB33F and D(#6)-3.0-1.38 had span-to-depth ratios of 3.3 and 3.0, reinforcement ratios of 0.0193 and 0.0174, and s/db ratios of 3.33 and 3.43, respectively. Lateral failure occurred during the second cycle at 8.0% chord rotation for CB33F and the first cycle at 12.0% chord rotation for D(#6)-3.0-1.38. The axial restraint may have contributed to the increase in deformation capacity by delaying the onset of bar buckling.

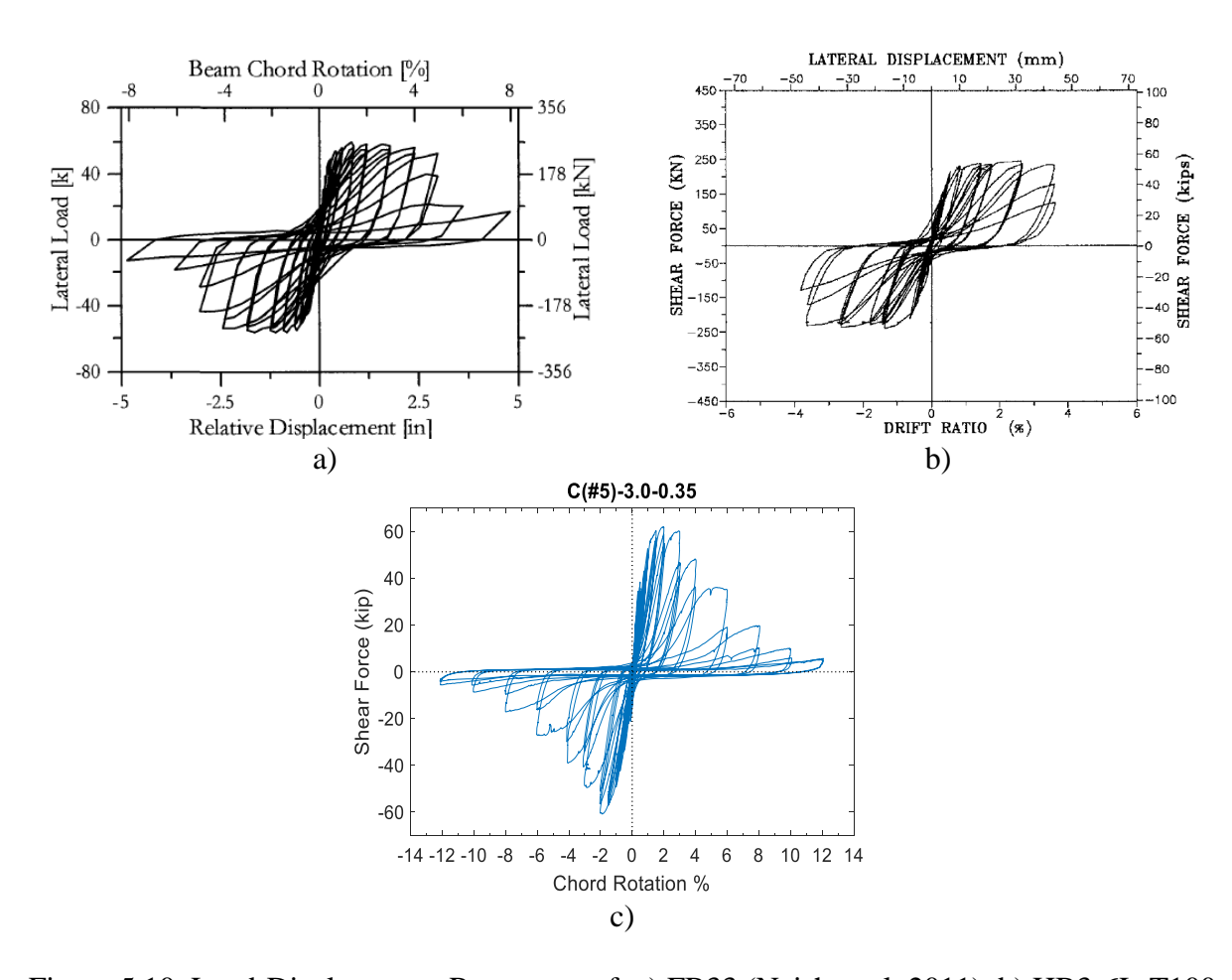


Figure 5.10. Load-Displacement Responses of: a) FB33 (Naish et al, 2011), b) HB3-6L-T100 (Xiao, 1999), and c) C(#5)-3.0-0.35

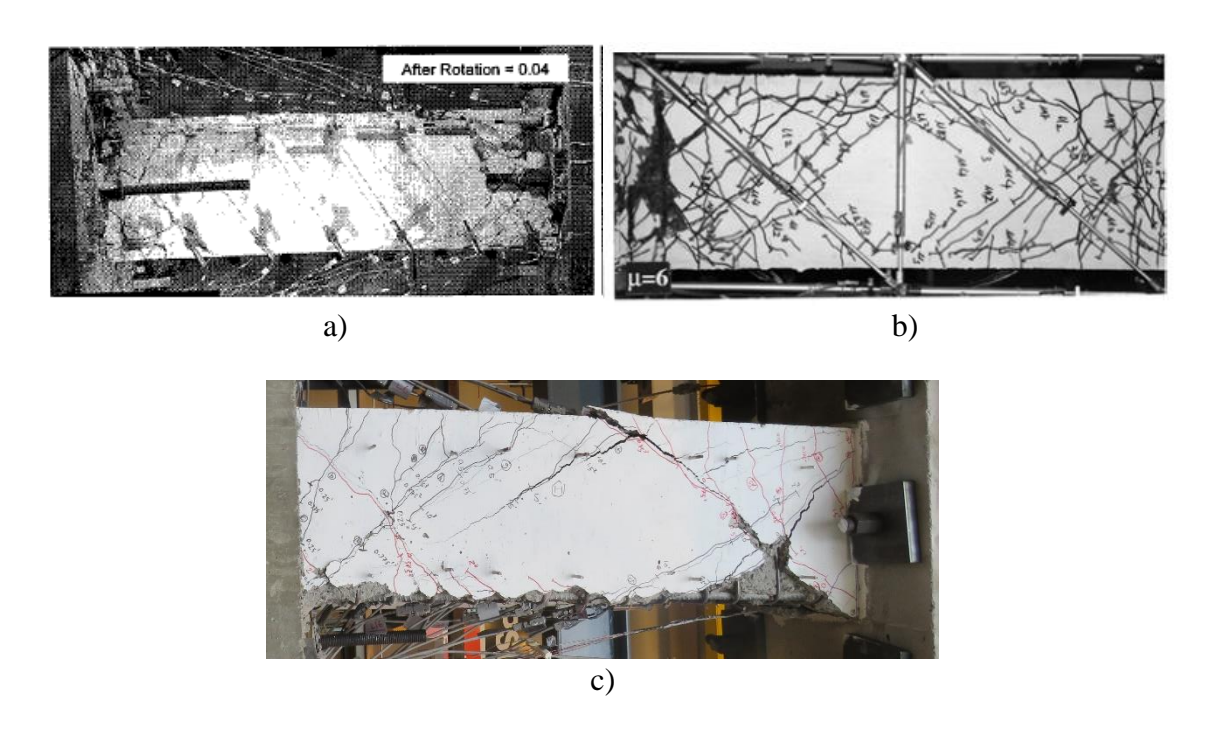


Figure 5.11. Observed Damage at 4.0% Chord Rotation for a) FB33 (Naish et al, 2011), b) HB3-6L-T100 (Xiao, 1999), and c) C(#5)-3.0-0.35

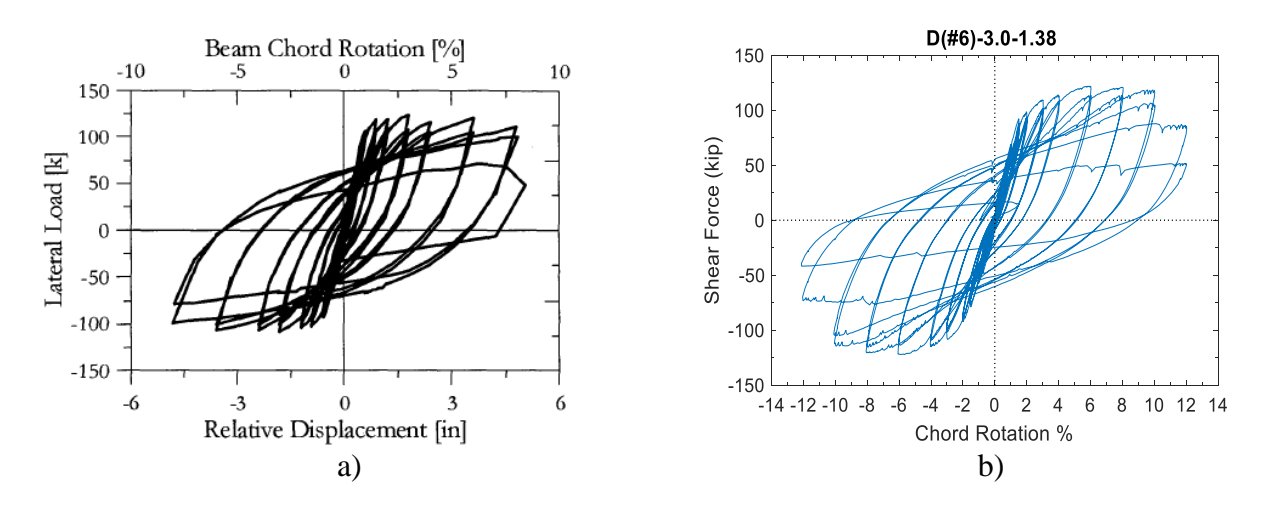


Figure 5.12. Load-Displacement Responses of: a) CB33F (Naish et al, 2011) and b) D(#6)-3.0-1.38

Using Eq. (3.19), the deformation capacity of the diagonally reinforced coupling beams with #4 and #6 diagonal reinforcement was estimated as 5.6% and 7.5%, respectively. The measured

deformation capacity exceeded the predicted values by at least 15% for the five beams. Although the axial restraint on the test beams did not lead to a reduction in deformation capacity relative to these predicted values, the axial restraint led to a significant increase in strength. For the five diagonally reinforced beams, $V_{max}/V@M_n$ ranged from 1.28 to 1.53 when M_n was computed at the peak measured axial load and ranged from 1.64 to 2.20 when M_n was computed with zero axial load. For $V@M_n$ computed at peak axial load, the large $V_{max}/V@M_n$ values were attributed to M_n being compression-controlled, since the M_n computation was based on an outer fiber compressive strain of 0.003 for unconfined concrete. Based on the difference in $V@M_n$, the difference in strength between the test beams and equivalent unrestrained beams was estimated as 9%-64%, with larger values for smaller longitudinal reinforcement ratio. The increased coupling beam strength creates additional demands on the walls, noting that the effect of axial restraint is typically excluded when coupling beams are designed in practice. In this study, the constant axial compressive stiffness applied to the diagonally reinforced beams ranged from 0.69Agf'c to $1.38A_g f'_c$ per inch. Additional research is needed to characterize typical levels of axial restraint for coupling beams. ACI 318-19 does not explicitly recommend capacity design for coupled walls. It is recommended that an upper bound for coupling beam strength be used in the determination of wall demands, similar to the use of probable beam strength for the design of columns in special moment frames. If the probable moment strength of a coupling beam was computed in the same manner as a special moment frame beam (i.e., using $1.25f_y$), additional strength may be created by axial restraint as evident from the tests. Although further is research is needed to better characterize the level of overstrength, results from this study provide experimentally derived values of overstrength for the range of constant stiffness axial restraint levels considered in the study.

5.4 Components of Deformation

The contribution of flexure, including bond slip of reinforcement, and shear, including shear sliding, to total deformation for each beam is provided in Figure 5.13. The LVDTs used to measure deformation within the beam were described in Section 3.5. The displacement from flexure, $\delta_{flexure}$, associated with each pair of vertical LVDTs was calculated as:

$$\delta_{flexure} = \theta * (D) = \frac{\delta_1 - \delta_2}{L} * D$$
 (5.1)

where θ is the rotation from flexure over the length of the sensors, δ_1 and δ_2 are the readings of the two vertical LVDTs at the same bay, L is the distance between the LVDTs, and D is the distance from the midpoint of the LVDTs to the mid height of the beam. At both the top and bottom of the test beam, the flexure measured between the support and a location 1" into the beam was attributed to bond slip. Using the method described by Massone and Wallace (2004), shear displacement for each pair of diagonal sensors was corrected for flexural deformation. Sliding of the beam relative to the top and bottom blocks was based on single sensors located between the beam and the top or bottom block (L43 and L44).

From Figure 5.13 it is evident that shear sliding generally provided less than 10% of the total deformation throughout all tests. Noting that the measured slip/extension is flexural deformation, flexural deformation provided at least 65% of the deformation. Comparing each pair of beams with varying applied axial stiffness, it was concluded that an increase in axial restraint led to a decrease in the contribution of slip/extension to deformation.

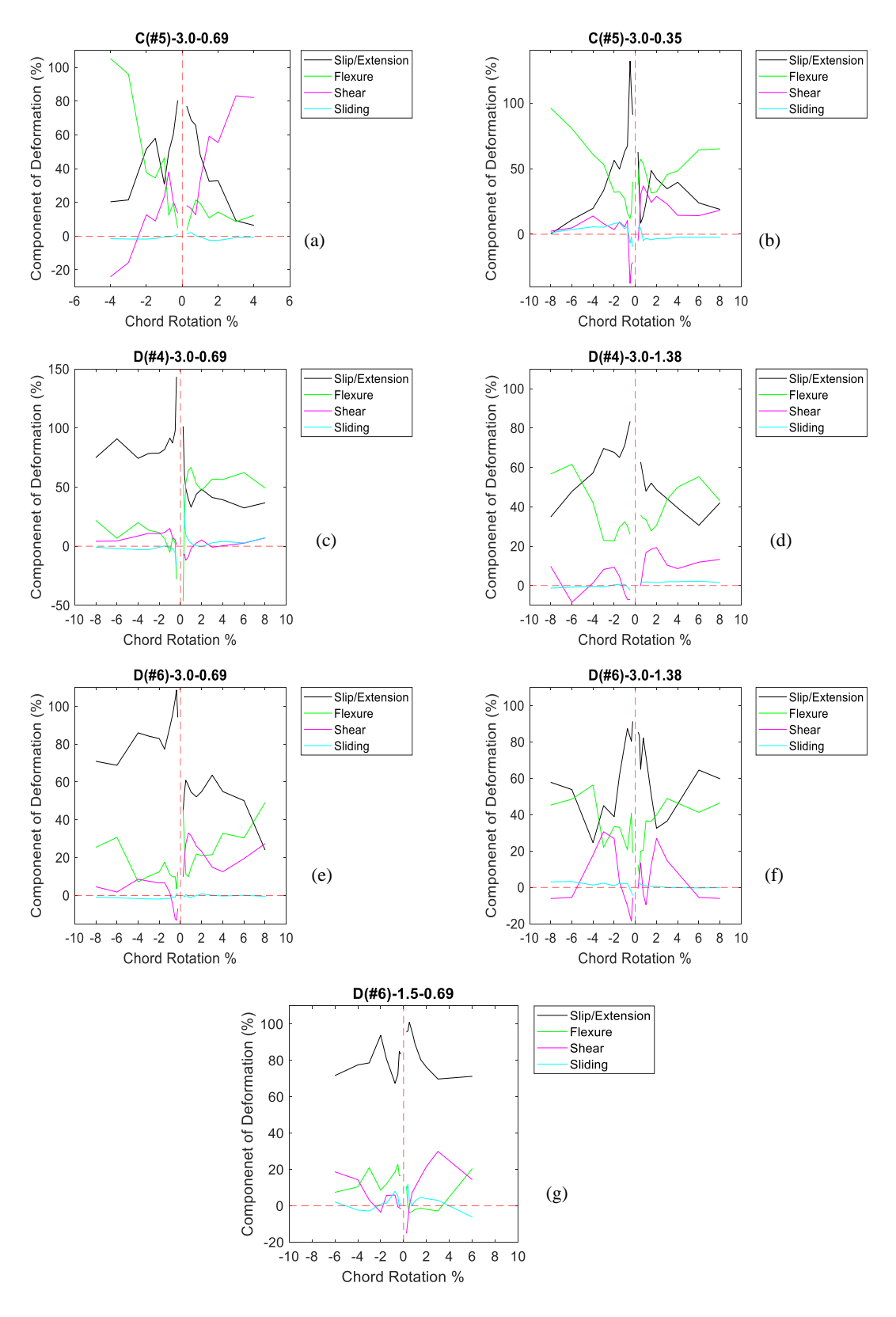


Figure 5.13. Components of Deformation for: a) C(#5)-3.0-0.69, b) C(#5)-3.0-0.35, c) D(#4)-3.0-0.69, d) D(#4)-3.0-1.38, e) D(#6)-3.0-0.69, f) D(#6)-3.0-1.38, and g) D(#6)-1.5-0.69

5.5 Effective Stiffness

The majority of the coupling beam deformation typically occurred due to flexure, as shown in Figure 5.13, such that the effective secant stiffness plots provided in Figure 5.14 were determined assuming all deformation was due to flexure. This is consistent with the approach used by Naish et al (2013) to report coupling beam stiffness for beams without axial restraint. Values of effective secant stiffness in Figure 5.14 were computed at peak displacement of the first cycle for each loading level. (EI)eff was calculated for the fixed-fixed beams as:

$$(EI)_{eff} = \frac{V * L^3}{12 * \delta} \tag{5.4}$$

where V is the peak shear force, L is the length of the beam, and δ is the relative horizontal displacement associated with the shear force. (EI)_{eff} was normalized to E_cI_g in Figure 5.14, where E_c is the modulus of elasticity of concrete and I_g is the moment of inertia of the gross concrete section. E_c was computed as $57\sqrt{f_c'}$ following Section 19.2.2.1 of ACI 318-19, with measured concrete strengths reported in Section 4.3 used for f'_c in this calculation.

Significant variation in effective secant stiffness is evident from Figure 5.14. The diagonally reinforced beams generally had larger effective stiffness values compared to the conventionally reinforced beams, with larger reinforcement ratio corresponding to larger effective secant stiffness for the diagonal beams. The influence of axial restraint on stiffness was more modest than the influence of reinforcement configuration and reinforcement ratio. The shorter beam, D(#6)-1.5-0.69, had significantly lower stiffness than the corresponding longer beam, D(#6)-3.0-0.69. This

was likely due to the lower longitudinal reinforcement ratio for the greater diagonal bar inclination and the greater shear deformation from the shorter span. Initial stiffness, computed at 0.25% chord rotation, varied from $0.21E_cI_g$ for D(#6)-3.0-1.38 to $0.05E_cI_g$ for C(#5)-3.0-0.69. The effective stiffness at 1.0% rotation was between $0.1E_cI_g$ for D(#6)-3.0-1.38 and $0.024E_cI_g$ for D(#6)-1.5-0.69. C(#5)-3.0-0.69 and D(#4)-3.0-1.38 were cracked during test set-up, which may have contributed to the lower initial stiffness values relative to C(#5)-3.0-0.35 and D(#4)-3.0-0.69, respectively.

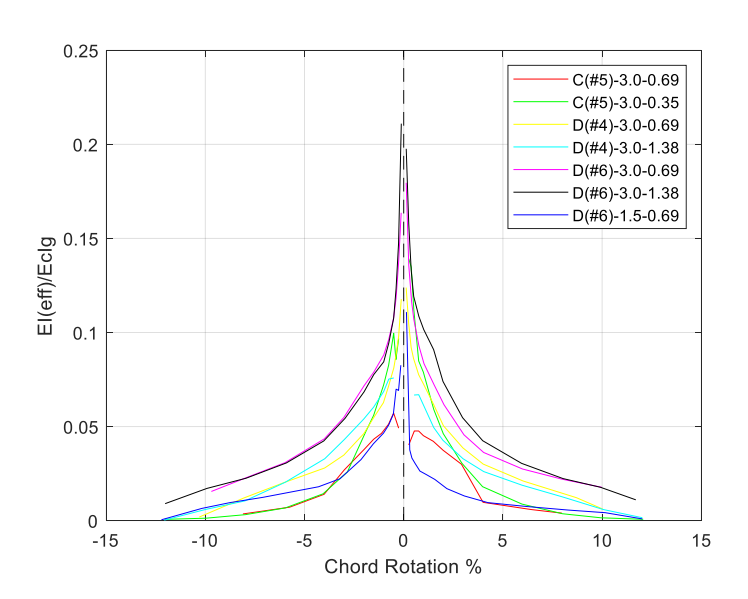


Figure 5.14. Effective Secant Stiffness

5.6 Backbone Models

For each test, a linearized backbone of the test data was formulated by connecting the peak loads at the first cycle of each chord rotation increment, and a multi-linear load-displacement backbone model was fit to the test data backbone, as shown in Figure 5.15. The backbone model was bilinear

up to the maximum shear force, V_{max} , and was formulated following the procedure described in ASCE/SEI 41 Section 7.4.3.2.4. The first line connected the origin to the yield force and intersected the test data backbone at 0.6 of the yield force. The second line connected the yield force to the peak shear force. The yield force was determined by providing an equal area under the test data backbone and model backbone up to the peak shear force. A bilinear model was used for post-peak strength degradation, with one line from V_{max} to $0.8V_{max}$ and the second line from $0.8V_{max}$ to $0.25V_{max}$. Equal area under the test data backbone and model backbone was used to determine the deformation in the model backbone at $0.8V_{max}$ and at $0.25V_{max}$. The backbone models for D(#6)-3.0-0.69 and D(#6)-3.0-1.38 were terminated at $0.8V_{max}$ because the test was stopped prior to reaching $0.25V_{max}$.

The effective stiffness and yield rotation values from the backbone models are provided in Table 5.6. For the conventionally reinforced beams, the rotation at yielding was significantly larger for the beam with larger axial restraint. For the diagonally reinforced beams, minimal difference in the rotation at yielding was associated with variation in axial restraint, while the combination of larger span-to-depth ratio and larger bar size and reinforcement ratio was associated with larger rotation at yielding and larger effective stiffness.

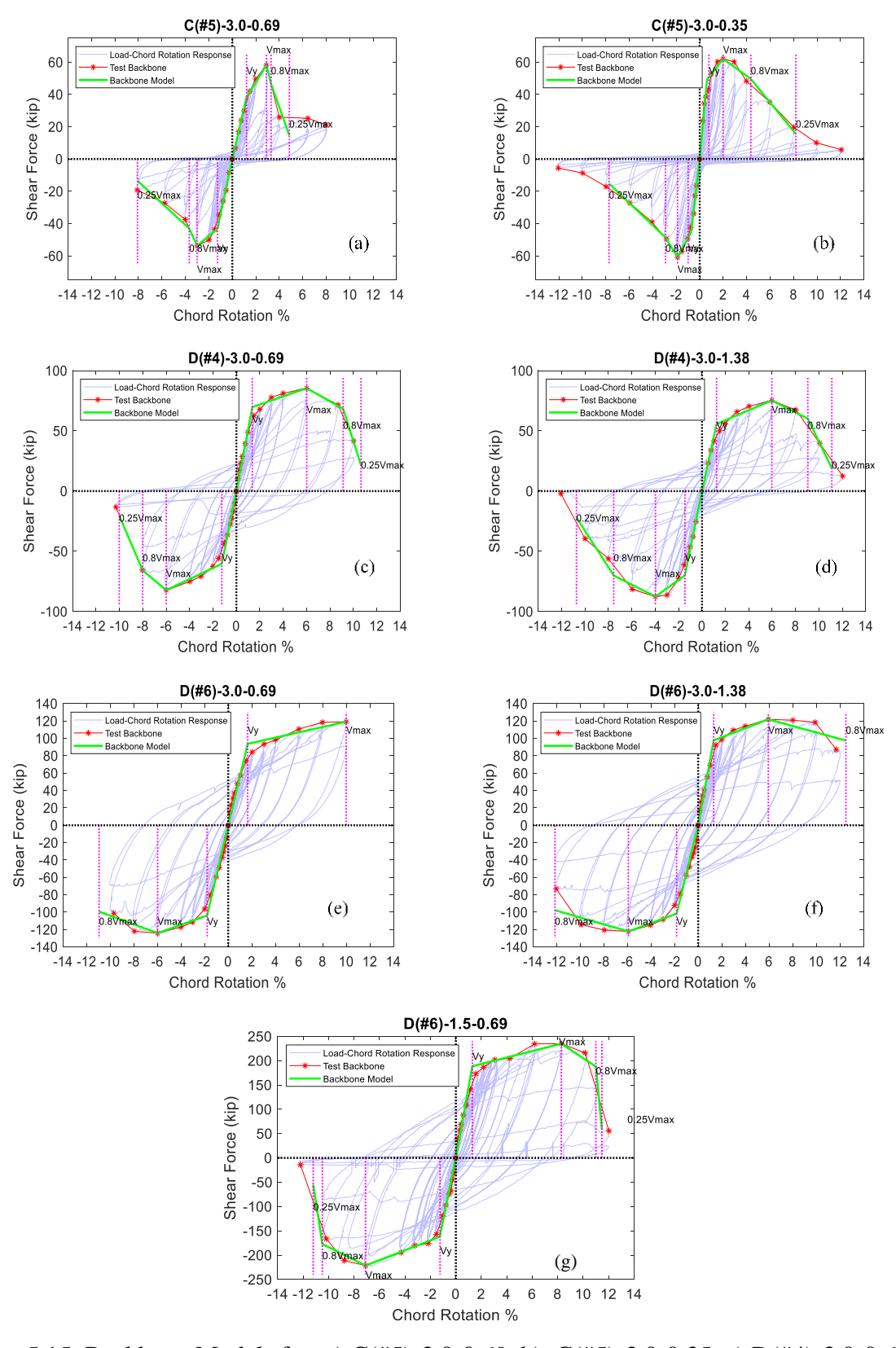


Figure 5.15. Backbone Models for: a) C(#5)-3.0-0.69, b) C(#5)-3.0-0.35, c) D(#4)-3.0-0.69, d) D(#4)-3.0-1.38, e) D(#6)-3.0-0.69, f) D(#6)-3.0-1.38, and g) D(#6)-1.5-0.69

Table 5.6. Effective Stiffness and Yield Rotation from Backbone Model Fit to Test Data

Beam Name	Normalized effective stiffness, (EI) _{eff} / E _C I _g			Rotation at yielding, θ_y %		
	(+)	(-)	Average	(+)	(-)	Average
C(#5)-3.0-0.69	0.048	0.051	0.0495	1.20%	1.20%	1.20%
C(#5)-3.0-0.35	0.118	0.092	0.105	0.60%	0.70%	0.65%
D(#4)-3.0-0.69	0.076	0.072	0.074	1.30%	1.20%	1.25%
D(#4)-3.0-1.38	0.067	0.072	0.0695	1.20%	1.40%	1.30%
D(#6)-3.0-0.69	0.084	0.086	0.085	1.60%	1.70%	1.65%
D(#6)-3.0-1.38	0.111	0.083	0.097	1.30%	1.80%	1.55%
D(#6)-1.5-0.69	0.029	0.051	0.04	1.30%	1.30%	1.30%

For conventionally and diagonally reinforced concrete coupling beams, ACI 318-19 Section A.8.4 and PEER TBI (2017) recommend a flexural rigidity of $0.07 \left(\frac{l}{h}\right) E_c I_g$ and shear rigidity of $0.4E_c A_g$. These values for flexural and shear rigidity were determined for each test beam and converted into an equivalent flexural rigidity using Eq. (3.21). The resulting (EI)_{eff} was $0.198E_cI_g$ and $0.094E_cI_g$ for the beams in this study with span-to-depth ratio of 3.0 and 1.5, respectively. These values are significantly larger than the test values reported in Table 5.6, where the highest value was $0.105E_cI_g$ and $0.04E_cI_g$ for span-to-depth ratio of 3.0 and 1.5, respectively. It is noted in PEER TBI (2017) Section 4.6.3 Commentary that the recommended stiffness values were increased relative to test data in order to account for axial restraint and scale effects in tests. The Naish et al (2013) test data was used in the formulation of these recommended values. Naish et al (2013) reported an effective stiffness of $0.125 E_cI_g$ for the beams without axial restraint tested in that study. The Naish et al (2013) beams had a larger reinforcement ratio relative to the axially restrained beams tested in this study, which may have led to the increase in stiffness. The rotation at yielding for all of the beams except C(#5)-3.0-0.35 was more than 1.0%, while Naish et al (2013)

reported values at roughly 1.0% for the beams in that study. Axial restraint likely contributed to the increase in yield rotation.

5.7 Reinforcement Strain

The reinforcement strain profiles provided in Figure 5.16 were based on strain gauge data measured at the peak displacement of the first cycle of each chord rotation increment. The plots may be used to understand the spread of plasticity in the beam and the concrete block. Larger reinforcement strain was recorded closer to the beam wall-interface. As the chord rotation increased, the length of yielding increased. However, damage to the gauges prevented collection of data much beyond the yield strain.

5.8 Curvature Profiles

The curvature profiles provided in Figure 5.17 were calculated at peaks of initial cycles from the data obtained from the vertical LVDTs within the beam. With the exception of C(#5)-3.0-0.35, curvature values were highest near the ends of the beams, where damage concentrated, noting that slip-extension amplified the curvature values at the beam-wall interface.

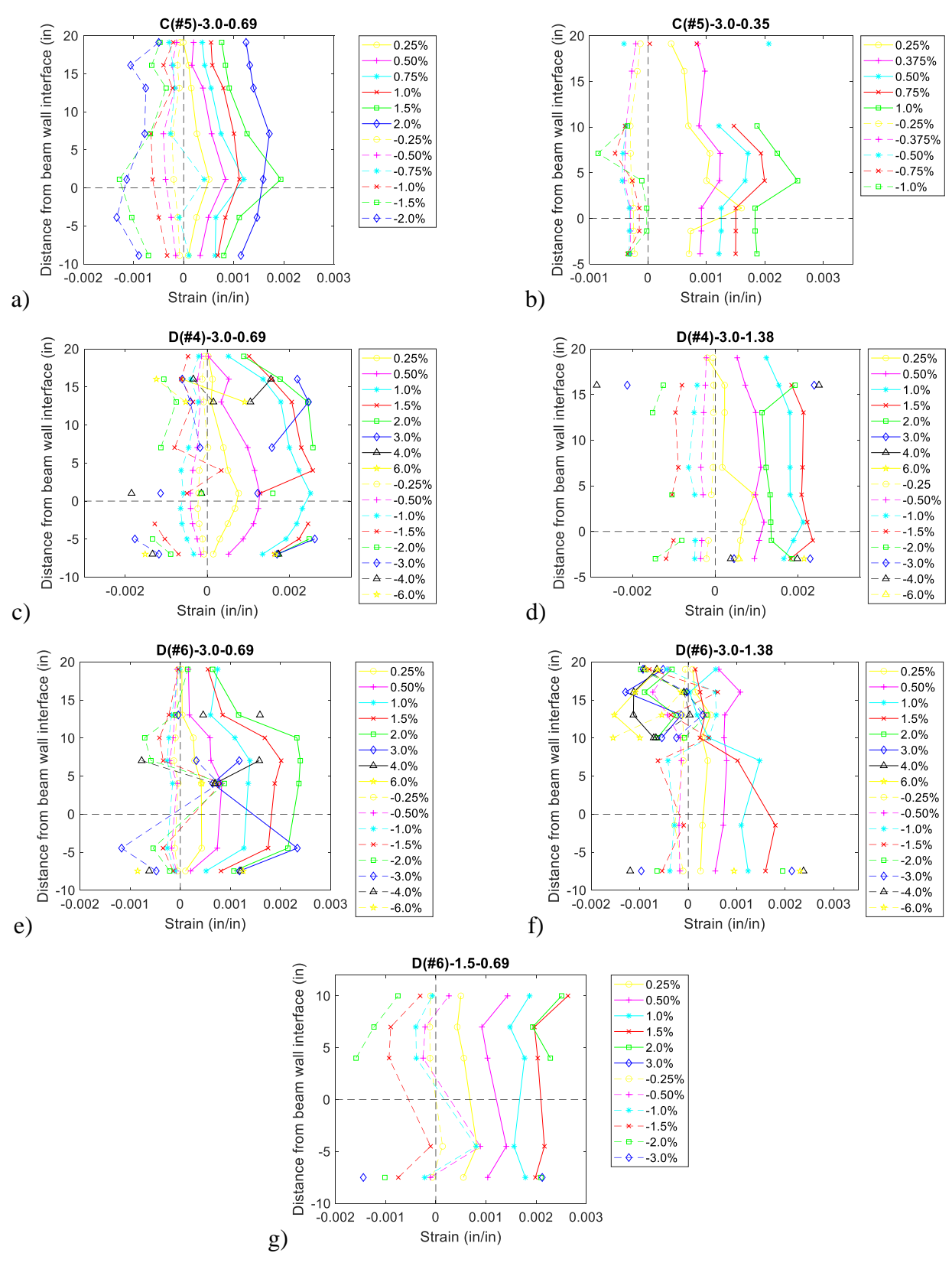


Figure 5.16. Reinforcement Strain Profiles for: a) C(#5)-3.0-0.69, b) C(#5)-3.0-0.69, c) D(#4)-3.0-0.69, d) D(#4)-3.0-1.38, e) D(#6)-3.0-0.69, f) D(#6)-3.0-1.38, and g) D(#6)-1.5-0.69

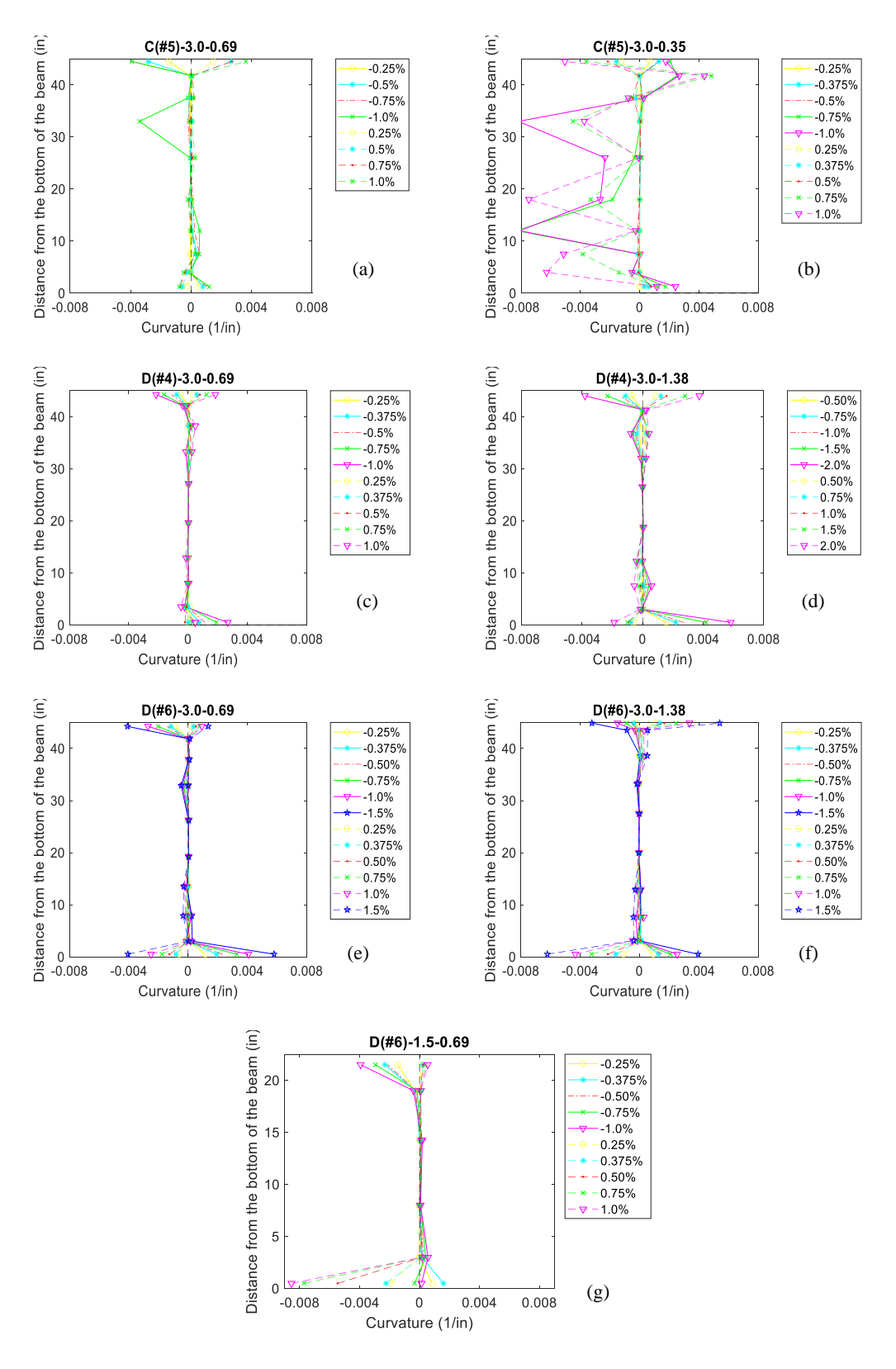


Figure 5.17. Curvature Profiles for: a) C(#5)-3.0-0.69, b) C(#5)-3.0-0.35, c) D(#4)-3.0-0.69, d) D(#4)-3.0-1.38, e) D(#6)-3.0-0.69, f) D(#6)-3.0-1.38, and g) D(#6)-1.5-0.69

6. SUMMARY AND CONCLUSIONS

Current recommendations for the deformation capacity of diagonally reinforced concrete coupling beams prescribe a limit of 3% chord rotation. This limit has existed for several decades despite new test data that has the shown the potential for coupling beams to have higher deformation capacity. A database of diagonally reinforced concrete coupling beams was formulated and used to assess deformation capacity, as well as strength and stiffness. For each test in the database, a piecewise linear backbone model was fit to the test data and used to determine the measured deformation capacity. A plastic hinge model that included bond slip was formulated to estimate deformation capacity based on strain limits. The strain limits were determined using existing models for crushing of confined concrete and buckling of longitudinal reinforcement. In addition to the plastic hinge model, empirical equations to estimate deformation capacity were fit to test data.

The deformation capacity model was not intended to predict axial elongation and capture the resulting influence of axial restraint on coupling beam deformation capacity. To better understand the effect of axial restraint on coupling beam strength and deformation capacity, seven one-half-scale reinforced concrete coupling beams were designed, constructed, and tested to failure under constant stiffness axial restraint and reversed-cyclic lateral loading. The beams were designed to comply with ACI 318-19 provisions. Test variables were reinforcement configuration (longitudinal or diagonal), span-to-depth ratio, primary reinforcement bar size and reinforcement ratio, ratio of transverse reinforcement spacing to primary reinforcement bar diameter (s/d_b), and axial stiffness. The test beams included three pairs of nominally identical beams tested under

varying levels of constant stiffness axial restraint. One of the pairs was conventionally reinforced while the other two pairs were diagonally reinforced.

The following conclusions on diagonally reinforced concrete coupling beams were reached:

- Using the database of past tests, deformation capacity was found to increase with an increase in longitudinal reinforcement ratio, transverse reinforcement ratio, and span-to-depth ratio, and ratio of diagonal bar diameter to section height (d_b/h), and decrease with an increase in the ratio of transverse reinforcement spacing to longitudinal bar diameter (s/d_b). Among the empirical equations considered to estimate deformation capacity, the use of Eq. (3.18) is recommended. Deformation capacity was determined to be primarily dependent on d_b/h and s/d_b in the refined model, and these parameters were included in Eq. (3.18). Consideration was given to the inclusion of transverse reinforcement ratio and span-to-depth ratio in the empirical equation, but this did not reduce the scatter. Consideration was also given to the influence of longitudinal reinforcement ratio, although this parameter was found to have a correlation of r = 0.80 with d_b/h. The refined model was more sensitive to change in d_b/h, resulting in use of this parameter in the empirical model.
- The empirical equation was calibrated to the dataset through regression, while the more refined plastic hinge model was intended to better capture the mechanics of coupling beam behavior, with calibration of a plastic hinge length. Use of a plastic hinge length that attempts to capture the spreading of plasticity from change in moment gradient was investigated by taking L_p as a multiple of diagonal bar length or beam length. A plastic hinge length of 0.5 multiplied by beam depth (0.5h) was found to provide the least amount

of scatter in predicting deformation capacity and generally agreed with the extent of the damage observed in test data. To predict the deformation capacity of diagonally reinforced coupling beams with the refined model, the use of $L_p=0.5 \mathrm{h}$ plus a 2.25% chord rotation increase is recommended. The average ratio of measured to predicted deformation capacity using these recommendations is 0.97 with coefficient of variation of 22%. The empirical equation led to reduced scatter relative to the plastic hinge model, with an average ratio of measured to predicted deformation capacity of 0.97 with a coefficient of variation of 18%.

- Test data suggests that the recommended value of 3% for the modeling parameter *d* in ASCE 41-17 (2017) and ACI 374-16 (2016) underpredicts the deformation capacity of diagonally reinforced coupling beams. Based on statistical results generated from test data, an increase to the parameter *d* is recommended. It is recommended to determine *d* using Eq. (3.18) when using mean values and Eq. (3.19) when using lower-bound values one standard deviation less than the mean.
- Eq. (3.21) is the equation for nominal shear strength provided in ACI 318-19 and considers only the vertical strength of the diagonal bars. This equation was found to be overly conservative, and Eq. (3.22) was considered. This equation includes the shear strength of concrete and transverse reinforcement and was found to provide a better fit to test data. Due to the lack of diagonal compression failure, exclusion of the $10\sqrt{f'c}A_{cw}$ limit in Eq. (3.22) was considered. This led to a better fit to test data, and it is recommended to compute V_n using Eq. (3.22) without the $10\sqrt{f'c}A_{cw}$ limit.
- Strength degradation in the tested diagonally reinforced concrete coupling beams was associated with buckling and fracture of diagonal reinforcement. For beams with aspect ratio of 3.0, damage concentrated at the ends of the beam, while, for the beam with aspect

ratio of 1.5, the damage spread over the length of the beam. The chord rotation at the onset of bar buckling was more sensitive to changes in s/d_b than to changes in the level of axial restraint. The beams with #4 diagonal reinforcement had s/d_b of 5.1 and buckling initiated at 6.0% chord rotation, while the beams with #6 diagonal reinforcement had s/d_b of 3.4-3.7 and buckling initiated at 10.0% chord rotation.

- In the tests, axial elongation was nearly proportional to chord rotation until significant damage was observed, at which stage the elongation decreased as the demand increased. Advanced levels of deformation and damage resulted in axial shortening, resulting in application of axial tension for the constant axial stiffness loading. The diagonally reinforced beams developed high levels of axial compressive stress, with peak values ranging from 0.35-0.51 $A_g f'_c$ for span-to-depth ratios of 3.0 and 0.27 $A_g f'_c$ for the beam with span-to-depth ratio of 1.5. Axial elongation increased with an increase in span-to-depth ratio. The conventionally reinforced beams experienced less axial elongation than the diagonally reinforced beams, as strength degradation in the frame beams was associated with opening of shear cracks rather than damage patterns characteristic of flexural failure.
- Lateral failure was taken as the first cycle peak at which a 20% or greater loss of peak strength occurred and was sustained for the remainder of the test. For the tested beams, deformation capacity was more sensitive to changes in s/d_b than the level of axial restraint, as strength degradation was associated with bar buckling. The beams with #4 and #6 reinforcement had a deformation capacity of at least 6% and 10%, respectively. The deformation capacity was at least 15% larger than that predicted using the empirical model (Eq. (3.18)), suggesting that axial restraint did not lead to reduction in deformation capacity. The deformation capacity of the diagonally reinforced beams was significantly

larger than that of the two conventionally reinforced beams, which reached peak strength at 3% chord rotation and experienced rapid post-peak strength degradation due to the opening of diagonal cracks. The deformation capacity of these frame beams was less than that experienced by flexure-yielding frame beams from other studies.

- For the beams tested in this study, constant axial compressive stiffness ranging from $0.69A_gf'_c$ to $1.38A_gf'_c$ per inch led to peak compressive stresses of 0.27- $0.51A_gf'_c$ and a resulting increase in beam strength estimated at 9%-64%, with larger values for lower longitudinal reinforcement ratio. As unrestrained beams were not tested in this study, this estimate was based on the increase in calculated M_n for the peak measured axial force. Peak measured shear demand was as large as 120% above $V@M_n$ calculated for M_n with no axial restraint and 53% above $V@M_n$ calculated for M_n with the peak measured axial force. ACI 318-19 does not explicitly recommend capacity design for coupled walls. It is recommended that an upper bound for coupling beam strength be used in the determination of wall demands. If the probable moment strength of a coupling beam was computed in the same manner as a special moment frame beam (i.e., using $1.25f_y$), additional strength may be created by axial restraint. Although further research is needed to better characterize the level of overstrength from axial restraint, results from this study provide experimentally derived values for the levels of axial demand considered in the study. Additional research is also needed to characterize typical levels of axial restraint for coupling beams.
- Throughout the tests, at least 65% of the deformation in the diagonally reinforced beams
 was due to flexure, which included the contribution from interface slip/extension. As the
 level of axial restraint increased, the percent contribution of slip/extension to lateral
 displacement decreased.

• The tested diagonally reinforced beams generally had larger effective stiffness values compared to the conventionally reinforced beams, with larger reinforcement ratio corresponding to larger effective secant stiffness for the diagonal beams. Based on the backbone models formulated for the test beams, the yield rotation for the conventionally reinforced beams increased with an increase in axial compression. For the diagonally reinforced beams, the beams with larger bar size (#6) had greater yield rotation and effective stiffness, while the effect of axial restraint was minimal.

REFERENCES

ACI 318-19. (2011). Building Code Requirements for Structural Concrete (ACI318-11) and Commentary (ACI318R-11). American Concrete Institute, Farmington Hills, Michigan.

ACI 374.2R-13 (2013). "Guide for Testing Reinforced Concrete Structural Element under Slowly Applied Simulated Seismic Loads". American Concrete Institute, Farmington Hills, Michigan.

Alsiwat, J.M., and Saatcioglu, M. (1992). "Reinforcement Anchorage Slip under Monotonic Loading," ASCE Journal of Structural Engineering, 8(9): 2421-2438.

ASCE-SEI 41-17. (2017). "Seismic Rehabilitation of Existing Buildings," American Society of Civil Engineers, Reston, Virginia.

Barbachyn, S.M, Kurama, Y.C., and Novak, L.C. (2012). "Analytical Evaluation of Diagonally Reinforced Concrete Coupling Beams under Lateral Loads." ACI Structural Journal, 109(4): 497-507.

Barney, G.B., Shiu, K.N., Rabbat, B.G., Fiorato, A.E., Russell, H.G., and Corley, W.G. (1980). "Behavior of Coupling Beams Under Load Reversals." Portland Cement Association.

Binney, J.R. (1972). "Diagonally Reinforced Coupling Beams," PhD Thesis, University of Canterbury, Christchurch, New Zealand.

FEMA 273. (1997). "NEHRP Guidelines for the Seismic Rehabilitation of Buildings," Federal Emergency Management Agency, Washington, DC.

Fortney, P.J., Rasaati, G.A., and Sharhooz, B.M. (2008). "Investigation on Effect of Transverse Reinforcement on Performance of Diagonally Reinforced Coupling Beams," ACI Structural Journal, 105(6): 781-788.

Galano, L., and Vignoli, A. (2000). "Seismic Behavior of Short Coupling Beams with Different Reinforcement Layouts," ACI Structural Journal, 97(6): 876-885.

Ghannoum, W.M., and Matamoros, A.B. (2014). "Nonlinear Modeling Parameters and Acceptance Criteria for Concrete Columns." ACI Special Publication 297.

Han, S.W., Lee, C.S., Shin, M., Lee, K., (2015). "Cyclic Performance of Precast Coupling Beams with Bundled Diagonal Reinforcement," Engineering Structures, 93(2015): 142-151.

Jang, S.J., Jeong, G.Y., Yun, H.D., (2018). "Use of Steel Fibers as Transverse Reinforcement in Diagonally Reinforced Coupling Beams with Normal and High Strength Concrete," Construction and Building Materials, 187(2018): 1020-1030.

Kwan, A.K.H., Zhao, Z.Z. (2002). "Testing of Coupling Beams with Equal Rotations Maintained and Local Joint Deformation Allowed," University of Hong Kong.

Lee J-Y., and Watanabe F. (2003). Predicting the longitudinal axial strain in the plastic hinge regions of reinforced concrete beams subjected to reversed cyclic loading. Engineering Structures, 25(7):927–939.

Lehman, D., Turgeon, J., Birely, A., Hart, C., Marley, K., Kuchma, D., and Lowes, L. (2013). "Seismic Behavior of a Modern Concrete Coupled Wall." ASCE Journal of Structural Engineering, 139(8), 1371-1381.

Lim, E., Hwang, S.J., Cheng, C.H., and Lin, P.Y. (2016). "Cyclic Tests of Reinforced Concrete Coupling Beam with Intermediate Span-Depth Ratio," ACI Structural Journal, 113(3): 515-524.

Mander, J. B., Priestly, J.N., Park, R. (1988). "Theoretical Stress-Strain Model For Confined Concrete." ASCE Journal of Structural Engineering, 114(8): 1827-1849.

Massone, L.M. and Wallace, J.W. (2004). "Load-Deformation Responses of Slender Reinforced Concrete Walls." ACI Structural Journal, 101(1), 103-113.

Mohr, D.S. (2007). "Nonlinear Analysis and Performance Based Design Methods for Reinforced Concrete Coupled Shear Walls," M.S. Thesis, University of Washington.

Motter, C.J., Abdullah, S.A., Wallace, J.W., "Reinforced Concrete Structural Walls without Special Boundary Elements", ACI Structural Journal, 115(3): 723-733.

Naish, D., Fry, A., Klemencic, R., and Wallace, J. (2013a). "Reinforced Concrete Coupling Beams—Part I: Testing." ACI Structural Journal, 110(06): 1057-1066.

Naish, D., Fry, A., Klemencic, R., and Wallace, J. (2013b). "Reinforced Concrete Coupling Beams—Part II: Modeling." ACI Structural Journal, 110(06): 1067-1075.

Paulay, T., and Binney J.R. (1974). "Diagonally Reinforced Coupling Beams of Shear Walls," ACI Special Publication 42-46, Farmington Hills, MI.

PEER TBI. (2017). "Guidelines for Performance-Based Seismic Design of Tall Buildings," Pacific Earthquake Engineering Research Center, Berkeley, California.

Poudel, A., Lequesne, R.D., and Lepage, A. (2018). "Diagonally Reinforced Concrete Coupling Beams: Effects of Axial Restraint." SL Report 18-3, the University of Kansas Center for Research, Inc., Lawrence, KS.

Priestley, M.J.N., Seible, F., and Calvi, G.M. (1996) "Seismic Design and Retrofit of Bridges", John Wiley & Sons, NY.

Rodriguez, E.R., Botero, J.C., and Villa, J. (1999) "Cyclic Stress-Strain Behavior of Reinforcing Steel Including Effect of Buckling", ASCE Journal of Structural Engineering, 125(6): 605-612.

Santhakumar, A.R. (1974). "The Ductility of Coupled Shear Walls," University of Canterbury, Christchurch, New Zealand.

Shin, M., Gwon, S.W., Lee, K., Han, S.W., and Jo, Y.W. (2014) "Effectiveness of High Performance fiber-reinforced Cement Composites in Slender Coupling Beams", Construction and Building Materials, 68(2014): 476-490.

Tassios, T.P., Moretti, M., and Bezas, A. (1996). "Behavior and Ductility of Reinforced Concrete Coupling Beams of Shear Walls," ACI Structural Journal, 93(6): 711-719.

Tegos, I.A., and Penelis, G.Gr. (1988). "Seismic Resistance of Short Columns and Coupling Beams Reinforced with Inclined Bars," ACI Structural Journal, 85(1): 82-88.

Weber-Kamin, A.S., Ameen, S., Lequesne, R.D., Lepage, A., (2019). "Reinforced Concrete Coupling Beams with High-Strength Steel Bars," PhD Dissertation. The University of Kansas.

Xiao, Y., Esmauily-Ghasemabadi, A., and Wu, H. (1999). "High-Strength Concrete Short Beams Subjected to Cyclic Shear," ACI Structural Journal, 96(3): 392-400.